The Dissertation Committee for Ali Ghahremaninezhad Mianji Certifies that this is the approved version of the following dissertation:

On the Role of Microstructure in Ductile Failure

Committee:

Krishnaswamy Ravi-Chandar, Supervisor

Mark E. Mear

Kenneth M. Liechti

Rui Huang

Amine Benzerga

On the Role of Microstructure in Ductile Failure

by

Ali Ghahremaninezhad Mianji, B.S.; M.S.

Dissertation

Presented to the Faculty of the Graduate School of

The University of Texas at Austin

in Partial Fulfillment

of the Requirements

for the Degree of

Doctor of Philosophy

The University of Texas at Austin

August 2011

Dedication

To my parents for their endless support, love and encouragement

To my sisters, Azadeh and Atoosa

To my brother, Amir

Acknowledgements

I would like to express my appreciation to my advisor, Professor Krishnaswamy Ravi-Chandar, for his excellent guidance and support throughout my Ph.D. I would also like to thank my committee members for their helpful comments. I would like to thank my professors at EM with whom I took courses. Thanks go to the members of the machine shop, Travis Crooks, David Gray and Ricardo Palacios, for their help in specimen preparation. I enjoyed the friendship of my colleagues: Aaron, Federico, Fassett, Haitao and Johnathan, to name a few during my stay at UT.

On the Role of Microstructure in Ductile Failure

Ali Ghahremaninezhad Mianji, Ph.D.

The University of Texas at Austin, 2011

Supervisor: Krishnaswamy Ravi-Chandar

Failure in structural materials occurs initially by localization of deformation, and subsequently through a process of nucleation, growth and coalescence of voids. Predicting material failure requires a careful investigation of the different stages of damage evolution at the multiple scales. The main objective of this thesis is to explore the evolution of damage and to correlate this with the deformation of the material at the continuum and microstructural levels. This is accomplished through macroscopic measurements of strain evolution using digital image correlation and microscale measurements of strain and damage using optical and scanning electron microscopy.

Three materials with different microstructure were examined. In oxygen-free, high-conductivity copper, a high-purity material without appreciable second phase particles, strain levels in the order of three were observed in the material without any trace of damage. Failure was observed to be triggered by plastic instability in the form of shear bands and the emergence of a prismatic cavity that grows in a self-similar fashion by an alternating slip mechanism. In Al 6061-T6, a material with a dispersion of second phase particles at a volume fraction of about 0.01, nucleation of damage does not appear until plastic strain levels of 0.5 to 1.0. Once damage in the form of particle fracture or decohesion at the interface initiates, subsequent failure follows by the void nucleation, growth and coalescence; but, dominated by the fluctuations in the distribution of second

phase particles, final separation occurs in a highly localized layer of material on the order of the grain size, corresponding to a small increase in the overall strain. In nodular cast iron, a material with an initial porosity of about 0.10, growth of voids was observed initially, but this was terminated by a transition of the deformation into a localized region.

Phenomenological models based on strain-to-failure and micromechanical models based on a mechanistic description of the microscale deformation are evaluated in light of the above examination of failure in these three classes of materials.

Table of Contents

List of Tables

List of Figures

List of Supplemental Files

File 1. A high resolution image of Figure 2.4.

File 2. A high resolution image of Figure 2.6a.

File 3. A high resolution image of Figure 2.7.

File 4. A high resolution image of Figure 2.15a.

File 5. A high resolution image of Figure 2.15b.

File 6. A high resolution image of Figure 2.15c.

Chapter 1: Introduction and Literature Review

1.1. INTRODUCTION

Failure of many ductile materials used in structural applications is typically considered to occur by the progressive nucleation, growth and coalescence of damage. While such damage must have atomistic origins, in polycrystalline materials, such atomic scale processes are often mediated by the defect structure in these materials at a much larger length scale: typically, microstructural features that are of the size of grains and/or second phase particles or inclusions ($\sim 10^{-5}$ m) have a great influence on the evolution of damage. Therefore, microscopic models of damage in materials consider continuum level modeling of damage. In such continuum models, the introduction of the idea of a Representative Volume Element (RVE) in which all properties can be represented by homogenized internal variables representing the damage evolution is essential to model development. Homogenization requires that the size of the RVE be selected so as to contain a statistically uniform representation of the damage process within the RVE. The size of the RVE can vary from about 10^{-3} mm^3 for metals and ceramics to about 10^6 mm^3 for concrete. The damage discontinuities in the RVE are considered to be "small" with respect to the size of the RVE, but large compared to the atomic spacing and even grain size (Lemaitre and Desmorat 2006). The damage is called ductile damage if it is the nucleation, growth and coalescence of microvoids in the microstructure (Figure 1.1a); in this case, the damage is measured as the fractional volume of voids in the RVE. On the other hand, the brittle damage can be classified as perfectly brittle or quasi-brittle; in perfectly brittle damage, the specimen with pre-existing microcracks fails without damage accumulation when the stress reaches some critical threshold (Figure 1.1b). In quasi-brittle damage, the deformation is characterized by a nonlinear segment of force-

elongation curve that precedes the final failure of the specimen (Figure 1.1c). During quasi-brittle damage the material does not flow gradually but it continuously degrades as interatomic bonds break progressively during the loading (Krajcinovic 1996). Some materials behave in a combined ductile–brittle manner where there is permanent deformation in addition to loss of stiffness (Figure 1.1d). In this dissertation attention is focused on the ductile failure.

Interest in ductile fracture stems from the need to develop structural reliability assessment procedures that take into account progressive damage in materials. Research in the field of ductile fracture has also been motivated by applications to metal forming, powder metallurgy, composite materials and a class of polymers (Benzerga et al. 2004). Figure 1.2 shows a schematic diagram of the different stages of ductile failure by void nucleation, growth and coalescence. First, micovoids nucleate at second phase particles at some stage during the loading history (Tipper 1949; Puttick 1959). These second phase particles are a product of the manufacturing process during which nucleating agents and alloying elements are added to metals; the nucleating agents promote nucleation of grains and control grain size distribution while the alloying elements provide specific microstructural features such as precipitates, and multi-phase structure (see Figure 1.3a), that can be used to develop specific material characteristics such as high yield strength, wear or corrosion resistance. However, in many cases, these second phase particles act as nucleation sites for damage during large inelastic deformation; this nucleation can be either through particle fracture or by decohesion at the particle-matrix interface, depending on the flow properties of the matrix, the particle size and morphology, the stiffness mismatch between the matrix and the particle, and the local stress state. These two modes of nucleation are illustrated in the micrographs of two model materials in Figure 1.4. Matrix-particle interface decohesion in a material made of soft matrix and

hard particles is illustrated in Figure 1.4a; particle fracture in a material made of higher strength matrix and hard particles is shown in Figure 1.4b. Many investigators have performed experiments and created model simulations of the nucleation problem in order to provide a quantitative measure of the stress at nucleation. Metal compacts manufactured by powder metallurgy techniques may already have an initial distribution of microvoids in the microstructure, formed as a result of incomplete densification (Figure 1.3b). Also in materials such as nodular cast iron, this stage of nucleation may not be observed. Second, voids that are either present in the material initially or nucleated during the first stage, grow in size with continued macroscopic deformation; note that this growth must occur at the submicroscale by slip in the lattice of polycrystalline metals. However, growth of the voids is typically evaluated by considering a continuum plasticity model of the deformation as in the analysis of McClintock (1968), and Rice and Tracey (1969). Macroscopic response of the material corresponding to such growth of voids is obtained using homogenization theory (for example Gurson 1977), and exhibits softening of the material response with continued deformation. The third and final stage of ductile damage is the coalescence of voids by plastic strain localization in the ligaments between the voids in the form of internal necking or shear bands. An example of void coalescence is illustrated in Figure 1.5; at the onset of coalescence the deformation is localized into a thin layer of highly strained material. Two different modes of coalescence are observed: internal necking in the intervoid ligament as shown in Figure 1.5a occurs when the stress state in the ligament is predominantly tensile, and shear localization occurs as shown in Figure 1.5b when the stress state in the ligament between two voids is shear dominant. In both cases, this localized phenomenon results in a sharp drop in the stress-strain response of the ductile materials as illustrated in Figure 1.2. The specific details of the onset of nucleation, the nature of the growth and

coalescence are, of course, material dependent. This class of micromechanical models that incorporate void nucleation, growth and coalescence are typically called Rousselier or Gurson-Tvergaard-Needleman (GTN) models and the general framework of these models is now rather well-established. Tvergaard (1990) and Benzerga and Leblond (2010) provide a comprehensive review of this approach to modeling of ductile failure.

Calibration and validation of these models have been attempted by numerous investigators (see for example, Brocks et al. 1996; Dong et al. 1996; Decamp et al. 1997; Pardoen et al. 1998; Steglich and Brocks 1998; Benseddiq and Imad 2008). However, this process is inherently non-unique, since many different combinations of parameters appear to capture the softening part of the material/structural response (Bernauer and Brock 2002). In this dissertation, attention is focused on quantitative assessment of the microscopic deformation and failure mechanisms in order to evaluate the applicability of micromechanical models of ductile failure.

1.2. LITERATURE REVIEW

One of the earliest experimental investigations in ductile fracture was by Ludwik (1926) who observed the formation of central cracks in aluminum tensile specimens with a final cup and cone failure mode. Tipper (1949) studied the fracture mechanisms in mild steel and alpha iron, and concluded that there were two fracture mechanisms: one occurred along specific crystallographic planes with little plastic deformation in the crystal (brittle cleavage fracture), and the other occurred by drawing the crystals away from the inclusions into fibrous form (ductile fracture by void growth). Separation of the matrix from inclusions was observed at a distance ahead of the crack tip. Orowan (1948) showed yet another mechanism of failure – based on observations by Tipper of the

formation of a polyhedral transverse channel in the neck of an aluminum single crystal specimen, he provided a mechanism of alternating slip for the formation of a cavity at the center of the necked specimen. This is described in more detail in Chapter 2.

Puttick (1959) examined fracture phenomena in high conductivity, 99.9% pure copper, α-iron and pure polycrystalline aluminum (>99.9%) by examining specimens failed under uniaxial tension. He found that in high conductivity copper (grain size about 50 μm), voids were formed at nonmetallic inclusions through drawing away of the metal or fracture of inclusions. These cavities then grew and finally coalesced to form the final rupture of the specimen; the resulting fracture surface in this material was of the typical cup-and-cone type. Fracture initiation in α-iron was identified to be triggered by opening of cavities at inclusions as in copper, but ahead of these a system of fine non-crystallographic cracks linking the inclusions was found. Puttick observed that even though inclusion cavities formed and grew as in copper, the fracture mechanism was different: cracks were nucleated at cavities of a critical size; then they propagated through the material linking up other inclusion sites. It was proposed that cracks were initiated at points of high tensile stress and because they did not require additional plastic strain they propagated much more rapidly than void growth. It was particularly observed that there were not many large voids away from the fracture surface; this was explained by the fact that only a couple critically grown voids were sufficient to trigger the crack. In the case of high purity polycrystalline aluminum, Puttick found that fracture occurred at the neck of a tensile specimen by slipping-off along a plane of shear oriented approximately at 45° to the axis of stress.

Rogers (1960) studied the tensile ductile fracture in oxygen free, high conductivity (OFHC) copper with heat treatment in three different environments: hydrogen, dry nitrogen and vacuum; the average grain size was about 1 mm. It was

observed that ductile fracture is initiated by the formation of cavities in the center of tensile specimens; the cavities were intergranular in the case of hydrogen treatment, and intragranular in the case of heat treatment in dry nitrogen and vacuum. These voids grew with plastic strain until they coalesced to form a central crack. Crack grew by localization of shear strain at a plane approximately 30º to 40º from the axis of tensile stress. Due to high level of shear strain in this localized band, a large number of small voids were nucleated and subsequently failed under applied tension (void sheet); Rogers also observed that if the crack propagated to the specimen surface by this mechanism the result is a cup-cone fracture surface which is commonly seen in iron, brass and duralium. On the other hand for material such as aluminum, gold, silver and copper, Rogers believed that the final separation takes place by either "ductile cleavage" (a term used by Rogers) or alternating slip as suggested by Orowan (1948).

1.2.1. Void Nucleation

Argon and Im (1975) measured quantitatively the conditions for decohesion of the matrix-particle interface in three different ductile materials: spheroidized 1045 steel, Cu-0.6%Cr alloy and maraging steel. They evaluated the local interfacial strength for separation of the second phase particles during the plastic deformation by the method described in their two previous papers (Argon et al. 1975a,b). The spheroidized 1045 steel had 0.125 volume fraction of equiaxed Fe_3C of mean particle diameter 0.44 μm. The ferrite grain size was about 5-10 μm. They observed that the mean diameter of separated particles was larger than that of the whole population. It was shown that larger than average size particles separated first and that other particles of smaller size separated with increasing plastic strain in an inverse relation to the particle size. This was explained by

an increase of interfacial stress as a result of interaction of particles at the regions of high local volume fraction. The Cu-0.6%Cr alloy studied in their work was aged and measured to have second phase Cu-Cr particles of 0.89 μm mean diameter and 0.0059 volume fraction. These particles were not always equiaxed and had a mean aspect ratio of 4; the grain size was in the range of 20-30 μm. The maraging steel studied had two types of second phase particles: TiC inclusions of volume fraction 0.011 with mean diameter of 5.3 μm and smaller size Ni_3Mo particles of about 0.5 μm diameter or smaller. Argon and Im (1975) focused their attention only on the large TiC particles. In contrast to the spheroidized 1045 steel, they found no preferential size dependent decohesion of the matrix-particle interface in Cu-0.6% Cr and maraging steel; this was attributed to the dilute concentration of particles where the particles were essentially non-interacting.

There have been numerous attempts to model the nucleation stage of ductile fracture. In early works on void formation at inclusions, for example by Argon et al. (1975a,b), the interfacial stress concentration of a work hardening solid with rigid equiaxed inclusions was analyzed within the continuum theory of plasticity and comparisons with experimental results by Argon and Im (1975) were made. Beremin (1981) investigated the cavity formation at inclusions in circumferentially notched tensile specimens made of A508 steel. Beremin reported that nucleation at elongated MnS occurs through particle fracture in longitudinal direction while the nucleation mode in transverse direction is interfacial decohesion. Beremin suggested a critical local stress criterion for nucleation of damage for both particle and interfacial breakage based on an extension of Eshelby's (1957) theory for inclusions in plastically deforming matrix originally proposed by Berveiller and Zaoui (1979). Lee and Mear (1999) studied the effects of particle morphology on the stress concentration at the particle-matrix interface and within the particle for different matrix properties and stress triaxiality levels. Babout

et al. (2004) investigated the dependence of particle fracture and particle-matrix debonding mechanisms on ductile matrix behavior, and compared their proposed model with results of model composite materials. They remarked that even though the larger particles seem to fracture at lower stress, the issue of size dependence of damage nucleation is an open question and needs more investigations. Chu and Needleman (1980) proposed stress-based and strain-based criterion for nucleation of voids in ductile materials. In addition, in order to account for the statistical variability in the second phase particles, they suggested a normal distribution for the nucleation strain. Although there appears to be a dearth of experimental characterization of the statistics of nucleation of cavities, this nucleation model has been used widely due to the ease of its implementation. The relation introduced by Chu and Needleman (1980) is written as follows

$$\dot{f}_n = A(\varepsilon_{eq}^p)\dot{\varepsilon}_{eq}^p + B(\dot{\Sigma}_m) \tag{1.1}$$

where

$$A(\varepsilon_{eq}^p) = \frac{f_N}{s_N\sqrt{2\pi}}\exp\left[-\frac{1}{2}\left(\frac{\varepsilon_{eq}^p - E_N}{s_N}\right)^2\right] \tag{1.2}$$

$\dot{f}_n$ is the rate of nucleation of voids, f_N is the volume fraction of the nucleating particles, E_N and s_N are the mean and standard deviation, respectively, of a normal distribution assumed for strain controlled nucleation process, $\dot{\Sigma}_m$ is the rate of macroscopic mean stress and B represents the dependence of stress controlled nucleation process; stress dependent nucleation is typically not considered in the literature. However, this model does not account for void size effects on nucleation and furthermore, given the long tail

of the normal distribution, nucleation of voids may occur at very low strain values and influence the material model even when the material exhibits deformation without damage.

1.2.2. Void Growth

Spitzig et al. (1988) studied the mechanical response of sintered iron specimens with different initial densifications subjected to tensile and compressive loadings. They made quantitative measurements of evolution of microstructural features such as void area fraction, void size and void shape during the deformation history. Using a Dirichlet tessellation technique they also pointed out that there existed a region of higher than average local pore volume fraction within the material where the localization occurred and resulted in the fracture of the material. In another study, Spitzig (1990) examined the effect of hydrostatic pressure on the deformation, evolution of damage and fracture in sintered iron. It was found that the ductility of specimens made of sintered iron increased linearly with hydrostatic pressure and that the influence of pressure increased with initial porosity. In another work on porous sintered steels, Chawla and Deng (2005) studied the influence of microstructure on the mechanical properties of specimens made of Fe-0.85Mo-Ni with three different initial porosities and microstructural characteristics. They found that all mechanical properties – tensile strength, Young's modulus, strain to fracture and fatigue strength – decreased with increasing porosity. They concluded that while the strength of the material depends on the porosity, the ductility is highly sensitive to the size distribution, shape and the degree of clustering in the microstructure.

Jablokov et al. (2001) monitored the evolution of damage in terms of void volume fraction in HY-100 steel over a range of temperatures (-85°C to 25°C), strain rates (10^{-3}/s

to 10^3) and stress triaxialities (0.8 to 1.3) under tensile loading of circumferentially notched specimens. The microstructure of the material contained 0.00015 area fraction of large MnS inclusions of length 50 μm elongated in rolling direction and surrounded by smaller equiaxed sulfides; the length to width ratio of these inclusions was about 20:1 and are distributed in bands of width 20 μm and spaced 50 to 60 μm apart. Their results indicated that damage initiated at elongated MnS particles at the early stages of deformation with a slow growth which is essentially insensitive to the temperature and strain rate, but highly dependent on the stress state and plastic strain. It was observed that the stable growth stage was terminated by a rapid void growth resulting from localization in the ligament between elongated primary voids. Prior to the onset of rapid void growth, the void volume fraction increased from a value corresponding to the initial volume fraction of second phase particles to ~0.004 for a triaxiality of ~1.1 as the macroscopic equivalent strain increased from zero to 0.10; coalescence occurred rather abruptly at this stage.

In another experimental work very similar to that in Jablokov et al. (2001), but on a different material (HSLA-100 steel), Chae and Koss (2004) concluded that while the two types of steel (HY-100 and HSLA-100) had very similar yield strength, hardening behavior and inclusion content, the failure mechanism was different, with a ductility of the HSLA-100 steel being more than double that of HY-100 steel. This large difference in ductility was attributed to the different microstructural features; while in HSLA-100 damage nucleates at nearly spherical sulfides that result in growth and coalescence of equiaxed voids; damage in HY-100 initiates at large elongated sulfides; and the growth is terminated by the early formation of flow localization in the ligament between the elongated voids.

The growth of existing or nucleated voids with plastic strain in ductile porous solids has been investigated extensively by many researchers. McClintock (1968) analyzed the expansion of a long circular cylindrical hole in an infinite non-hardening matrix stretched in the axial direction ($\sigma_{z\infty}$) and subjected to remote lateral stresses ($\sigma_{r\infty}$) and found the following relation for the growth of the cylindrical hole

$$d\log\frac{b}{b_0}=\sqrt{3}\sinh\left(\frac{\sqrt{3}\sigma_{r\infty}}{\sigma_{r\infty}-\sigma_{z\infty}}\right)d\varepsilon_{r\infty}+d\varepsilon_{r\infty} \tag{1.3}$$

where b_0 and b are the initial and current hole radii. Rice and Tracy (1969) calculated the growth of a spherical cavity in a rigid-perfectly plastic matrix under remote strain rate field as follows

$$\frac{dR_0}{R_0}=C\exp\left(\frac{\sqrt{3}\sigma^{\infty}}{2\tau^{0}}\right)d\varepsilon_{eq}^{p} \tag{1.4}$$

where R_0 is the radius of the void, σ^{∞} is the remote mean stress, τ^{0} is the yield stress in shear, ε_{eq}^{p} is the equivalent plastic strain and C is a parameter.

The exponential dependence of void growth on the stress triaxiality – defined as the ratio of mean stress to equivalent stress – can be realized in equations (1.3) and (1.4). This is in accord with a body of experimental results that indicate a similar dependence of the ductility on stress triaxiality. Over the past four decades, many models have been introduced to take into account the effect of damage on deformation (see for example, Gurson 1977; Rousselier 1987). The Gurson model is one of the most widely used micromechanics-based constitutive formulations for ductile fracture that was derived following the analysis of Rice and Tracy (1969). In the Gurson model, hollow spheres with constant inner to outer radii ratio are assembled to form a model for the damaging

solid (Figure 1.6). The matrix material is assumed to be incompressible, rigid-perfectly plastic, and follow isotropic J_2-flow theory of plasticity. This model which accounts for dilatation was derived by adopting a kinematically admissible displacement field compatible with prescribed linear displacement on the outer boundary. The admissible displacement field is used to calculate the effective stresses via an upper bound approach. The yield surface is expressed as

$$\phi(\Sigma_{eq}, \Sigma_m, \sigma^0, f) = \left(\frac{\Sigma_{eq}}{\sigma^0}\right)^2 + 2f\cosh\left(\frac{3\Sigma_m}{2\sigma^0}\right) - \left(1 + f^2\right) = 0 \tag{1.5}$$

where Σ_m and Σ_{eq} are the mean and equivalent macroscopic stress, respectively, σ^0 is the flow stress of the matrix and f is the void volume fraction of the hollow spheres. In an effort to obtain a better comparison between the explicit analysis of a doubly periodic array of voids that accounts for the interaction between voids as well as the non-uniform stress field and the result from the Gurson porous plasticity relation, Tvergaard (1981) introduced the parameters q_1, q_2 and q_3 in the relation (1.5) as follows

$$\left(\frac{\Sigma_{eq}}{\sigma^0}\right)^2 + 2fq_1\cosh\left(\frac{3q_2\Sigma_m}{2\sigma^0}\right) - \left(1 + q_3 f^2\right) = 0 \tag{1.6}$$

The plastic strain rate at the macroscale follows the normality rule, established by the principle of maximum plastic work of Hill (Bishop and Hill 1951) as shown below

$$\dot{\mathbf{E}}^p = \dot{\lambda}\frac{\partial\phi}{\partial\boldsymbol{\Sigma}} \tag{1.7}$$

where $\dot{\lambda}$ is the plastic multiplier. The evolution of the internal variables, namely matrix flow stress and porosity are needed in order to describe the deformation history

undertaken by the porous plastic solid. Invoking the equivalence of macroscopic and microscopic plastic dissipation, the following relation can be written for the rate of plastic strain in the matrix as

$$(1-f)\sigma^0\dot{\varepsilon}^p_{eq} = \boldsymbol{\Sigma} : \dot{\mathbf{E}}^p \tag{1.8}$$

where $\sigma^0 = \sigma^0(\varepsilon^p_{eq})$ is introduced in order to account for the hardening behavior of the matrix material and superscript *p* denotes the plastic strain when extended to analysis of an elasto-plastic hardening porous solid. Equation (1.5) is supplemented with an evolution law for the porosity which is split into two parts

$$\dot{f} = \dot{f}_g + \dot{f}_n \tag{1.9}$$

where $\dot{f}_g$ is the rate of growth of existing voids in the material and $\dot{f}_n$ is the rate of nucleation of new voids from particles. The first term is related to the macroscopic mean strain increment by virtue of conservation of mass which reads as follows

$$\dot{f}_g = 3(1-f)\dot{E}^p_m \tag{1.10}$$

where $\dot{E}^p_m$ is the macroscopic mean plastic strain rate.

Gologanu et al. (1993, 1994 and 1995) extended the Gurson model to take into account the void shape effects by analyzing a spheroidal RVE consisting of a confocal spheroidal cavity with matrix material being incompressible and obeying J_2 flow theory of plasticity. The model was extended further by Benzerga and Besson (2001) to incorporate plastic anisotropy by analyzing a hollow sphere where the matrix behavior is assumed to follow Hill's quadratic yield function with the same trial velocity field as in the original Gurson model. In recent years, constitutive relations embracing both void

shape and material anisotropy have been developed (Monchiet et al. 2008; Keralavarma and Benzerga 2008, 2010). Mear and Hutchinson (1985) studied the extension of isotropic hardening Gurson model to kinematic hardening behavior. Wen et al. (2005) extended the Gurson plastic potential to account for the effect of void size based on Taylor (1938) dislocation theory; this effect was incorporated through the matrix strain hardening behavior. Inspired by recent experimental observations (Bao and Wierzbicki 2004; Barsoum and Faleskog 2007), Nahshan and Hutchinson (2008) proposed an extension to Gurson model to overcome the model's perceived deficiency in realizing damage in cases of shear-dominated fracture in low triaxiality.

1.2.3. Void Coalescence

Beachem (1963) examined the different rupture mechanisms in ductile metals by studying the fracture surfaces in a scanning electron microscope and concluded that there were three major void coalescence mechanisms that led to rupture in ductile metals. "Normal rupture", where coalescence takes place under uniform plastic strain parallel to the direction of the tensile stress, leads to equiaxed dimples; "shear rupture", where coalescence occurs under the combined effect of plastic strain in the direction of applied stress and shear strain on a plane of maximum shear stress, leads to elongated dimples on opposite mating fracture surfaces; "tearing rupture", where coalescence occurs under nonuniform strain in the direction of the applied stress, leads to elongated dimples pointing toward the fracture origin on both fracture surfaces.

The coalescence of voids at the onset of final failure is the most complex and least understood stages of ductile fracture. This can be attributed to experimental difficulties in the observation of micro-voids coalescence stage of ductile fracture. For many years, the

incipient coalescence was treated as the final failure of ductile materials, so that less was known about the coalescence process. One of the early models proposed for void coalescence was by Brown and Embury (1973). In their model, the shear localization is triggered in the intervoid ligament when the void length is equal to spacing and 45^o lines can be drawn between neighboring voids. Another commonly used criterion simply imposes a constant critical void volume fraction at final failure (Needleman and Tvergaard 1984). In order to complement the constitutive relation, a coalescence criterion based on a critical void volume fraction has been extensively used due to the simplicity of implementation in numerical simulations. The post-coalescence stage of the ductile porous solid that takes into account the sharp loss of load carrying capacity of the material was introduced by Needleman and Tvergaard (1984) as follows

$$f^*(f) = \begin{cases} f & \text{for } f \le f_c \\ f_c + \dfrac{f_u^* - f_c}{f_F - f_c}(f - f_c) & \text{for } f > f_c \end{cases} \tag{1.11}$$

where $f^*(f)$ is the modified porosity that replaces f in equation (1.6), $f_u^* = 1/q_1$, f_c is the porosity at which coalescence initiates and f_F is the porosity corresponding to the final failure of the material. Despite the appeal of the constant void volume fraction criterion in numerical modeling, further studies on unit cell calculations showed that the onset of coalescence also depends on stress triaxiality, strain hardening and more importantly on the initial void volume fraction (Koplik and Needleman 1988). In order to remedy this lack of consideration of the role of the microstructure in the coalescence process, Thomason (1985a,b, 1990) analyzed micromechanical models of the transition of plastic deformation to localization in the ligament between micro-voids in a non-hardening material and suggested a plastic limit load criterion for the onset of voids

coalescence in the form of internal necking. Zhang and Niemi (1995) by incorporating a modified Thomason's plastic limit-load criterion for failure into GTN constitutive relation for pre-coalescence stage, were able to achieve good agreement with the unit-cell calculations of Koplik and Needleman (1988). In their results material failure was the natural consequence of the combined constitutive formulation. Pardoen and Hutchinson (2000) extended the GLD model – a modified Gurson model that accounts for the anisotropy of the void shape (Gologanu et al. 1993, 1994, 1995) – and the Thomason's plastic limit-load criterion by the means of unit cell computations to take into account the strain hardening property of the matrix material. Furthermore, they incorporated micromechanical constitutive equations governing the coalescence stage after the incipient coalescence in the form of internal necking, thereby obtaining an enhanced set of governing equations for the entire ductile fracture process which accounts for porosity, void shape, relative void spacing and strain hardening. Furthermore, Benzerga (2002) proposed a constitutive relation for the entire coalescence stage suitable for finite element implementation where modifications were made to mitigate the unrealistic predictions of Thomason's criterion for coalescence of flat voids.

Real microstructure of structural materials consists of inhomogeneities at different levels that have a significant influence on the plastic deformation and ductility. Microstructural inhomogeneities in forms of morphology, size and spatial distribution of second phase particles, and grain texture are introduced in the materials during the manufacturing processes. Understanding the different mechanisms through which these inhomogeneities affect the constitutive and failure behavior of ductile solids is of vital importance. Plastic strain localization which takes place during the deformation history of ductile solids and acts as the precursor to failure is greatly dependent on the variations of these microstructural details. With the advent of powerful experimental and

computational tools, there have been extensive studies aimed at understanding the roles of inhomogeneities at different stages of ductile deformation and damage processes. Spitzig et al. (1988) characterized the evolution of porosity, void size and shape in tensile specimens made of iron compacts with different initial porosities that resulted from different degrees of densification in processing. They noted the presence of regions with 4-7 times porosity of that in the bulk material. Using the experimental results from above, Becker (1987) introduced the inhomogeneities of initial porosity in finite element simulations of axisymmetric and plane strain deformations for two different microstructures. Becker concluded that flow localization occurs in a band between the regions of higher void fractions and the subsequent void growth and failure is limited in these localized bands. In an attempt to incorporate the real microstructure into the predictive constitutive and damage models, Ghosh et al. (2009), Chen et al. (2003), Worswick et al. (2001), and Butcher and Chen (2009) directly integrated the microstructural characteristics such as particle morphology, size and spatial distribution using digital imaging tools into a finite element framework to explicitly link the material behavior at the micro-scale to that at the macro-scale. The damage formation and evolution were shown to be very sensitive to the size and spatial dispersion of the clusters of the particles. These researchers also attempted to characterize a proper length scale for the materials they investigated by analyzing the dependence of the ductile failure process on the size of the representative volume element. The inhomogeneities at the grain level in polycrystalline materials have also been given attention recently by some researchers (Becker and Richmond 1994; Hu et al. 2011). Recently in order to overcome the limitations of finite element calculations in dealing with a complex microstructure with high level of inhomogeneities that is seen in real structural materials, a novel numerical technique based on fast Fourier transform (FFT) originally proposed by Moulinec and

Suquet (1998) was adopted to examine the effect of non-uniform local porosity on macroscopic and local responses of a rigid-perfectly plastic matrix material with a complex irregular distribution of cylindrical voids with no clusters (Michel 2001). In a follow-up investigation by Bilger et al. (2005), the effects of porosity variations in a rigid-perfectly porous solid in forms of random distribution of voids, disconnected clusters and connected clusters were examined numerically using fast Fourier transform. They realized a strong dependence of both overall and local field distributions on different microstructural pattern.

1.2.4. Strain-to-Failure Fracture Models

Due to complexity of modeling the ductile fracture on the micro-scale, macroscopic strain-to-failure models have been introduced over the past four decades to facilitate fracture prediction. These models usually contain several material parameters that need to be calibrated from experiments; strain-to-failure is determined with respect to some specimen dimension characteristics such as the gage length or cross-sectional area. With the advent of numerical tools in recent years, the simulations of the experiment have also been widely used in calculating the strain at the onset of failure. However, these methodologies of obtaining strain-to-failure suffer from strong dependence on specimen length scale or discretization scheme, and do not represent the intrinsic failure characteristics of the material. In this section we discuss the widely used Johnson-Cook fracture model as an example of this class of models.

The Johnson-Cook model (1985) is an empirical model that is written in the following form

$$\varepsilon_f = \left[D_1 + D_2 \exp\left(D_3 \frac{\sigma_m}{\sigma_{eq}} \right) \right] \left[1 + D_4 \ln \frac{\dot{\varepsilon}}{\dot{\varepsilon}_0} \right] \left[1 + D_5 T^* \right] \tag{1.12}$$

where ε_f is the strain-to-failure, σ_m / σ_{eq} is the stress triaxiality, $\dot{\varepsilon} / \dot{\varepsilon}_0$ is the dimensionless strain rate with $\dot{\varepsilon}_0 = 1.0$ s^{-1}, T^* is the homologous temperature and $D_1 - D_5$ are material constants that are calibrated from experiments at the macroscale. We will examine the applicability of the Johnson-Cook model to different materials – oxygen-free, high-conductivity (OFHC) copper and Al 6061-T6 – through measurements at different gage lengths, all the way down to the size of grains. The material constants conventionally calibrated through the strain measurements based on specimen dimensions for these materials are listed in Table 1.1.

1.3. ORGANIZATION OF THE DISSERTATION

In Chapter 2, results of an investigation of the deformation and failure process in oxygen-free, high-conductivity copper realized through electron and optical microscopy of uniaxial tension tests are described. The onset and evolution of the failure governed by plastic instability of the deformation is explained. Numerical simulations are also presented, with qualitative comparisons to the essential features of the experiment. Experimental strain measures obtained at the grain level are compared to the strain-to-failure models widely used in ductile fracture simulations.

In Chapter 3, an investigation into constitutive and failure behavior of Al 6061-T6 sheets through tension tests and flat-notched tension tests is presented. Optical and electron microscopy were used to characterize the microstructure; the onset and evolution of damage are correlated with the deformation at the grain level. The final stage of fracture was studied quantitatively. Numerical simulations are also performed to obtain

the evolution of the stress state with deformation. Comparisons with the strain measured with digital image correlation allow quantification of the material behavior in a multi-scale framework.

In Chapter 4, the process of deformation and failure in Al 6061-T6 under dominantly shear loading is explored. The strain measures at the level of the grain and the initiation of failure are examined through qualitative and quantitative microscopy. Strains in the range of 2 are observed at the grain level in low triaxiality loading conditions. A stark contrast with the modified Mohr-Coulomb fracture model (Beese et al. 2010) is shown.

In Chapter 5, the deformation and damage evolution of nodular cast iron are studied through tension and flat-notched tension tests. Metallographic quantification of the evolution of microstructure is also presented. The main features of the fracture and the active mechanisms governing the failure are presented.

In Chapter 6, we present conclusions of the role of microstructure in ductile failure process.

Table 1.1. Material constants calibrated from strain measurement based on specimen dimensions for oxygen-free, high-conductivity copper (OFHC) (reproduced from Johnson and Cook 1985) and Al 6061-T6 (reproduced from Lesuer et al. 2001).

Material constant	D_1	D_2	D_3	D_4	D_5
OFHC copper	0.54	4.89	-3.03	0.014	1.12
Al 6061-T6	-0.77	1.45	-0.47	0.0	1.60

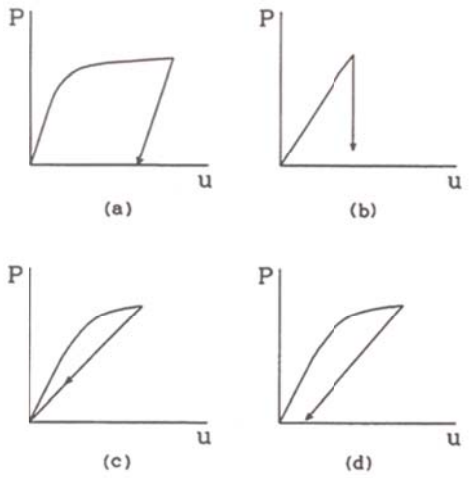

Figure 1.1. Load-elongation diagram corresponding to different types of material damage; (a) ductile damage, (b) perfectly brittle damage, (c) quasi-brittle damage and (d) combined ductile-brittle damage (reproduced from Krajcinovic 1996).

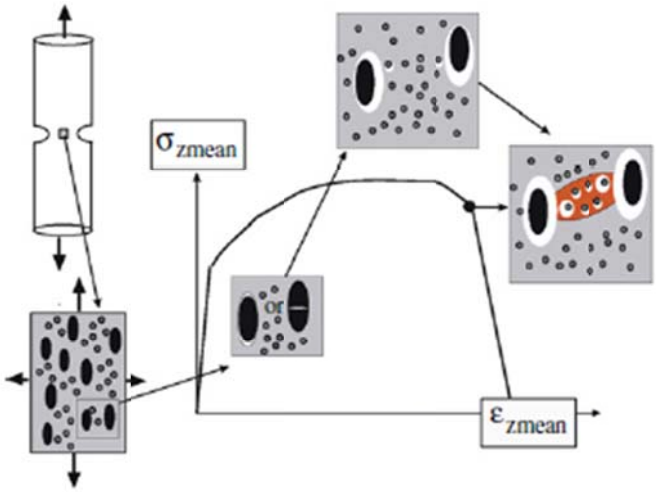

Figure 1.2. Different stages of ductile failure (Fabrègue and Pardoen 2008).

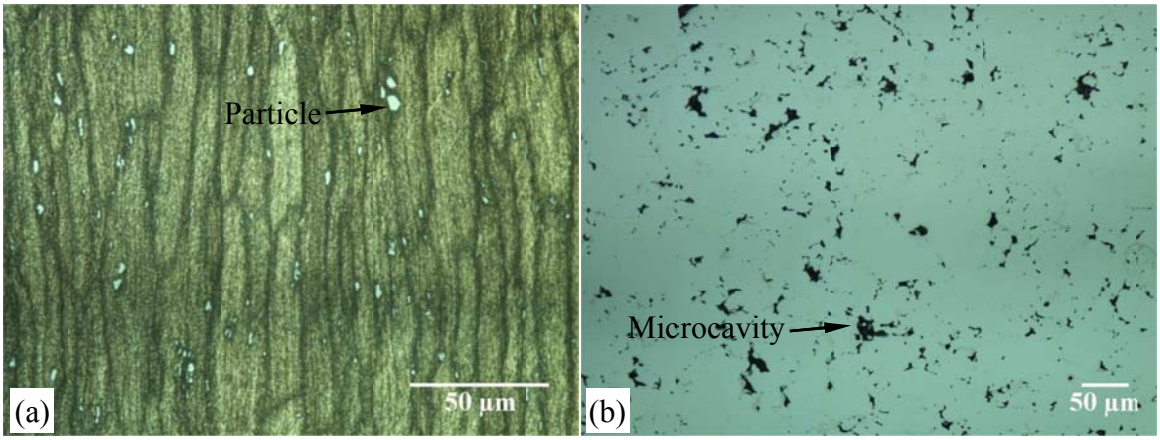

Figure 1.3. Optical micrographs showing (a) the second phase particles in Al6061-T6 sheet and (b) microvoids initially present in sintered iron.

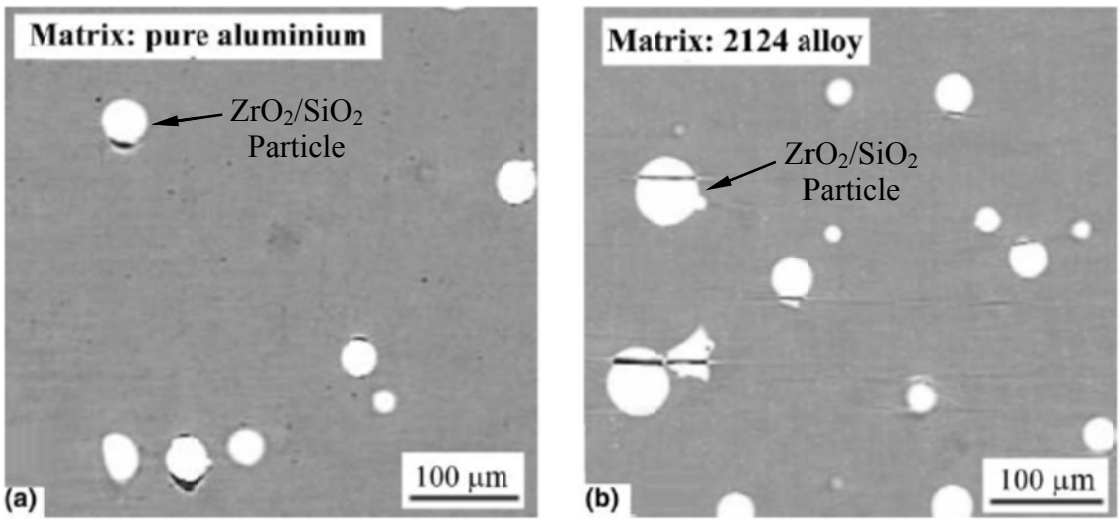

Figure 1.4. Void nucleation in two model materials; (a) matrix-particle interface decohesion in a composite made of soft matrix and hard particles; (b) particle fracture in a composite made of higher strength matrix and hard particles (reproduced from Babout et al. 2004).

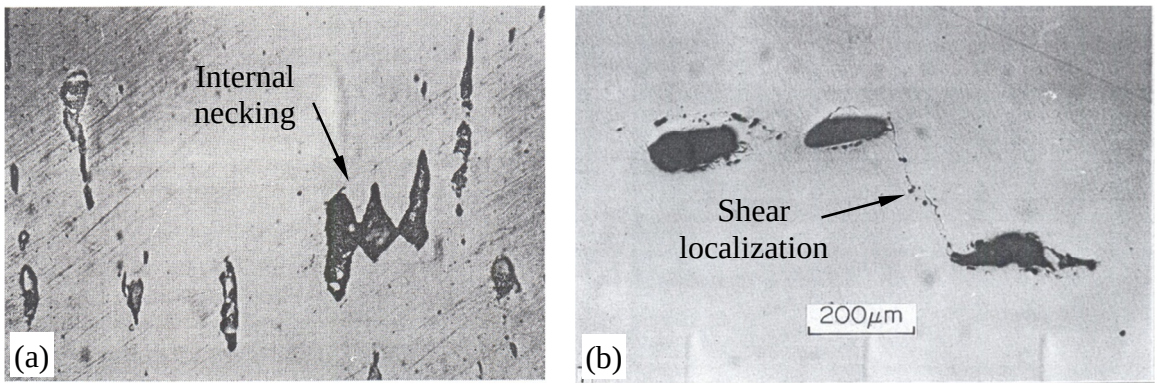

Figure 1.5. Two different modes of void coalescence in ductile materials; (a) internal necking in the intervoid ligament (reproduced from Puttick 1959); (b) shear localization in the ligament (reproduced from Hancock and Mackenzie 1976).

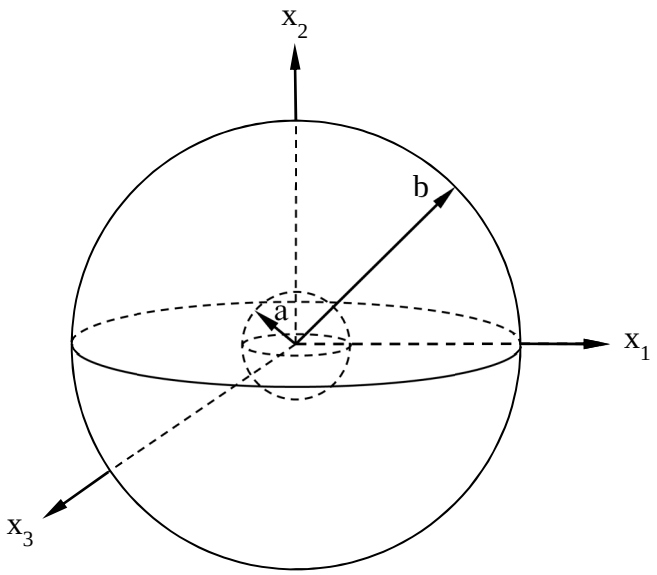

Figure 1.6. Diagram of the RVE considered in the Gurson model.

Chapter 2: Failure of Polycrystalline OFHC Copper

2.1. INTRODUCTION

Ductile failure in polycrystalline copper has been the subject of numerous investigations over the past century. Failure in this context is understood in the sense described by Orowan (1948): rupture "is a consequence of an instability of plastic deformation and occurs when the deformation becomes localized in a small part of the specimen." Progression of failure from the localized plastic deformation seldom arises from breakage of primary bonds, but from slip along crystallographic planes at the smallest scales and is generally thought to occur by void nucleation and growth at slightly larger scales. It is now well-known, since the early work of Ludwik (1926), that uniaxial tensile specimens of polycrystalline metals fail in the familiar "cup and cone" mode of fracture. Orowan (1948) showed yet another mechanism of failure – based on observations by Tipper of the formation of a polyhedral transverse channel in the neck of an aluminum single crystal specimen, he provided a mechanism of alternating slip for the formation of a crack at the center of the necked specimen. Figure 2.1 is a reproduction of the mechanism proposed by Orowan (1948). It is well-known that in plane-strain tension, the deformation localizes along the characteristics (slip lines) of perfect plasticity; these are aligned along lines inclined at 45° with respect to the direction of tension. The rectangular opening occurs where these slip lines intersect; Orowan observed that slip occurs initially along AB and CD with subsequent slip along planes EB and CF. Continuation of such alternating slip events results in an enlargement of the rectangular cavity. Orowan (1948) suggested that failure in polycrystalline materials could also occur by such alternating slip "if the plastic deformation is concentrated in thin zones around planes of maximum shear stress". This suggestion appears to have not been pursued in

more recent literature, perhaps due to the lack of experimental observations that carefully outlined conditions under which such a mechanism could be of importance. For example, Rogers (1960) examined ductile failure in OFHC copper with a (fairly large) grain size of about 1 mm; after examination of metallographic sections from uniaxial tests interrupted at various stages of neck growth, he concluded that voids were nucleated both at grain boundaries and in the interior of grains, and accumulated along lines parallel to the direction of tension, at the center of the specimen where the triaxiality was the largest; coalescence of voids resulted in the formation of a central crack. Subsequent growth of this crack occurred by concentration of shear at an angle of 30° to 40° to the tensile axis, nucleation of a large number of voids within this shear zone and their eventual coalescence; this is called the "*void-sheet mechanism*". These void sheets zig-zag across the central segment of the specimen and form the "cup" of the cup-cone fracture. Most importantly, Rogers noted that the final separation (the "cone" part) could evolve by the Orowan mechanism of ductile failure by alternating slip, although he could not rule out cleavage in the highly strained grain. Puttick (1959, 1960) also explored the basic deformation and failure mechanisms in polycrystalline copper. The material had a grain size of about 50 μm, and contained impurities that were introduced during the rolling process. These specimens developed standard cup-and-cone fractures that began with the formation of a diffuse necking localization. An image of a thickness section is shown in Puttick's paper (see Figure 2.1 in Puttick 1959), identifying voids within the necked region; the average true strain at the narrowest part of the neck can be estimated to be around 0.66. Using high magnification images, fracture and debonding of impurity particles from the copper were also identified by Puttick (1959). The formation of a macroscopic shear band and void coalescence within the shear band were also identified by Puttick (1960). These careful metallographic observations clearly revealed that the

mechanism of failure in ductile materials is the nucleation and growth of cavities in polycrystalline copper. One must, of course, exercise caution in extrapolating this conclusion to all materials, and even to copper with a different grain structure. For example, do these conclusions continue to hold when the grain size is decreased by an order of magnitude or if the level of impurities is decreased? This requires very careful material characterization at multiple scales.

Argon and Im (1975) examined a copper specimen with grain size in the range of 20 to 30 μm; this material also contained a second phase of Cu-Cr alloy with a particle diameter of around 0.89 μm. They estimated that the particles would debond at a stress level of about 993 MPa; the strain level at nucleation of cavities was found to be about 70% of the overall plastic strain at failure. French and Weinrich (1974, 1975, 1976, 1977) examined failure in commercial copper and brass in a series of publications. In a particularly interesting set of experiments, they identified that at high superposed pressure levels (French and Weinrich 1975), plastic flow localizes in shear into narrow bands and failure occurs only within these bands; this appears to be in line with Orowan's suggestion, except for the lack of transverse channels. French and Weinrich (1976) also examined the failure of α-brass with very low impurity content; they identified the formation of zones of intense shear deformation but could not observe any voids within this zone by optical examination. However, the fracture surface presented a dimpled appearance which led them to postulate that the void-sheet mechanism in the intense shear zone must have occurred very late in the deformation.

Lindholm et al. (1980) developed a torsion apparatus for subjecting specimens to large strain levels at various strain rates; they examined the shear response of thin-walled tubes of annealed OFHC copper in the strain rate range of 0.009 s^{-1} to about 330 s^{-1}. The grain size in the specimen ranged from about 25 to 35 μm. Specimens strained at rates

below 10 s^{-1} exhibited positive strain and strain-rate hardening; more importantly, *no localization of deformation was observed even at a true (logarithmic) strain level of about two*. At strain rates greater than 174 s^{-1}, localized shear deformation was observed at a strain level of about 1.6. Pardoen and Delannay (1998) examined the failure response of commercial Cu containing 0.2% by volume of copper oxide inclusions; the inclusions were ellipsoidal with major and minor diameters averaging 1.63 μm and 1.03 μm, respectively. They found that debonding between the copper oxide particles and the copper matrix occurred almost at the onset of plastic deformation and that failure in this material was due to the growth and coalescence of voids. Porosity measurements were obtained from density measurements; their observations indicated that the strain at failure was 0.95 for the drawn material and 1.23 for the annealed material; the final porosity was also determined to be 0.009 and 0.014 respectively for the drawn and annealed materials. Pardoen and Delannay evaluated the fitness of different porous plasticity models to capture this response. It would appear that the lower strain at failure observed by Pardoen and Delannay (1998) in comparison to the pure shear measurements of Lindholm et al. (1980) is a reflection of the role of stress state and defects in localizing deformation and failure. However, French and Weinrich (1977) had also examined commercial copper with a large concentration of 3 μm diameter copper oxide particles but found that the mechanisms of deformation within zones of shear localization were very similar to that in α-brass with very few inclusions. They found that only those voids that were within the shear zones grew and coalesced to form the fracture. There are numerous other investigations of the compressive response of OFHC copper at high strain rates (see for example, Follansbee and Kocks 1988; Tong and Clifton 1992; Nemat-Nasser and Li 1998), but most of these explore constitutive behavior and do not address the issue of ductile failure.

In the present work, our objective is to provide a fundamental examination of the deformation and fracture processes in high purity, oxygen-free, high-conductivity copper. The main reason for such an examination is that since the methods of characterization of microstructural features have improved significantly in the past few decades, the ability to make quantitative observations of failure phenomena at multiple scales has increased enormously. For example, we combine digital image acquisition technology, image compositing, and statistical processing methods to obtain quantitative information about strains down to the level of individual grains. Using such techniques, we obtain estimates of grain rotations and strains over the entire region of localized deformation. We examine OFHC Copper as a material with very few impurities; follow-on studies will explore materials with a distribution of second phase particles.

In this Chapter, we describe the deformation and failure response of OFHC copper. The experimental methods used in this investigation are described in Section 2.2. The response of the material in a uniaxial tensile test is described in Section 2.3. The macroscopic response is rather well-known; the deformation localizes through a necking instability. Through a series of interrupted tests, a number of specimens at different stages of neck development were obtained and examined to determine the strain evolution quantitatively. The evolution of deformation localization and strains within the grains is also described in Section 2.3. The nucleation and growth of a single central cavity through the Orowan mechanism of alternating slip rather than homogeneous void growth is demonstrated to be the dominant mode of failure in this material. The failure mechanisms are examined through scanning electron microscopy. Finally, numerical simulations performed within the framework of continuum plasticity are described in Section 2.4; these results are used to outline the conditions at the onset of nucleation of the central cavity and to identify the mechanisms of growth (enlargement) of the cavity.

2.2. EXPERIMENTAL METHODS

The material used in this investigation is an oxygen-free, high-conductivity copper, with the designation Cu-102 (3/4 hard); this material is used as an example of a ductile material that contains very few impurities in the form of precipitates, second-phase particles or grain-boundary phases. The raw material was purchased from a 99.95% pure, ¼ inch thick plate stock and cut to ½ x ¼ inch cross-sectional dimensions. The x-y-z coordinates are taken to be aligned along the longitudinal (rolling), width (transverse) and thickness (short-transverse) directions. The initial grain size distribution was obtained by etching the specimen in Copper Etchant #1 for 45 seconds; this makes the grains clearly visible. Representative optical micrographs of the copper stock in the x-y, x-z and y-z planes are shown in Figure 2.2a-c. Quantitative image analysis was performed using the software NIH ImageJ in order to determine grain size distributions; the lengths of the major and minor axes of an equivalent ellipse were extracted from this measurement. The distribution of the minor axis of the equivalent grain along the x-z plane is shown in Figure 2.2d; the mean value and standard deviation of the major and minor axes of the equivalent elliptical grain distributions are listed in Table 2.1. The rolled copper has an anisotropic grain size distribution. In particular, the grains are elongated in the x-direction, with mean values in the range of 80 to 90 μm; they are also wider in the y-direction (with a mean of 40 to 60 μm) in comparison to the z-direction (with a mean of 26 μm). Therefore, we expect the material to exhibit transversely anisotropic response. We note that this characterizes only the geometry of the grains; evolution of grain orientation and crystallographic texture occurs at large deformations as indicated by the plane strain compression test simulations reported by Anand and Kalidindi (1994). Such crystallographic texture evolution has not been examined in the present work.

Dog-bone type uniaxial tensile specimens were machined from the rolled plate stock. Specimens of rectangular cross-section (w = 11.14 mm, gage length was 76.20 mm, and t = 6.46 mm) were machined for these tests; the geometry of the specimen is shown in Figure 2.3a. In some of the tests, the rectangular stock was used "as-is", without narrowing down the gage-section; this did not affect the sequence of events observed. Two specimens with a circular cross-section (diameter = 5.55 mm) machined from the same stock were also tested.

Damage evolution in these copper specimens was examined through optical and scanning electron microscopy on interrupted tests. In order to obtain a detailed picture of the deformation at the level of grain size, the specimens obtained from interrupted tests were sectioned, polished, and etched to reveal the grain boundaries in the x-z and x-y planes; images of the grains at different macroscopic strain levels were analyzed to obtain grain orientations and strains in a statistical sense. There has been a recent spurt of activity in grain-based strain evaluation, using the digital image correlation technique (see for example: Carroll et al. 2010). In particular, these techniques rely on obtaining an image of the grains, with an embedded or superposed grid or speckle pattern deposited on the specimen surface, both before and during different stages of deformation. The deformed image is then correlated with the undeformed image in order to extract the surface strain field. The thrust of these studies has been to examine the nature of heterogeneity of deformation at the grain level and to identify the typical size of the representative volume element over which homogenization may be performed in order to apply continuum theories of material behavior. In contrast, our objective is to track the strains at the individual grain level, to correlate these strains with onset of microscopic failure processes, and to make a correlation with macroscopic strain localization in a

statistical sense; this requires destructive tests and can be accomplished only through interrupted tests.

2.3. RESULTS AND DISCUSSION

Numerous investigators have observed and modeled the response of ductile materials under uniaxial tension. We summarize the main observations in order to place the present results in the proper context. Under uniaxial tensile loading, the deformation remains homogeneous even after the onset of plastic deformation, if the material exhibits a strain-hardening response. With continued straining, a limit load is reached at the Considère point with a diffuse neck appearing almost immediately beyond this strain level. As the neck grows further, the triaxiality (defined as the ratio of the mean stress to the effective stress) increases from one third to just around one; cavities are expected to nucleate at the center of the necked region, grow and coalesce into a crack like object; further failure is influenced by the growth of this crack. When the remaining ligament becomes small, shear localization occurs at about 45°; material separation in this shear zone occurs by a "void-sheet" mechanism – collective growth and coalescence of voids in this shear localized plane. In specimens of circular cross-section, the result is the commonly observed "cup and cone" fracture. In specimens that are of rectangular cross-section, another instability is observed: within the diffuse necked region, highly localized shear bands develop in the x-z plane; such localization occurs most clearly in the plane-strain tension tests (see Clausing 1970; Anand and Spitzig 1980; Spencer et al. 2002, for experiments and Tvergaard et al. 1981 for simulations). Further deformation is concentrated within the shear bands resulting in eventual failure along these shear bands (also by the void-sheet mechanism). In the present work, cylindrical specimens of

rectangular and circular cross-sections are used; the progression of deformation is similar to that reported by others. The main point of departure, and therefore the focus of the present work, is on the development of final failure.

2.3.1. Uniaxial Tension Test

The results of uniaxial tensile tests on OFHC Copper specimens are discussed first. Figure 2.3 shows the nominal stress (force/initial cross-sectional area) vs. normalized crosshead displacement variation that is typical of such tension tests. Since this material exhibits very little strain hardening, uniaxial deformation becomes unstable at very small global strain levels; corresponding to the peak load at point A, a diffuse neck develops at some location in the specimen and all further deformation occurs within the necked region. Beyond this point, the overall load decreases gradually at first and then more rapidly towards final failure. The question of when and what kind of damage, if any, occurs within the highly deformed necked region of the specimen must be examined carefully in order to develop appropriate failure models. In order to accomplish this, specimens were unloaded after deforming them through increasing amounts of strain, and sectioned to reveal the deformation across the x-y and x-z planes of the specimen. These specimens were then prepared for metallographic examination by mounting, polishing and etching in Copper etchant #1, following standard procedures. Figures 2.4-2.7 show images of the x-z and x-y sections of the specimen at different stages of neck evolution; these images correspond to points labeled as B, C, D, and E in the load-elongation diagram in Figure 2.3. These images were obtained in a Nikon Eclipse microscope at a magnification of 200; for each specimen, between eighty and one hundred images were captured over a large region and assembled into one high-resolution

image covering the entire necked region. As a result of the etching process the grain boundaries are easily identified in these images; visual observation provides ample evidence of large strains, large rotations in the region of the neck, and a shear localization in certain areas of the neck. It is evident that a highly nonhomogeneous state of strain is established in the necked region. There are a number of striking observations that can be made from these micrographs.

- Figure 2.4 shows an image of an x-z section across the necked region of the specimen corresponding to the point B in the load elongation diagram. The diffuse neck has formed, but the shear localization across the specimen has not yet appeared. By tracing lines tangent to the grains, the early stage images can be used to visualize the streamlines of plastic flow. As shown by the highlighted white rectangle, some grains near the specimen free surface exhibit early traces of shear localization.
- The x-z and x-y sections across the necked region corresponding to the point C in Figure 2.3 are shown in Figures 2.5a and 2.5b; the grain width (dimension in the specimen thickness direction) can be seen to have decreased significantly all over the necked region from its original size shown in Figure 2.2. Large grain rotations can also be observed in these images. We will evaluate the grain orientation variation and the strains quantitatively in Section 2.3.2 to determine the local strains at the level of the grains.
- The macroscopic deformation appears to be concentrated along the two characteristics of plane-strain plasticity (Figures 2.5a and 2.5b show the x-z and x-y planes, respectively). Very large grain rotations and significant thinning of the grains can also be seen in this image in Figure 2.5a. A high magnification image

of the region marked with a white rectangle labeled 'I' in Figure 2.7 is shown in Figure 2.8 which shows the strain localization zone. Such concentrated shear zones have been observed in high purity copper by French and Weinrich (1975) who performed tensile tests at high pressures; micrographs of etched longitudinal sections shown in their work bear significant similarities to the ones shown in Figure 2.5a.

- Quite remarkably, a *single* cavity is nucleated at the center of the necked region (Figure 2.5a); it is well-known from Bridgman's early work that a high triaxial stress arises at the center of the neck[1]. In the present experiment, due to the intersection of the two planes of shear localization at the center of the specimen, an even larger triaxiality is expected; hence voids, if they nucleate, must do so at this location. However, the surprising observation is that unlike the typical nucleation of multiple ellipsoidal voids (of the type shown by, for example, Puttick 1959), a prismatic void with a rectangular cross-section appears. The macroscopic boundaries of the rectangular void appear to be oriented along the plane-strain slip directions. The x-y section of the specimen along the dashed red line in Figure 2.5a is shown in Figure 2.5b; this reveals the prismatic nature of the cavity. However, it is not clear that the macroscopic field is the driver in the generation of the rectangular cavity. Even in specimens with an initially circular cross-section, the nucleation of the central cavity breaks the global symmetry and a rectangular prismatic void of the type shown in Figure 2.5a was observed! The local symmetry due to grain orientation or anisotropy effects appears to dictate the

[1] Numerical simulations described in Section 2.4 indicate that the triaxiality at the center of the necked region in the specimen is about 1 to 1.05.

initial development of slip and hence determine the orientation of the macroscopic rectangular cavity.

- Beyond nucleation of the central rectangular cavity, its further growth is even more remarkable in its self-similarity – as shown in Figures 2.6a and 2.7, the rectangular cavity simply becomes larger! Figure 2.6b shows the x-y plane section of the specimen across the dashed red line in Figure 2.6a; the prismatic nature of the cavity is evident from this figure. A small number of ellipsoidal voids are observed to be distributed at grain boundaries in the vicinity of the enlarging central void. However, it is clear that void growth and coalescence along the lines required for applicability of homogenized models of porous plasticity cannot be the applicable failure mechanism. In fact, outside of the growing rectangular cavity, very little damage is observed in the specimen. Spencer et al. (2002) noted a similar polygonal cavity in the interior of an annealed Al 5754 Al-Mg alloy with very low impurity content. The failure mechanism appears more likely to be along the lines of the alternating slip conjectured by Orowan (1948); we will explore this further through microscopy in Section 2.3.3.
- Comparison of the grain size across the specimen thickness in Figures 2.6a and 2.7 points to a very important aspect of the material response. The concentration of strain along the shear bands and the relatively large plug of lightly deformed material are easily observed in Figure 2.5a; for a very low hardening material, after formation of the shear localization, further deformation should occur only in the shear band and the plug should simply move as a rigid body. For example, numerical simulations of the plane-strain tension test by Tvergaard et al. (1981) show the formation of such an unloaded wedge. This would also be the case if the void-sheet mechanism is the appropriate failure mechanism. However, in our

experiment, with further deformation of the specimen, the material that was originally within the plug region continues to get sheared and at the end stage of the deformation in Figure 2.7, the plug region has disappeared completely. One must seek a different mechanism of cavity expansion to allow continued straining of the material in the "plug" region.

- At final fracture, the nearly rectangular prismatic shape of the cavity is maintained on the fracture plane as shown in Figure 2.7. From identification of the grain flow lines on the broken specimen, the corresponding points on the upper and lower parts – labeled with upper and lower case letters in Figure 2.7 – can be identified quite easily. This is seen more clearly in the magnified image of the region labeled 'II' in Figure 2.5a, shown in Figure 2.9; the red lines indicate the alternating slip path taken by the crack, and the white dashed lines show the cavity expansion. It appears that the 90° corner is growing self-similarly, like a crack, but the growth appears by the Orowan alternate slip mechanism; we will examine the fracture surface in detail to obtain evidence for this mechanism.

It should be noted that we have only looked at the topological evolution of the grain; crystallographic changes have not yet been examined. The latter is necessary to reveal the planes and orientations along which slip occurs in order to accommodate growth of the rectangular cavity. We now turn to each one of these observations and provide further qualitative and quantitative interpretations.

2.3.2. Measurement of Grain Rotations and Strains

We develop simple schemes to convert the qualitative observations discussed above into quantitative measurements of grain rotations and grain size measurements. The grain size measurements can be interpreted in terms of an average strain measure; note that this can be done only in a statistical sense since we have images of the grain only from interrupted tests. This is accomplished using the following procedure: first, the average and standard deviation of the grain size in the initial microstructure were estimated from the images of the kind shown in Figure 2.2 and are indicated in Table 2.1. Next, the location of each grain boundary was identified visually along horizontal lines such as Lines 1-3 in Figure 2.5a and Line 4 in Figure 2.7 and captured into a data file using a MATLAB code. Far away from the neck, the grain boundaries are all nearly vertical (along the rolling direction). At the minimum thickness location, the grains are once again vertical. However, the regions in between the two clearly exhibit large grain rotations within the shear bands. At every grain boundary, the slope of the grain boundary was also measured by identifying three points in the neighborhood on the grain boundary and obtaining the best fit slope. Such grain orientation measurements are necessary to obtain proper estimates of the strain in the direction parallel and perpendicular to the grains.

Strain estimation requires a bit more care; the grain size along each horizontal line was estimated from the manually identified grain boundary locations. The distribution of the equivalent ellipse minor axis along Line 4 in Figure 2.7 is shown in Figure 2.10; for comparison, the distribution in the x-z plane of the unstrained material is also shown in this figure. It is clear that the average value of the equivalent minor axis that was in the range of 26 μm in the initial microstructure has decreased to about 4 μm within the shear

band[2]. While this is indicative of a large strain, it represents an average over the entire length of Line 4; but even larger strains must occur within the bands; therefore, we extract a statistical measure of the *local* strain. The variation of the grain size across the Lines 1-3 in Figure 2.5a and Line 4 in Figure 2.7 was obtained, and divided by the mean grain size in the x-z direction to obtain an estimate of the strain in the thickness direction $\varepsilon_t = \ln\left(t/\hat{T}\right)$, where $\hat{T}$ is the mean initial grain size and t is the size of the deformed grain; assuming that the strain in the width direction (y-direction) is zero[3], the equivalent plastic strain can be estimated to be $\varepsilon_{eq} = \left(2/\sqrt{3}\right)\ln\left(\hat{T}/t\right)$; this variation is plotted in Figure 2.11 as open symbols. Note that there is quite a large scatter; this, however, does not arise from errors in experimental measurements. Rather, this is inherent in the process, since we divide the current grain size by the average initial grain size. In order to interpret this strain data better, the deformed grain was averaged over ten grains to obtain the mean deformed grain width, $\hat{t}_{10}$ and the standard deviation, $\Delta\hat{t}_{10}$. Then best estimate for the true strain in the thickness direction, and its standard deviation are obtained as $\bar{\varepsilon}_t = \ln\left(\hat{t}_{10}/\hat{T}\right)$ and $\Delta\varepsilon_t = \left[\left(\Delta\hat{T}/\hat{T}\right)^2 + \left(\Delta\hat{t}_{10}/\hat{t}_{10}\right)^2\right]^{1/2}$, respectively, where $\Delta\hat{T}$ is the standard deviation of the initial grain size; the corresponding equivalent plastic strain can be estimated to be $\varepsilon_{eq} = \left(2/\sqrt{3}\right)\ln\left(\hat{T}/\hat{t}_{10}\right)$. The variation of this estimate of the equivalent strain across the Lines 1-3 of Figure 2.5a, and Line 4 of Figure 2.7a is shown in Figure 2.11 by the red solid lines; the estimated standard deviation is within the range of 0.5 – 0.8. Of particular interest are Line 3 that corresponds to the tip of the rectangular cavity tip and Line 4 that passes through the shear band in the most deformed stage observed in the present tests. The maximum strain in the notch tip in Line 3 is estimated to be

---

[2] The effect of grain rotation has been corrected, and the deformed grain thickness was calculated in the rotated frame of the grain.

[3] This assumes plane-strain conditions, which are only approximately satisfied in this rectangular cross-section. Nevertheless, this represents a lower bound for equivalent strain estimate.

$\varepsilon_{eq}\big|_{\max} = 2.5 \pm 0.5$ and decays away from the notch. Large strains and strain gradients arise in the shear band as readily identified from Figure 2.11. The maximum recorded strains within the shear band are about $\varepsilon_{eq}\big|_{\max} = 3.75 \pm 0.5$. *Remarkably, it should be noted that there is no sign of material failure/damage within the shear banded region by any mechanism such as cavitation or cleavage at these extremely large strain levels and therefore we may only take this estimate to be a lower bound for the failure*.

The large local strains measured above are in stark contrast to reported strain-to-failure values based on measurements averaged over the specimen diameter. The failure strain, ε_f for the Johnson-Cook failure criterion for isothermal conditions is written in the following form: $\varepsilon_f = \left[D_1 + D_2 \exp\left(D_3 \sigma_m / \sigma_e\right) \right] \left[1 + D_4 \ln\left(\dot{\varepsilon}/\dot{\varepsilon}_0\right) \right]$, where σ_m is the mean stress, σ_e is the von Mises effective stress, $\dot{\varepsilon}$ is the strain rate, $\dot{\varepsilon}_0$ is the reference strain rate (taken to be unity) and D_1 to D_4 are material constants. The material constants for OFHC copper are: $D_1 = 0.54$, $D_2 = 4.89$, $D_3 = -3.03$, and $D_4 = 0.014$ (Johnson and Cook 1985). The variation of the failure strain with triaxiality $T = \sigma_m / \sigma_e$ is shown in Figure 2.12. This strain-to-failure is consistent with the reports of Puttick (1960) and Pardoen and Delannay (1998) for uniaxial tension.

Now, let us consider the strains measured at the grain level. From the numerical analysis discussed in Section 2.4, the triaxiality along Line 4 of Figure 2.7 is expected to be around 2/3; the measured maximum strain level is around $\varepsilon_{eq}\big|_{\max} = 3.75 \pm 0.5$; but there is no hint of failure or even damage in this region indicating that the strain-to-failure is even higher. On the other hand, along the Line 3 in Figure 2.5a, the triaxiality is expected to be as high as 3, in the vicinity of the notch (similar to that near a crack) and to decay away from this point. The average strains measured are around $\varepsilon_{eq}\big|_{\max} = 2.5 \pm 0.5$; since the rectangular cavity grows with continued loading, it might be appropriate to suggest that the strain to failure at high triaxiality is in this range. We

conclude that strain measures averaged over some specimen length (gage length, diameter/thickness etc) are not representative of the local strain to failure and should be used with great caution when simulating local failure. In particular, what is commonly taken to be an experimental measure of the strain-to-failure is merely an average over the specimen dimension and is not suitable as a calibration of the local strain to failure. The strain measured in the present work provides a lower bound on failure and is a better estimate of the strain to failure since it is based on measurements at the level of the grain; we will explore this further in Section 2.4.

2.3.3. Mechanism of Growth of the Central Rectangular Cavity

In order to determine the mechanism of growth of the rectangular cavity, the fracture surface was examined in a scanning electron microscope. A low magnification SEM image of the fracture pattern, viewed in the x-direction is shown in Figure 2.13a. The fracture surface exhibits two distinctly different surface features; points corresponding to labels ‘a’, ‘b’, ‘c’ and ‘d’ in Figure 2.7 are marked on the fractograph as well. The fracture surface from ‘a’ to ‘b’ is slanted with respect to the x axis by about 45°, while the fracture surface from ‘b’ to ‘c’ is oriented at different angles with respect to the x-axis. Higher magnification images of the two types of surfaces are shown in Figure 2.13b to 2.13e. The slanted fracture surface was optically reflecting, with very few visible defects; scanning electron micrographs of this surface shown in Figures 2.13b, 2.13d and 2.13e at increasing magnifications also reveal a very smooth surface. Dimples that are characteristic of void nucleation, growth and coalescence are not seen on this surface. Also, there is no evidence of cleavage facets on the fracture surface; in fact, there are no visible traces of the grain boundaries that can be observed! There are a few

isolated voids; we infer from optical microscopy on the x-z planes that these are at the grain boundaries. These voids do not seem to play any role in the fracture; the fracture plane merely slices through the voids or the voids are created after the fracture surface is formed. At extremely high magnification (Figure 2.13e), the fracture surface exhibits a terraced appearance; the steps appear to be about 50 to 200 nm in width, the height of the steps is not resolved in this imaging scheme, but one suspects that this is of the same order. These features suggest that the failure on the shear planes must have occurred by Orowan's alternating slip mechanism as illustrated in Figure 2.9. In contrast to this, the fracture surface between 'b' and 'c' in Figure 2.13 is fully dimpled; this is the typical surface expected from the void nucleation, growth and coalescence mechanism of fracture. It must be noted that, in fact, the SEM image is a projection of the entire surface between 'b-g-c' as labeled in Figure 2.7. The optical image of the x-z plane clearly indicates that there are very few voids just below the fractured surface 'b-g-c' and therefore the voids and dimples observed in Figure 2.13 appear only very close to or on the fracture plane.

It is clear that there are two mechanisms for the extension of the central cavity – one driven by shear and the other by cavity growth. It remains to resolve the sequence of their occurrence and the mechanism of shear induced enlargement of the rectangular cavity. We sectioned the specimen unloaded from the point D, and observed the fracture surface; it exhibits predominantly the shear dominated growth of the rectangular cavity implying that the void dominated crack growth is a later event. We now illustrate the Orowan mechanism governing the nucleation and growth of the single rectangular cavity, and then present an argument based on grain rotations for the generation of the dimpled fracture surface. This will be substantiated through a simple numerical simulation in Section 2.4 that makes the proposed mechanisms plausible. A schematic diagram of

rectangular cavity expansion by the alternate slip mechanism is shown in Figure 2.14. At two of the tips of the rectangular cavity, labeled A and B, the tensile stress concentration is quite large. However, at these locations the grains are oriented parallel to the direction of maximum tension; furthermore, these grains have undergone very large strains (greater than 2) and therefore significantly strain-hardened. Cleavage fracture is difficult (and there is no fractographic evidence for this), but separation could occur by crystallographic slip processes. Of course, the local slip planes will certainly not be aligned with the global alternating slip directions illustrated in Figure 2.14, and therefore the macroscopic slip will be stepped along crystallographic planes; we believe that the stepped appearance of the fracture surface is a reflection of this process. In contrast, at the other two tips of the rectangular cavity, labeled C and D, the maximum tension is significantly lower; hence, these two tips do not "grow" in the early stages of deformation. However, the grains at these locations are oriented nearly perpendicular to the direction of maximum local tension; therefore, there is the possibility for cracks to grow along the grain boundaries by nucleation of cavities. The largely dimpled fracture surface seen along 'b-g-c' is then the result of cavity growth and coalescence in this region.

2.3.4. Surface Roughness Generation at Large Deformations

The outer surfaces of the specimen exhibit a dimpled, orange-peel type appearance (see the scanning electron micrograph in Figure 2.13a); here we examine the mechanism of formation of such surface texture. Continuum analysis of stability of deformations near a free surface, such as the bifurcation analysis of Hutchinson and Tvergaard (1980), has identified the onset of surface instabilities on a half space under

plane-strain conditions; their results indicate that for a power-law hardening material, $\sigma = k\varepsilon^n$, surface instabilities may be triggered when the strain exceeds a critical level that depends on the strain hardening exponent n (beyond the Considère limit). For the OFHC copper considered in the present work, $n = 0.016$; the bifurcation analysis of Hutchinson and Tvergaard (1980) indicates that surface instabilities are to be expected when the strain parallel to the surface reaches about 0.094. It is also well-known that plastic deformation causes significant changes in the surface roughness; for example, Shimizu and Abe (2001) have examined the change in roughness by using topographic measurements. More recently, Stoudt and Hubbard (2009) showed that the surface roughness in an aluminum alloy increased from sub-micron levels to something in the range of ±10 μm as the strain increased to near the failure levels. Such roughening is clearly due to variations in the grain level strain evolution; these fluctuations can eventually lead to strain localization. The dimples observed in the copper specimens are of similar origin. In this section, we examine the mechanism of formation of the surface texture and demonstrate that for the OFHC copper, this is *fundamentally* a process of creation of new surfaces by the alternating slip mechanism of Orowan.

High magnification images of the surface of the necked region of the specimen are shown in Figure 2.15; the source locations of these images are marked by the white rectangles in Figures 2.4, 2.5a (Rectangle I) and 2.7 (Rectangle II). Even at the early stages of overall straining of the specimen, the surface grains indicate large gradients in grain rotation as can be seen in Figure 2.15a inside the highlighted box; there is just a hint of onset of strain localization in this figure. As global straining and the diffuse neck growth continue, deformation localizes at numerous points on the specimen surfaces; this is exemplified by the region shown at high magnification in Figures 2.15b and 2.15c. The dashed white line in Figure 2.15c indicates the “shear band” across which there exist

large gradients in the grain rotations; from changes in the grain width, one can also infer that the strains are significantly larger inside the band than outside, as already discussed in Section 2.3.2. Other similar shear bands in different stages of development are visible all along the surface of the specimen as one may verify from the high resolution images in the Supplemental Files section of this dissertation. After further straining, a crack appears between grain boundaries at the location indicated by the arrow in Figure 2.15c. Such cracks appear to have little to do with the overall failure of the specimen since the central rectangular cavity dominates the overall failure of the specimen as discussed in Section 2.3.3.

Careful examination of the specimen surface and correlation to these sectioned images indicates that the dimples observed on the surface are really the creation of new surfaces at the locations where the shear bands intersect the free surface. As indicated earlier, by tracing lines tangent to the grain boundaries, one can obtain the streamlines of plastic flow; two such streamlines are indicated in Figure 2.15b by the red dashed lines. Noting that one streamline comes extremely close to the specimen free surface at this loading stage, and that the other one cuts into the free surface, we conclude that a new surface must have been created between the points labeled ‘a’, ‘b’ and ‘c’. Another way of explaining this is to note that these streamlines correspond roughly to the tenth and fourteenth grains from the specimen free surface at locations that are far away from the point ‘b’, but at this location, one streamline comes to a free surface, while the other streamline is at the second grain from the surface at ‘b’; this is only possible if the other twelve grains separated, created new surfaces and rotated away to form the line segment from ‘a’ to ‘b’ and from ‘b’ to ‘c’. High magnification scanning electron micrographs of the regions between ‘a-b-c’ indicate a stepped (or terraced) surface similar to that shown in Figure 2.13e, suggesting that the alternating slip mechanism of Orowan is the

operating mechanism as well in creating the free surfaces; this new surface presents an extremely highly reflecting surface and is the reason for the textured surface appearance. The best example of the Orowan mechanism can be seen on the free surface on the right side of the neck in Figure 2.6a. Since we observe numerous such surface localizations, but only one set of shear bands that go across the specimen, we surmise that the nucleation of shear localization must appear at the surface of the specimen first; further investigations are necessary to confirm this conjecture.

2.4. NUMERICAL SIMULATIONS

We perform a numerical simulation of the uniaxial tensile test; quantitative comparison of this simulation to the experiments is extremely difficult. First, it is very difficult to obtain a properly calibrated plasticity model that can be extended to the large strain levels that have been measured at the grain level. Second, the grain distribution measurements above indicate significant initial anisotropy; furthermore, the large strains and rotations induce an evolving anisotropy as well. Third, it is not clear how the alternating slip mode of failure can be modeled numerically. Nevertheless, based on our conjecture that the material must continue to strain harden even at large strain levels, we use a simple power-law model for the response of copper; in the absence of a calibrated model, we are forced to ignore the anisotropy of the material. Failure is handled by a critical strain-to-failure criterion, although it is clear that this is deficient in the sense that it is scale sensitive; we motivate its use by observing that no significant damage was observed in the copper specimens at regions away from the failure planes. Furthermore, grain-level strains measured in the experiments provide a suitable length scale over which this failure criterion may be applied. Since we know that the Johnson-Cook model

underestimates the local strain to failure, we attempt to mimic the experimentally observed behavior discussed earlier: we assume that no failure occurs as long as the triaxiality is below unity and that for larger triaxialities, failure is triggered at a constant effective strain level of 2.5 (see Figure 2.12). It should be evident that the immediate consequence of this criterion is that failure will be suppressed along the shear bands, but at the center of the specimen, where there exists a triaxiality of nearly unity, nucleation of a cavity will be triggered. A plane-strain simulation is performed with the aim of identifying the stress state at the four corners of the rectangular cavity to help in understanding the shear dominant crack growth mechanism at two of the tips while triggering void dominant crack growth at the other two tips.

The uniaxial tensile specimen is discretized with a graded mesh that contains a fine mesh region where the necking localization occurs; linear elements, with reduced integration (CPE4R), are used in the formulation; the simulations were performed in ABAQUS v6.9 Explicit. The top boundary was assigned a constant normal velocity and zero lateral displacement; the bottom boundary was given zero normal and lateral displacement; zero traction was specified on the lateral boundaries. In order to study the effect of spatial discretization on the numerical results, three mesh densities in the expected necked region were considered – mesh 1, with 40×80 elements (in z and x directions, respectively); mesh 2, with 200×400 elements and mesh 3 with 400×400 elements; the smallest element size corresponds to 90, 18 and 10 μm, respectively. Evolving texture and anisotropy are ignored, and the standard J_2 incremental plasticity theory with a power law hardening response (with $n = 0.016$) is used to represent the material behavior. Since the element size is of the order of the grain size, the imposition of a strain-to-failure based on grain based estimates discussed above should be an acceptable approximation.

The variation of the nominal stress vs. normalized gage displacement from the plane strain simulation cannot be compared quantitatively with the experimental result, but exhibits all the qualitative features (see Figure 2.16). In particular, the appearance of the peak load at point A, and the gradual drop in load as the diffuse necking localization grows (until the point labeled B in Figures 2.3) are predicted; it should be noted that this response corresponds to plastic deformation and no damage/failure model is necessary to replicate these aspects of the response. Quantitative comparison is not possible in the absence of proper calibration of the strain hardening behavior as well as tracking of the anisotropy and texture evolution. From Figure 2.16, it is observed that the response from three different meshes fall on top of each other until the onset of the second drop in the loading response; after this point mesh 2 and mesh 3 give very close response. In light of the consistency obtained from the two fine meshes, the results using mesh 2 are used in subsequent discussion.

Contour plots of the equivalent plastic strain, the stress triaxiality, and the maximum principal stress are shown in Figure 2.17 at four different stages of loading – diffuse necking, shear localization and rectangular cavity formation, growth of the rectangular cavity, and final separation. It is clear that a neck appears first (Figure 2.17a), with an overall shape that is comparable to that seen in the experiment (Figure 2.4). This is followed by the emergence of the shear localization within the necked region (with some hint of this already present in Figure 2.17a), again similar to the experimental observation in Figure 2.5a, and also similar to the simulations of Tvergaard et al. (1981). At this stage, the stress-state in the center of the specimen has a triaxiality of around unity and the failure criterion is activated in the central part of the specimen; since we use an element deletion scheme to impose this failure criterion, elements in the central region begin losing their ability to carry stress sequentially, opening up a central cavity. This

cavity can be observed in Figure 2.17b. This causes an immediate redistribution of stresses in the vicinity of the cavity; the maximum principal stress contour plot in Figure 2.17e shows the concentration near the equatorial tips; at the polar tips, the maximum principal stress is still tensile, but significantly lower. The triaxiality is one or larger at the equatorial tips, and below one at the polar tips. Therefore, by the nature of the failure criterion imposed, failure can only occur at the two equatorial tips. At the polar tips, failure in the experiment occurs by void growth (along the grain boundaries of the oriented grains), but the simulations were not endowed with a capability to mimic this behavior. The final failure seen in this simulation (Figure 2.17d) is quite similar to the pattern observed in Figure 2.7. The constitutive and failure models used in the present simulation are extremely idealized; nevertheless, the simulation has all the necessary ingredients to capture the evolution of failure. We note that when traditional damage models such as the Gurson-Needleman-Tvergaard model are used, failure is generated along one of the shear bands, with the remaining material in the necked region left at the strain level attained at the onset of the shear band. In contrast, the present simulation, with a strain-to-failure criterion shown in Figure 2.12, replicates the final failure pattern quite well and points to the importance of two aspects of the failure criterion: the use of local strain measurements and the inhibition of failure by shear.

2.5. SUMMARY

Ductile failure in oxygen-free high-conductivity copper has been examined through uniaxial tension experiments. In order to follow the deformation of the material, multiple tests were performed and interrupted at different stages of overall deformation; these specimens were sectioned, polished and etched to reveal the evolution of strain at

different positions in the specimen. The evolution of grain-level deformation was quantified by measuring local strain variations. As is typical of such ductile materials, plastic deformation under uniaxial tension localizes into a neck; this is followed by shear localization across the thickness section, with the formation of shear bands oriented at an angle of 45° to the axis of tension. At the central region, where the shear bands intersect and the triaxiality is about unity, a rectangular prismatic cavity was formed. With continued straining, the rectangular cavity expanded in a self-similar manner. Scanning electron micrographs of the fracture surface indicated the absence of void growth and cleavage, suggesting alternating slip as the only mechanism for expansion of the rectangular cavity. Surface texture development was also observed in these specimens; microscopic examination of the grain level strain evolution indicated that new surfaces were generated by the alternating slip mechanism. Simple numerical simulations are used to capture the observed deformation and failure mechanisms.

There are some very important conclusions that are derived from this work, some that are specific to the material considered, and others of more general applicability. First, large strain levels were observed, with local logarithmic strain values lying in the range of 2.5 to 3.5 in regions with different triaxiality. These measurements were performed at the length scale of the grains and are significantly higher than the strain-to-failure obtained from strain measurements based on characteristic specimen dimensions. The general conclusion is that when applying strain-to-failure criteria such as the Johnson-Cook in the element deletion models, one should not rely on measurements of failure strains that are averaged over characteristic specimen dimensions, but obtain local strain measures. Secondly, no evidence of damage in the form of distributed void nucleation was found even in the descending portion of the force-elongation response; therefore this response is attributable to plastic behavior of the material and structural localization and

not damage. Of course, at this stage, this is a material-specific conclusion; detailed examination of each material is necessary to determine if this conclusion is applicable in each case. These results point to the need to exercise caution in applying strain-to-failure and damage models to problems of ductile failure.

Table 2.1. Grain size statistics in the OFHC Copper.

Plane	Mean – μm		Standard Deviation – μm	
	Major axis	Minor axis	Major axis	Minor axis
y-z	62	27	27.7	13.1
x-y	90	42	32.9	19.0
x-z	80	26	33.7	13.5

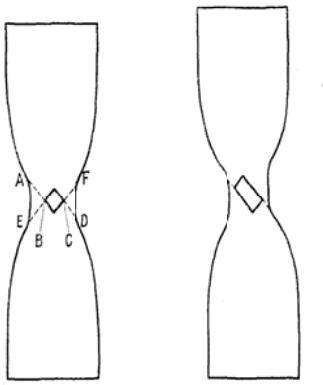

Figure 2.1. Sketch of the alternating slip mechanism of cavity growth (reproduced from Orowan 1948).

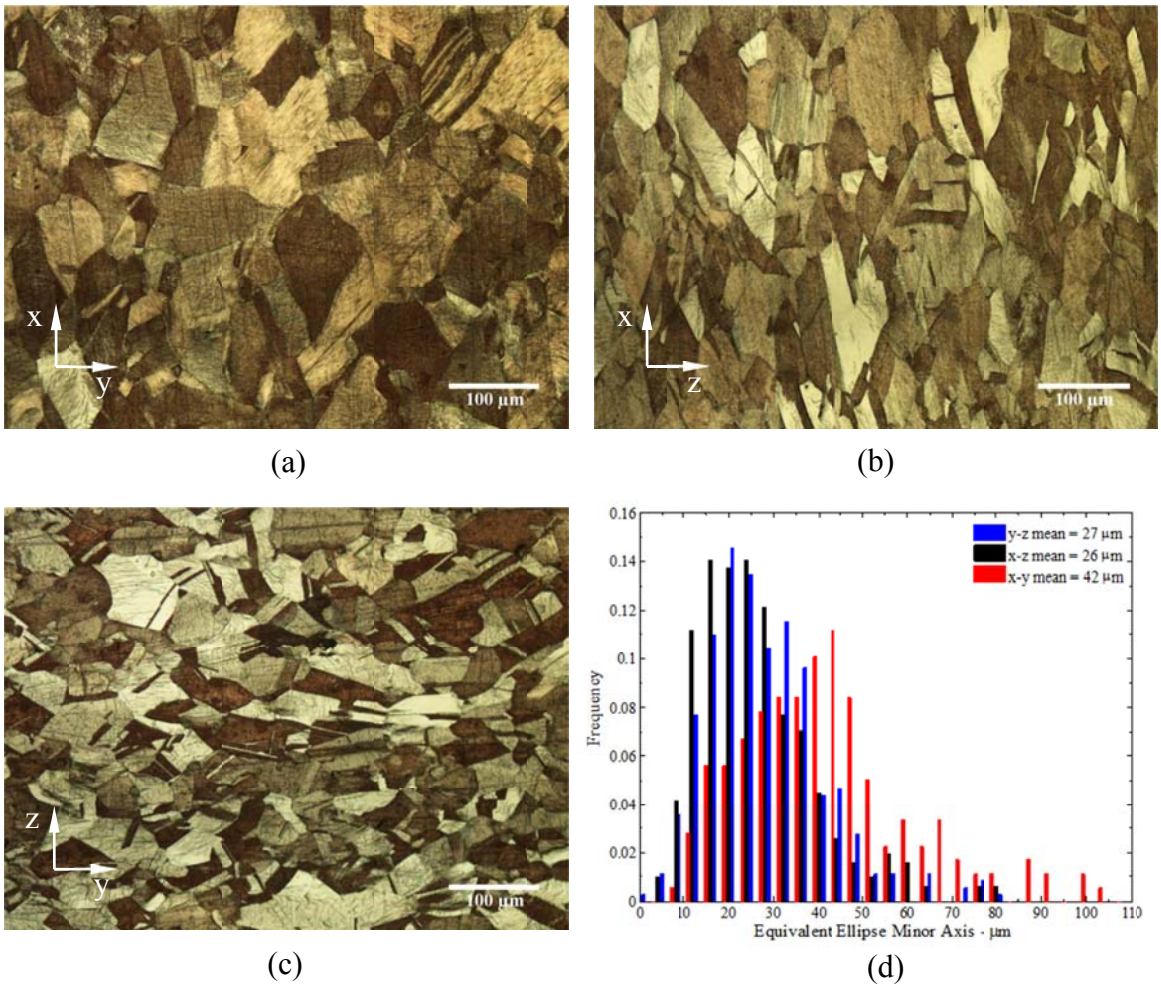

Figure 2.2. Microstructure of OFHC copper in the (a) x-y. (b) x-z, and (c) y-z planes. The (x,y,z) directions are the rolling, transverse and thickness directions, respectively. The distribution of equivalent ellipse minor axis in the three directions is shown in (d).

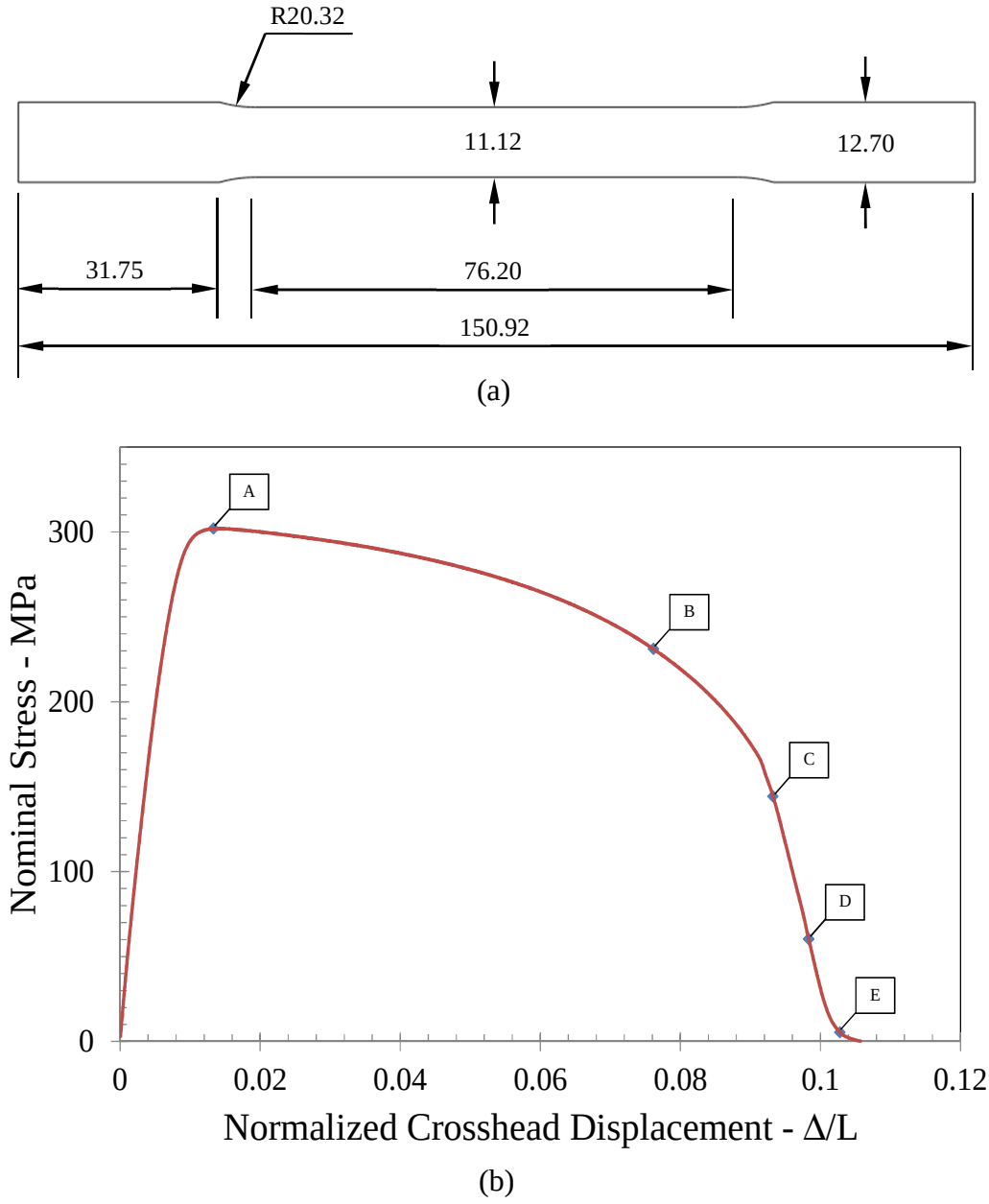

Figure 2.3. (a) Diagram of the rectangular cross-section specimen; all dimensions are in mm. The thickness of the specimen is 6.46 mm. (b) Variation of the nominal stress vs. crosshead displacement, Δ, normalized by the gage length, L, for OFHC copper specimen. Point A corresponds to the peak load; four different specimens were tested and unloaded from the points B, C, D and E. These specimens were used for microstructural examination.

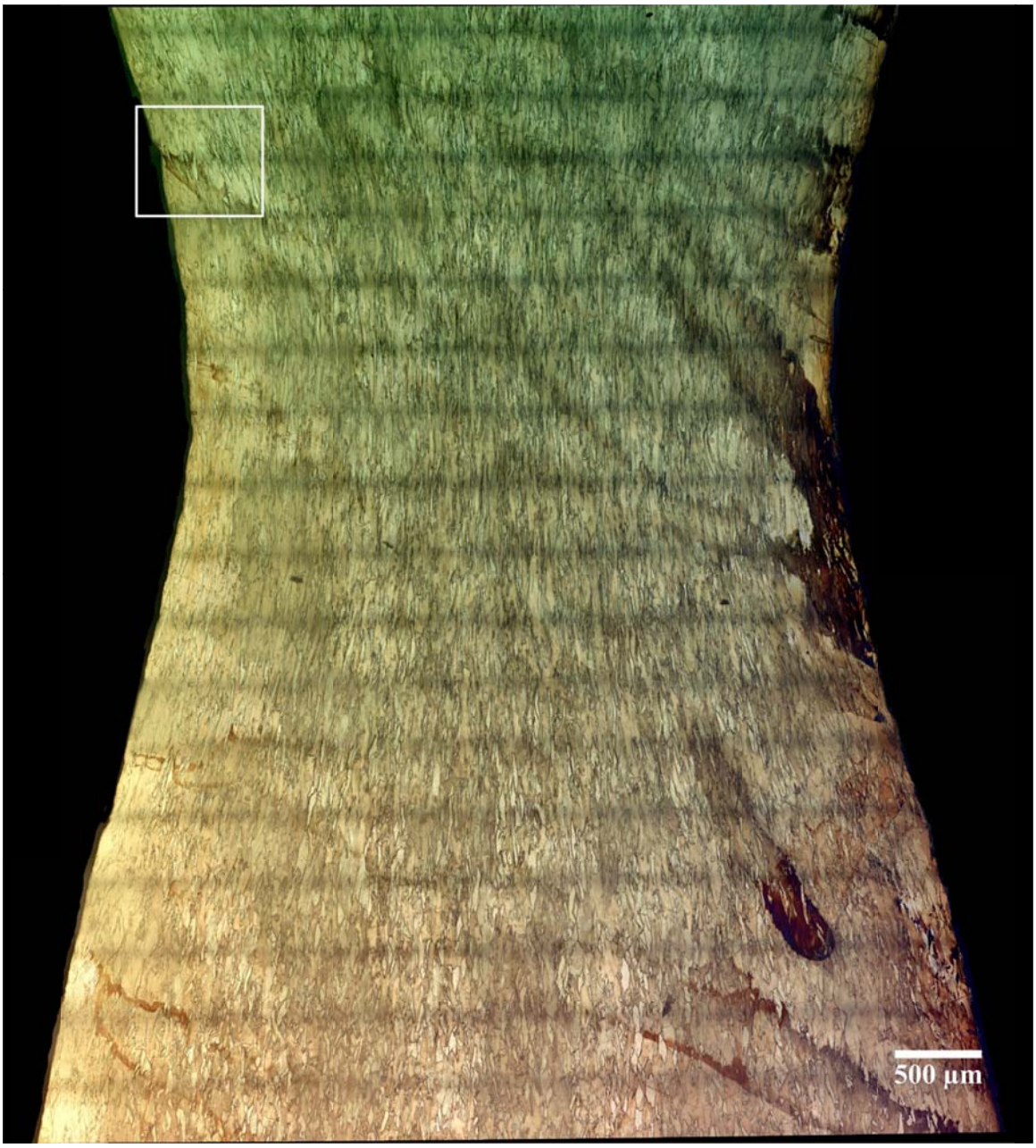

Figure 2.4. Micrograph showing an x-z section of Specimen B. The grain flow is revealed by etching with copper etchant #1. The region inside the white box is shown in high magnification in Figure 2.15a. See Supplemental Files Section for a high resolution image of this figure.

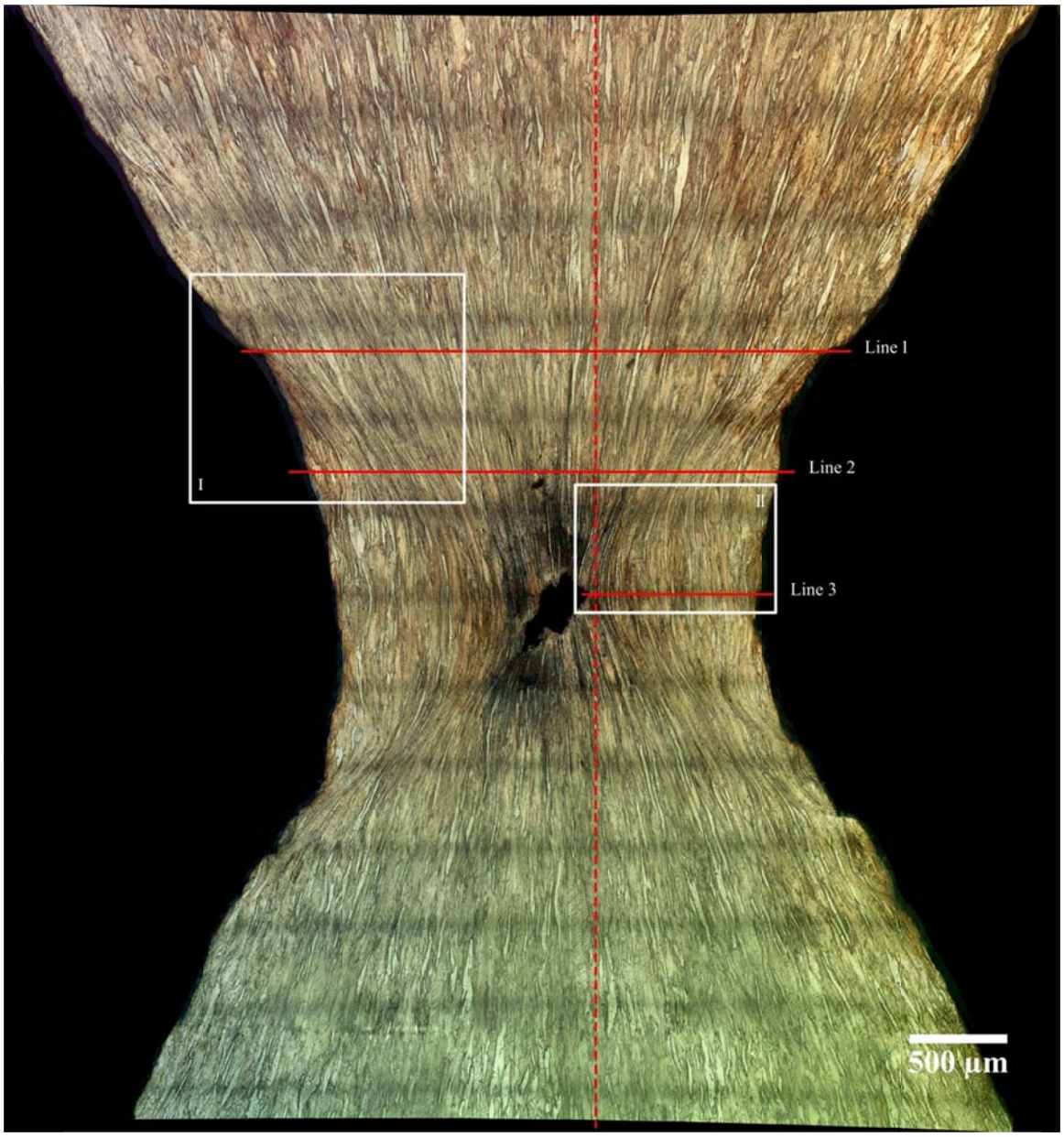

Figure 2.5a. Micrograph showing an x-z section of Specimen C. The grain flow is revealed by etching with copper etchant #1. The regions I and II inside the white boxes are shown in high magnification in Figures 15b and 9 respectively. In addition to the necked profile, it is possible to identify shear strain localization across the specimen in two bands oriented roughly at 45° to the tensile axis. Furthermore, a rectangular cavity can be seen at the center of the specimen. The x-y section view along the dashed red line is shown in Figure 2.5b; grain measurements were performed.

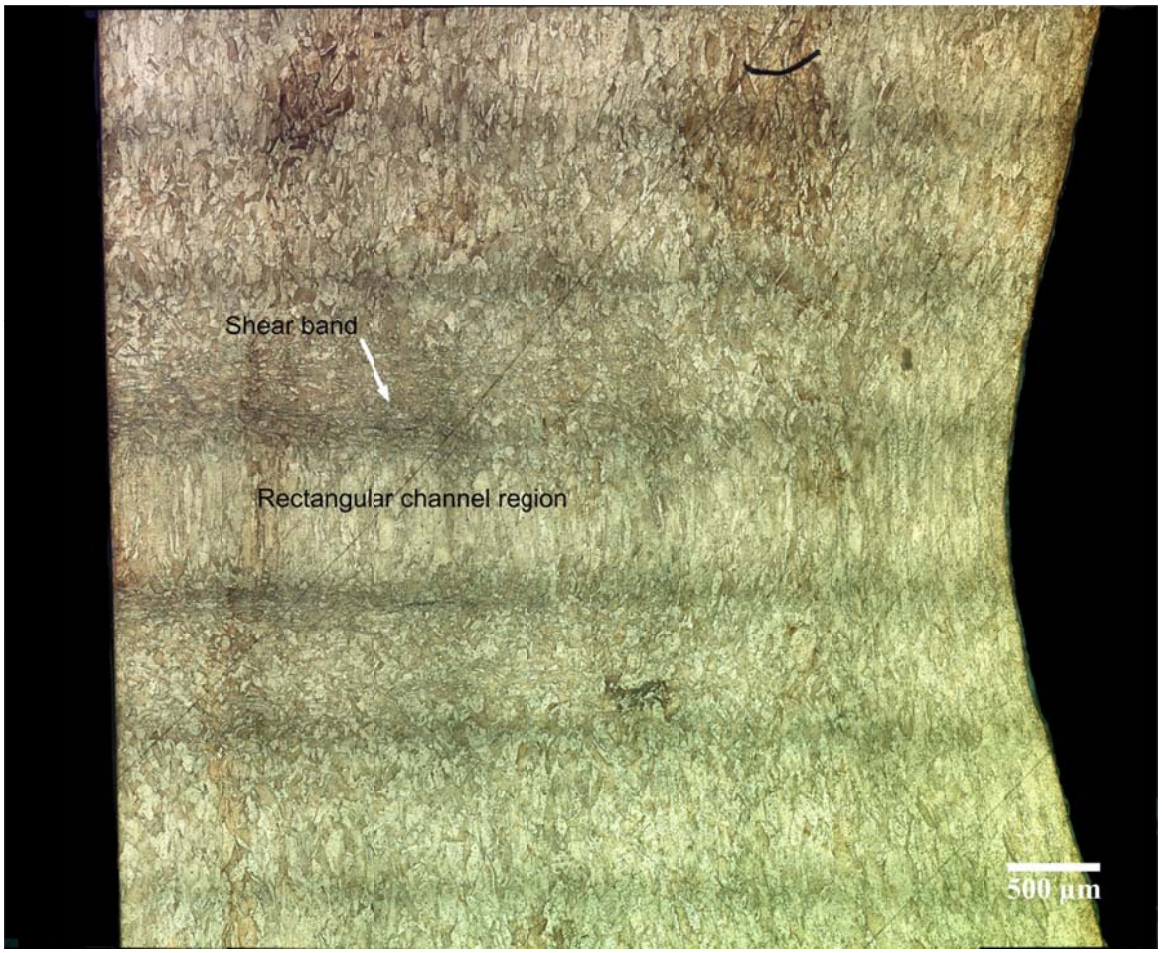

Figure 2.5b. Micrograph showing an x-y section of Specimen C; this section is taken along the dashed red line in Figure 2.5a. The grain dimensions are revealed by etching with copper etchant #1. The fact that the grains are elongated and that the grains are rotated in the shear band can be observed easily; also the prismatic nature of the channel can be inferred from this section.

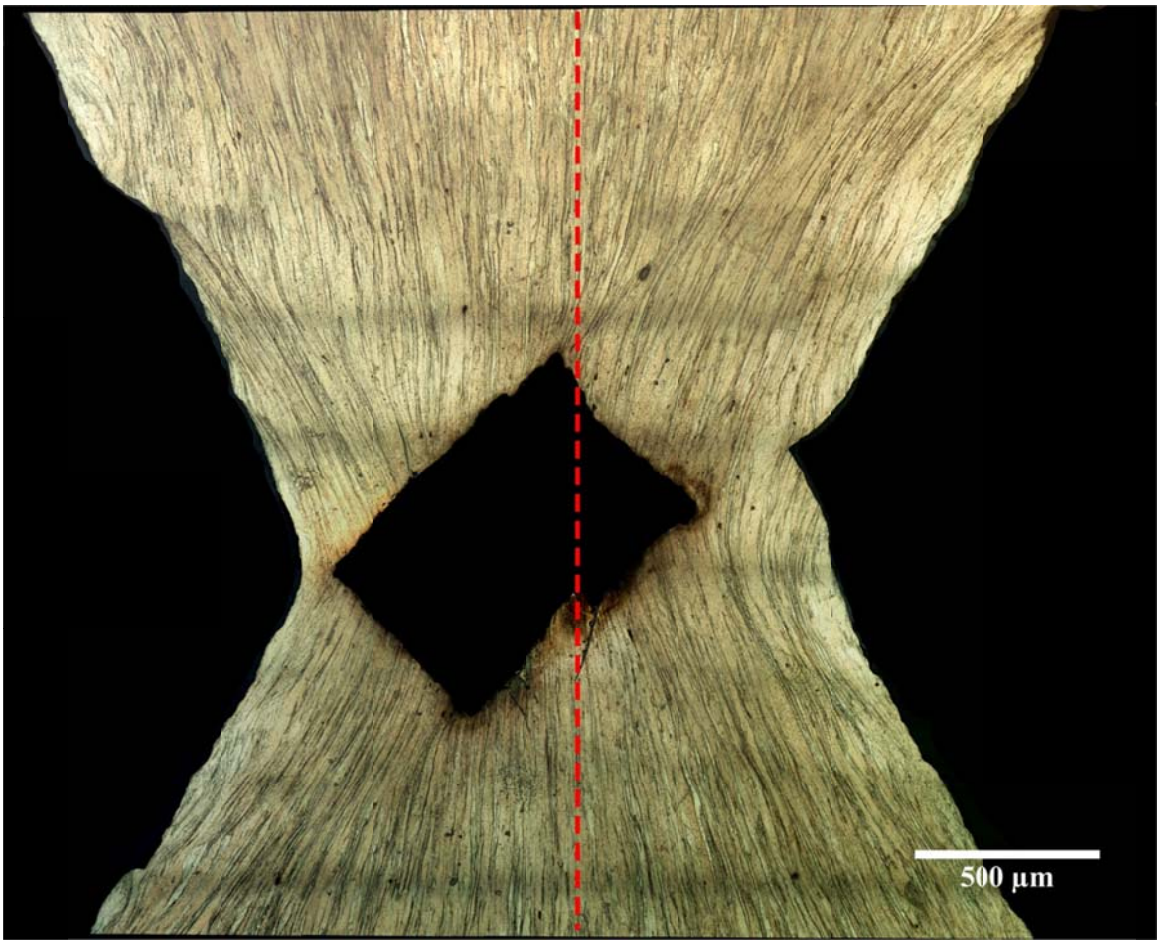

Figure 2.6a. Micrograph showing an x-z section of Specimen D. The grain elongation is revealed by etching with copper etchant #1. The x-y section view along the dashed red line is shown in Figure 2.6b. The rectangular cavity maintains its symmetry and enlarges. Other shear localized zones are also visible at the free surfaces of the specimen. See Supplemental Files Section for a high resolution image of this figure.

Figure 2.6b. Micrograph showing an x-y section of Specimen D; this section is taken along the dashed red line in Figure 2.6a. The prismatic nature of the channel can be readily seen from this section.

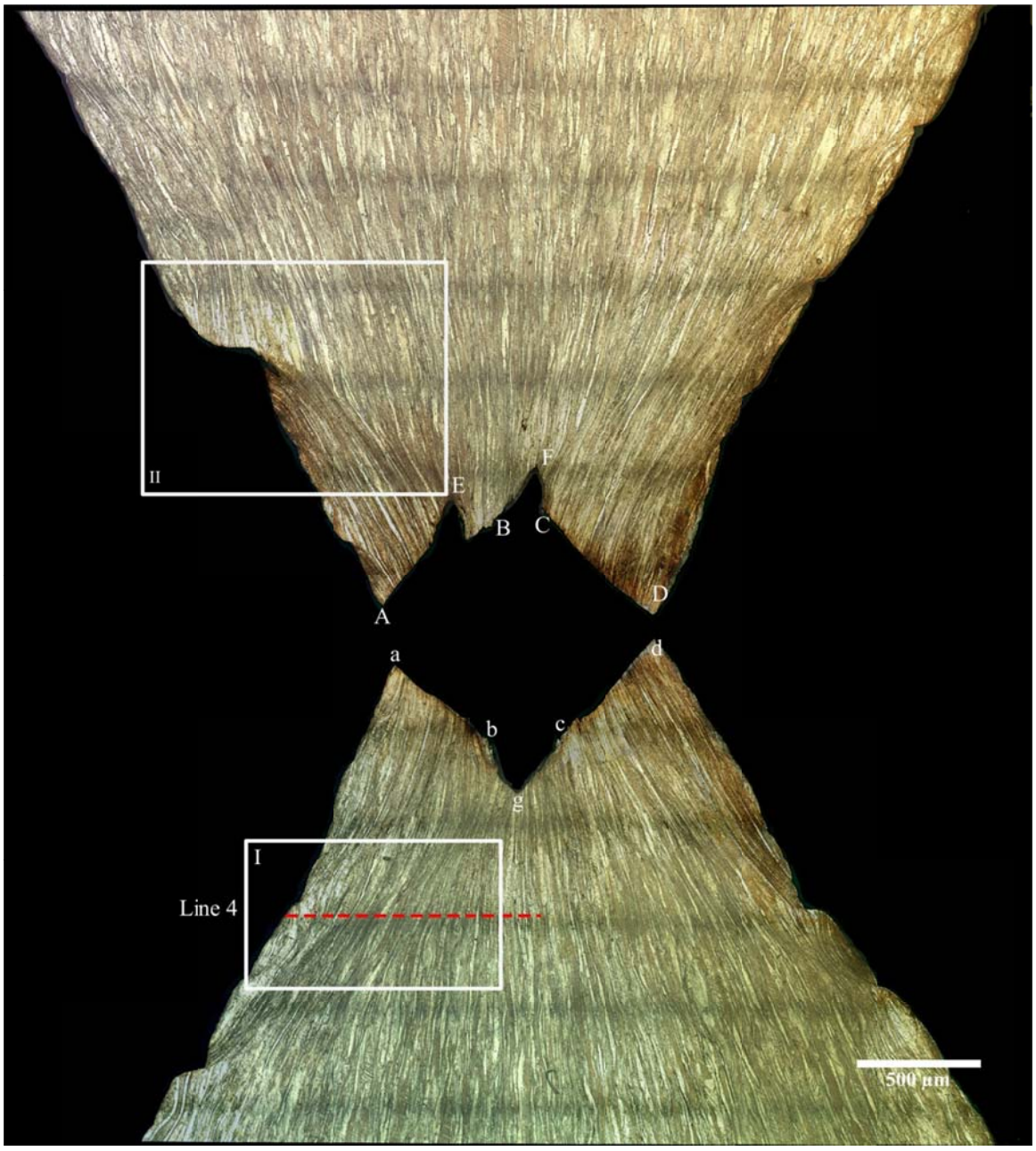

Figure 2.7. Micrograph showing an x-z section of Specimen E. The rectangular cavity continues to maintain its symmetry until complete failure of the cross-section. Material points corresponding to the upper and lower fracture surfaces are identified by upper and lower case letters. The regions I and II inside the white boxes are shown in high magnification in Figures 2.8 and 2.15c, respectively. See Supplemental Files Section for a high resolution image of this figure.

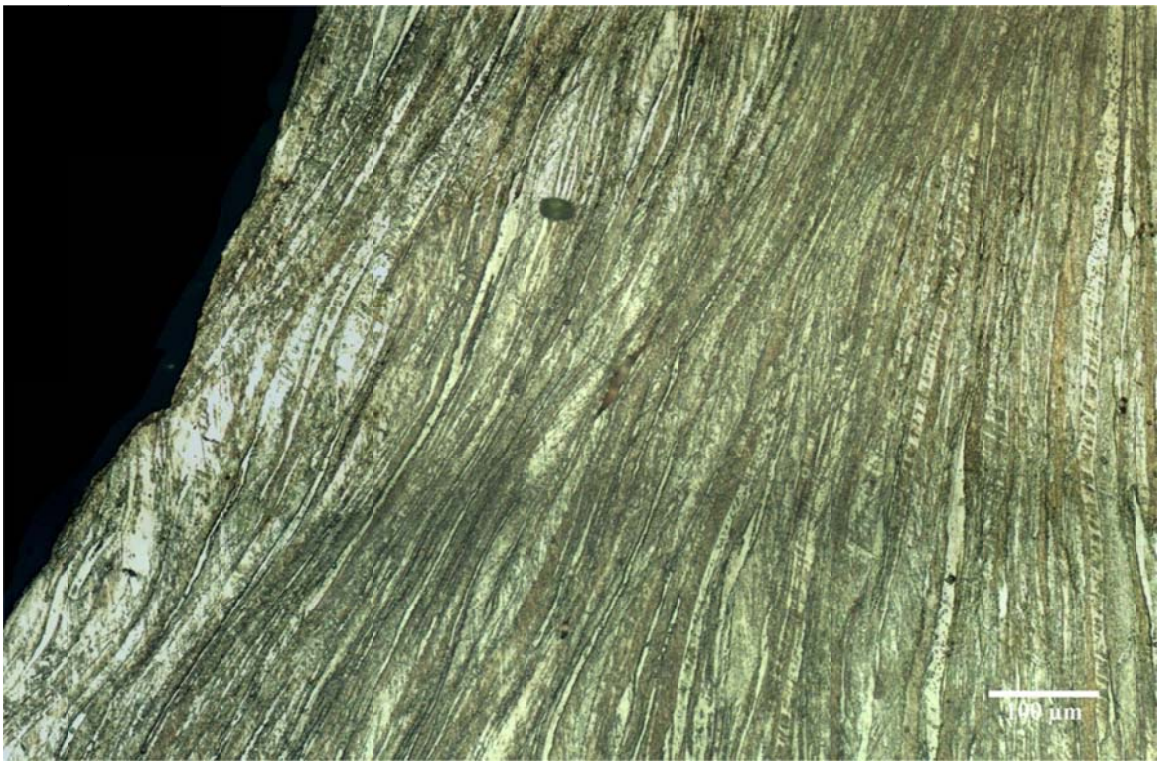

Figure 2.8. High magnification image of Region I in Figure 2.7.

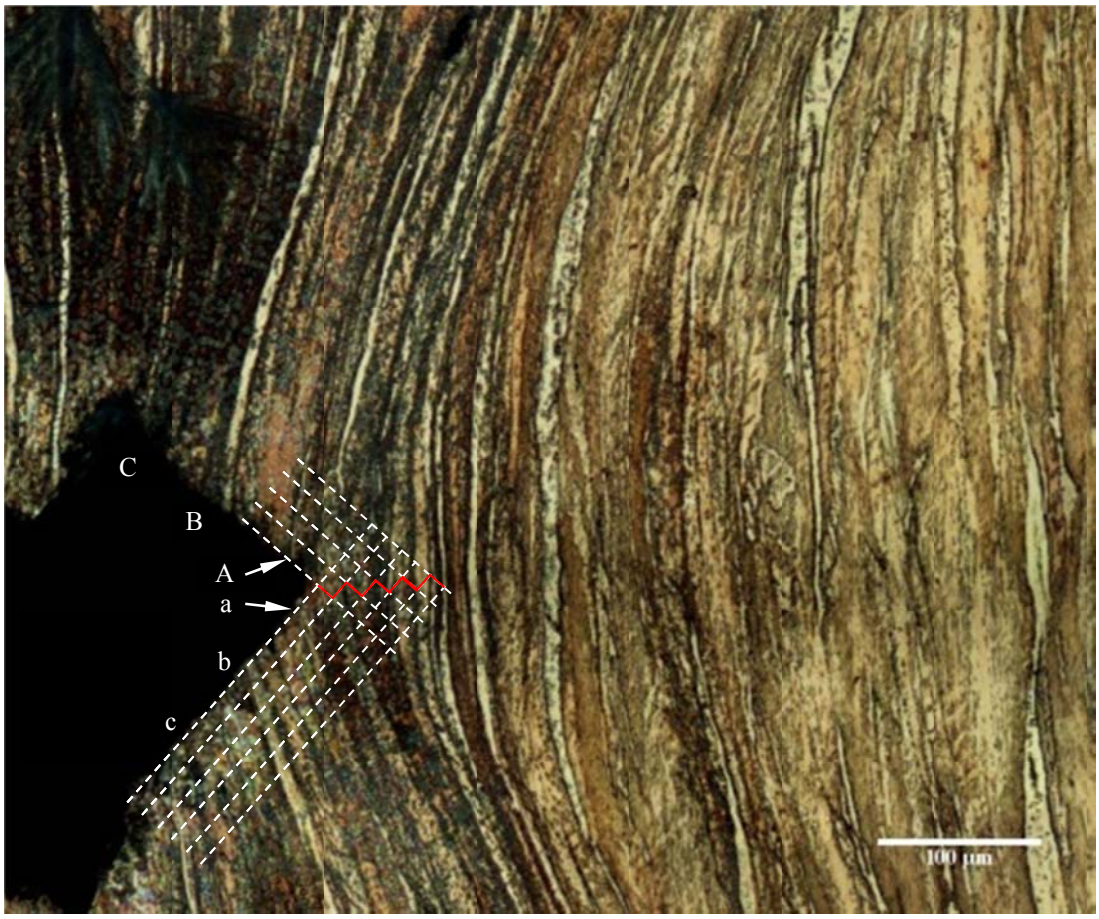

Figure 2.9. Detailed image of the Region II in Figure 2.5a, showing the tip of the rectangular cavity. The corresponding grains on the upper and lower fracture surfaces are shown by the upper and lower case letters, respectively. The alternating slip mechanism of crack extension is sketched by the red line; the expansion of the rectangular cavity is indicated by the white dashed lines.

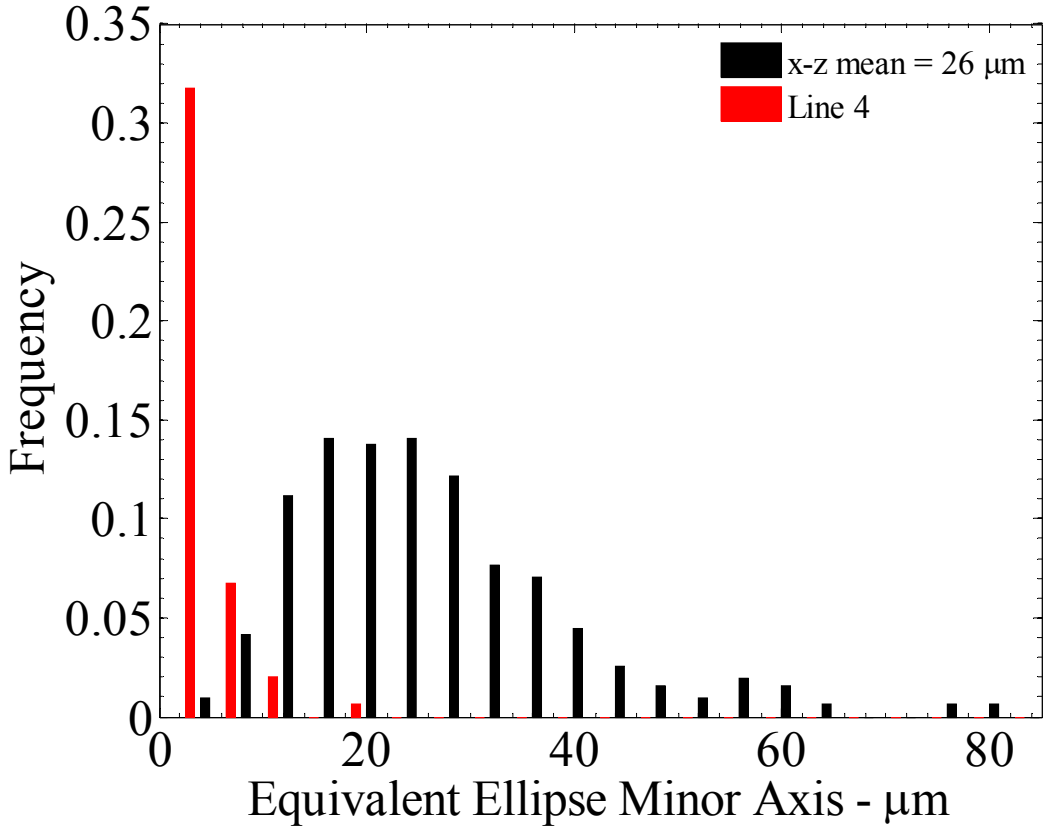

Figure 2.10. Histogram of grain size in the x-z direction of the unstrained material is compared with the histogram of grain sizes measured along Line 4 of Figure 2.7, including the shear localized region.

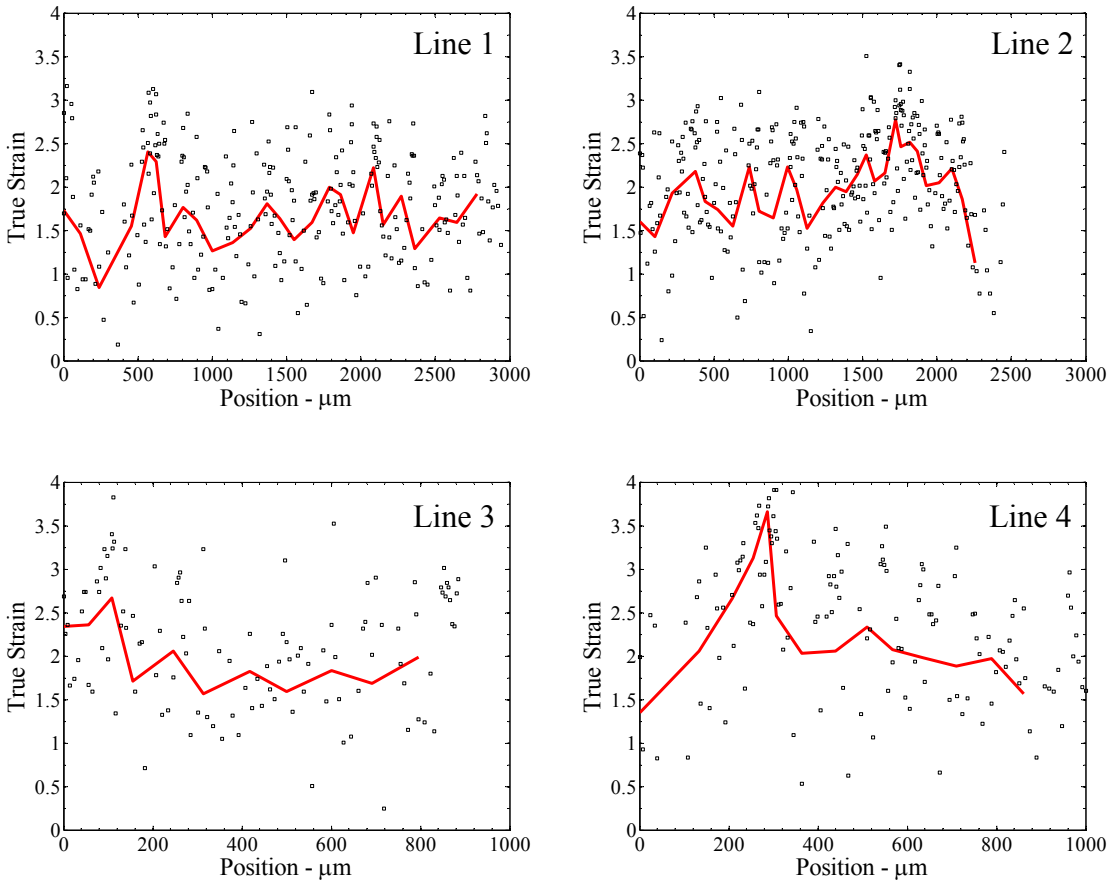

Figure 2.11. Spatial variation of the equivalent plastic strain along Lines 1–3 of Figure 2.5a and Line 4 of Figure 2.7. The open symbols indicate the strain estimate based on each grain while the red line is a strain estimate averaged over every ten grains.

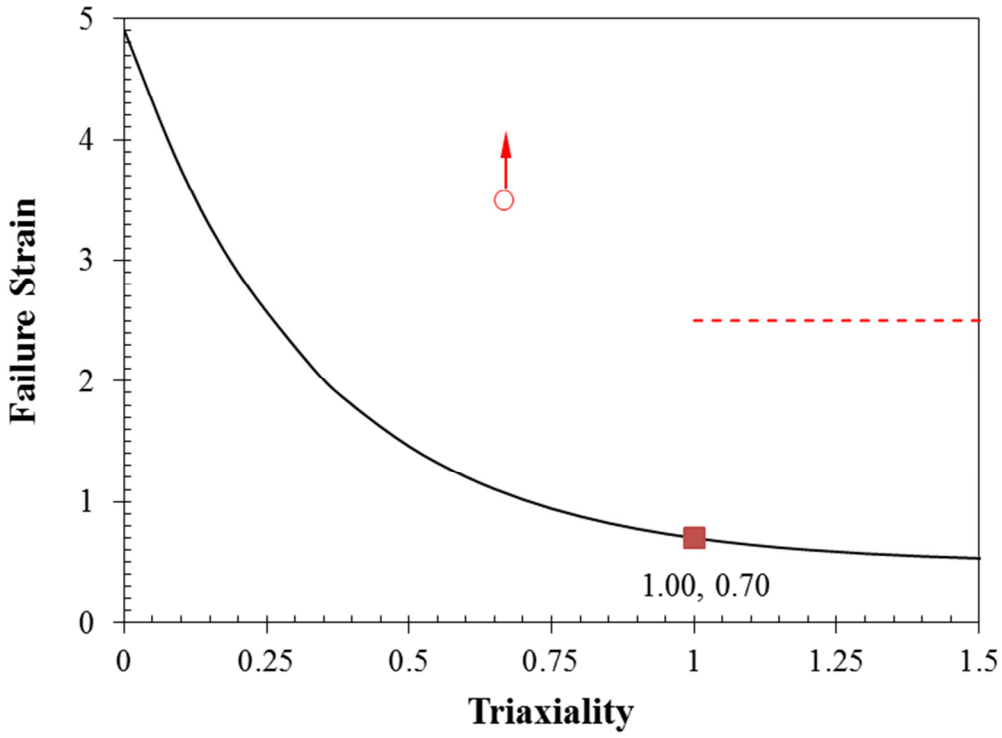

Figure 2.12. Johnson-Cook failure criterion for OFHC copper (with parameters from Johnson and Cook 1985). The red dashed line indicates that failure was observed at a strain level of ~2.5 near the notch tip with a triaxiality in the range of one to three. The red open circle indicates that a strain of about 3.5 was measured in the region of the shear band, where the triaxiality is ~0.667; however, since these points did not exhibit damage/failure, we mark an arrow to suggest that the failure strain should be higher than 3.5.

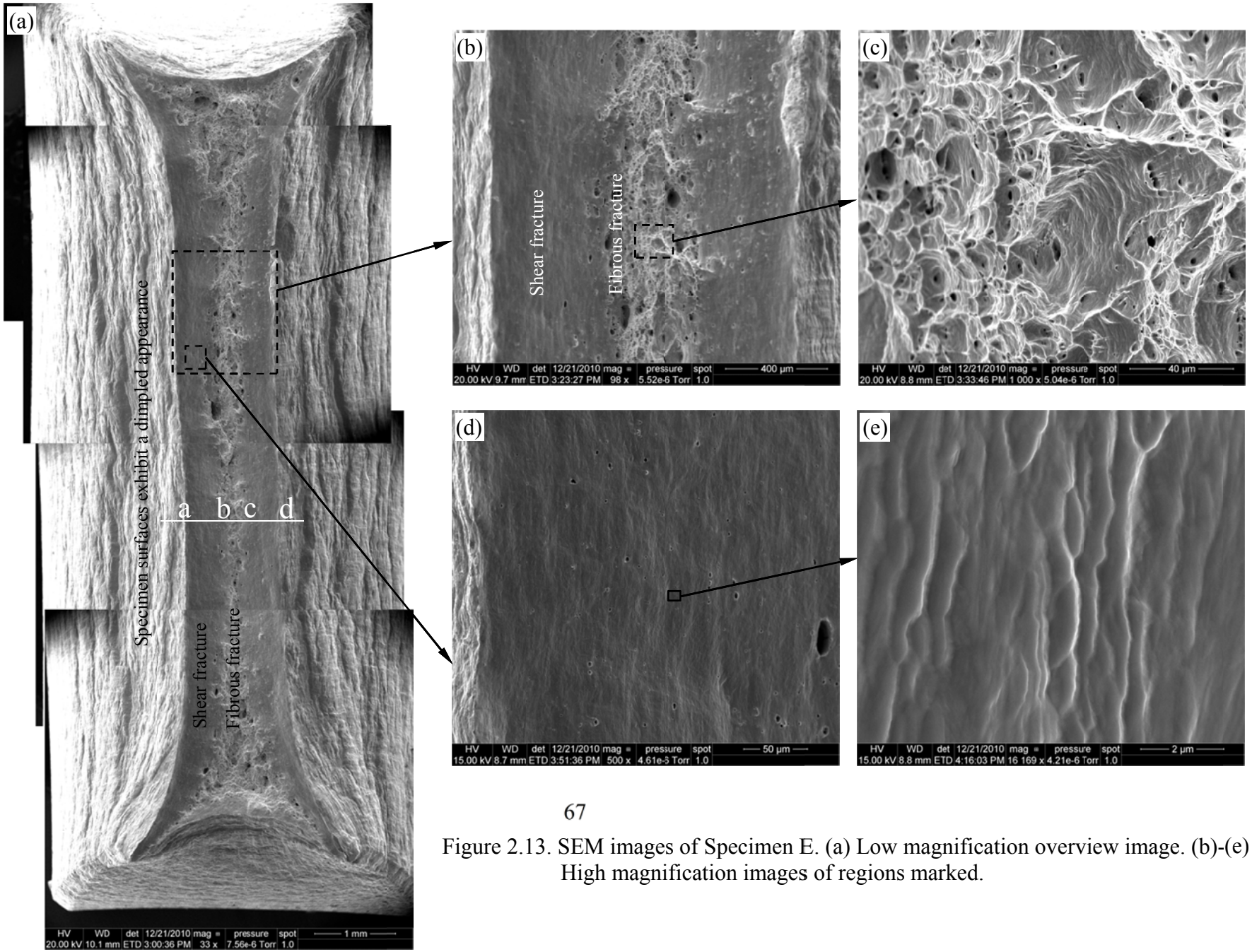

Figure 2.13. SEM images of Specimen E. (a) Low magnification overview image. (b)-(e) High magnification images of regions marked.

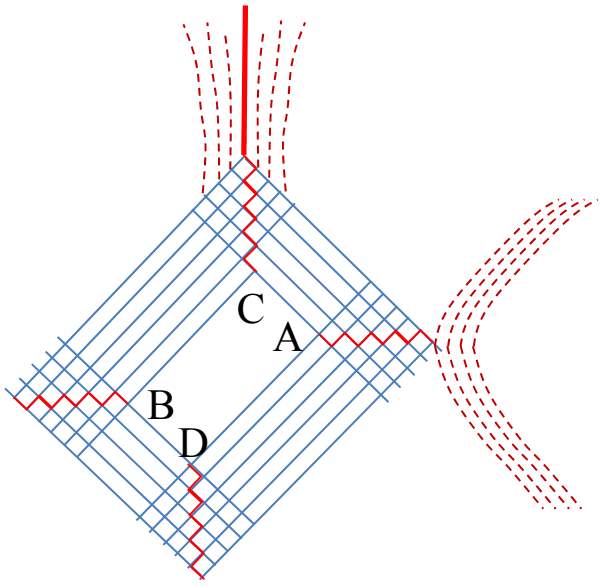

Figure 2.14. Sketch illustrating grain orientation (in dashed red lines) near the four corners of the rectangular cavity. The blue lines indicate sequential opening of the rectangular cavity by alternating slip along the solid red lines. At the two corners labeled A and B, the grains are oriented in the direction of tension and the crack extends by alternating slip; at the other two corners, the grain are perpendicular to the line of tension and a void growth mechanism seems to be triggered at some point.

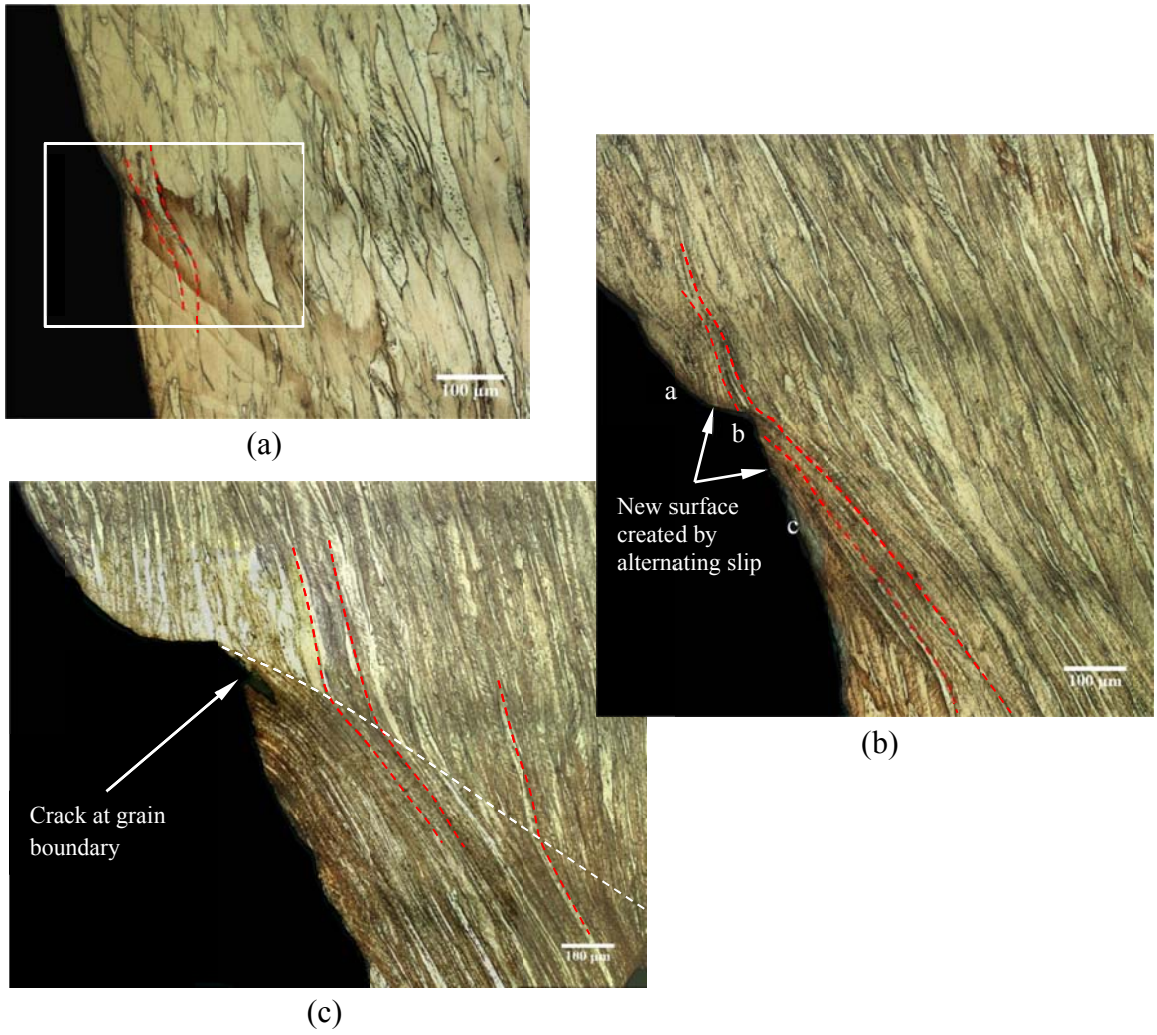

Figure 2.15. Detailed images of the regions outlined by the white rectangles in Figures 2.4, 2.5a and 2.7, showing the shear localization near the surface of the specimen. Streamlines are traced by the dashed red lines. The creation of new surfaces by the alternating slip mechanism is identified. See Supplemental Files Section for high resolution images.

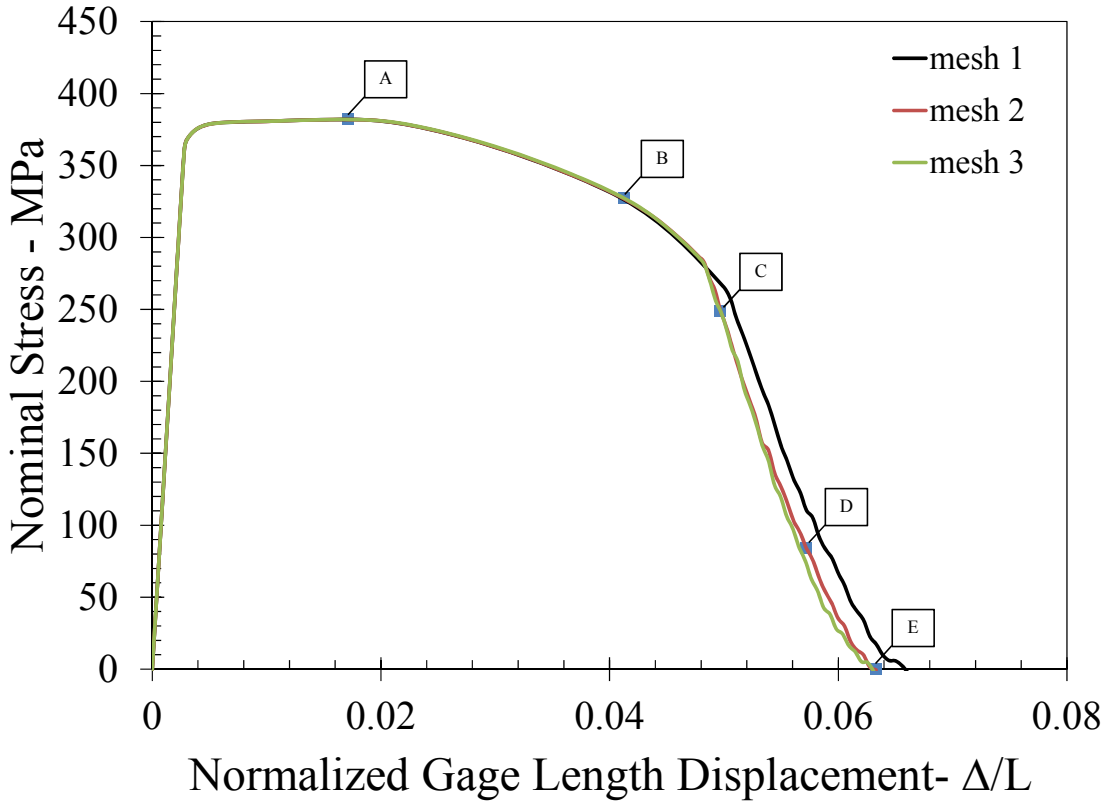

Figure 2.16. Nominal stress vs. gage displacement response from three mesh densities, mesh 1, mesh 2 and mesh 3. Labels A-E mark the peak load, diffuse necking, shear localization and rectangular cavity formation, growth of the rectangular cavity, and final separation.

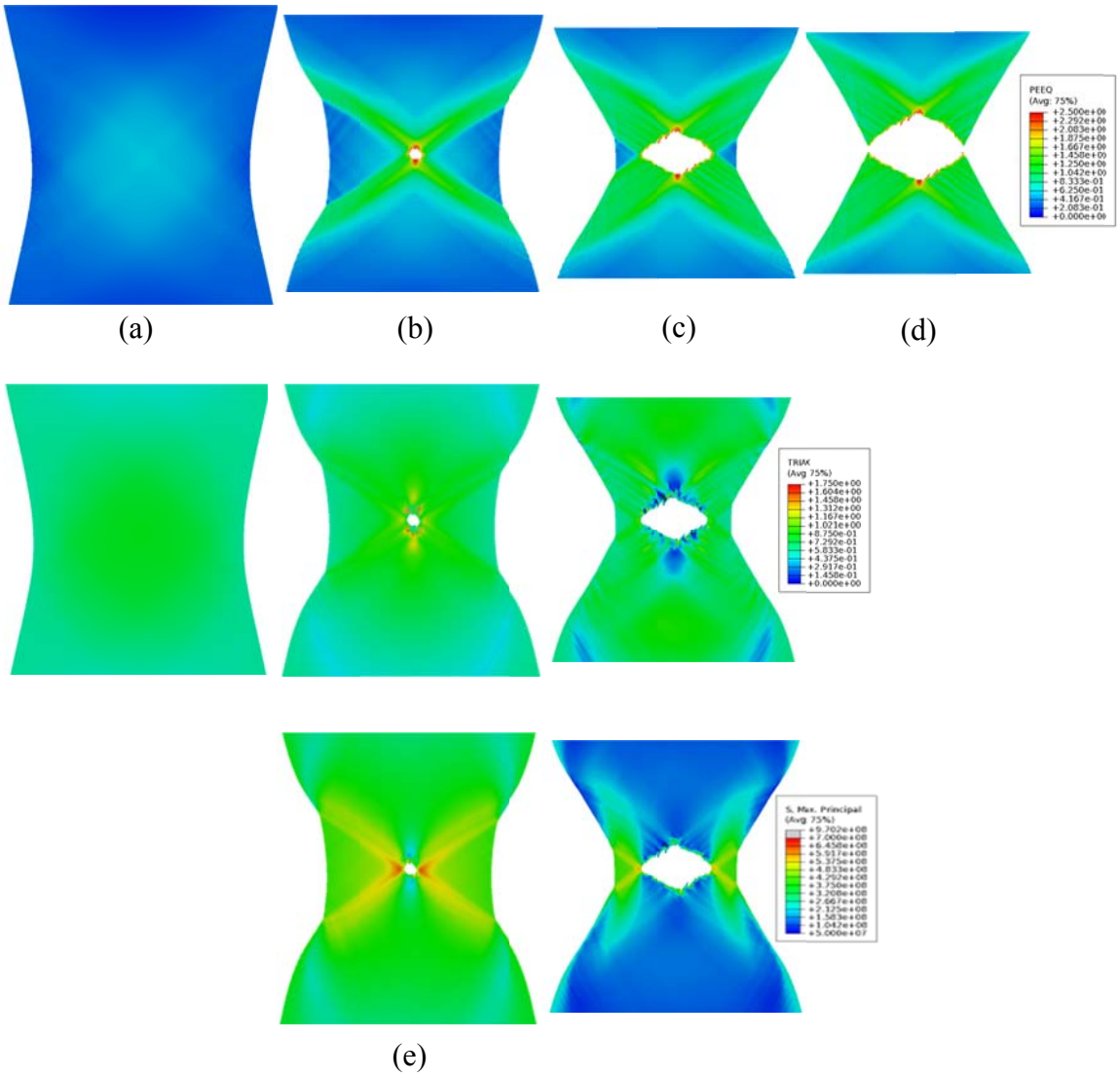

Figure 2.17. Results of the plane-strain finite element simulation incorporating isotropic J_2 plasticity and element deletion failure model. The equivalent plastic strain, triaxiality and maximum principal stress at different stages in the loading are shown. The four stages shown here correspond to points B, C, D and E indicated in Figure 2.16.

Chapter 3: Constitutive and Failure Behavior of Polycrystalline Al 6061-T6

In this section, the results of an investigation into the elastic-plastic response of Al 6061-T6 and the development of damage leading up to the point of final failure are reported. Macroscopic as well as microscopic responses are investigated in order to facilitate model building. Uniaxial tests and notched tension tests were used in order to vary the degree of triaxiality significantly. Pure shear tests and shear tests with superposed tension or compression have also been performed and these results will be discussed in the next Chapter.

3.1. MATERIAL

Attention is focused in this section on specimens of Al 6061-T6. The chemical composition of the aluminum alloy is listed in Table 3.1. In order to reveal the grains, sections of the specimen were prepared using standard metallographic polishing techniques. The specimens were mounted in epoxy and wet-polished starting from 320-grit size and going down to 1200-grit size sand paper. Special care was taken not to apply excessive force on the specimens so as to prevent the polishing compound from embedding into soft aluminum matrix. In the next stage, an abrasive diamond paste with particle diameter 3 μm and 1 μm was used with a lapping cloth, and finally a colloidal suspension with 0.05 μm diameter silica particles was used to achieve the required metallographic finish. The specimens were then pre-etched, first in 2% aqueous solution of sodium hydroxide for 55 seconds, and subsequently color-etched with Weck's (Weck and Leistner 1986) alkaline solution (4% potassium permanganate + 1% sodium hydroxide) for 15 seconds to obtain the contrast in the microstructure. This polishing and

etching process allows good visibility of the grain boundaries. We note that in nearly all papers published in the literature on Al 6061-T6, such etching process has not been used. Hence, microstructural features could not be revealed at the grain level prior to the work presented here. About 40 to 50 images of each section were taken in a Nikon Eclipse optical microscope at magnification of 200X in order to quantify the initial grain size distribution in the material. The initial microstructure of the Al 6061-T6 in three sections x-y, x-z and y-z is shown in Figures 3.1a-c. As indicated earlier, the x,y,z directions correspond to the rolling, transverse and thickness directions respectively. The grain dimensions in y and z directions are calculated for each section as the distance between two intersecting points of a grain with the lines parallel to y and z directions. The distributions of the grain dimensions on the three sections are plotted in Figure 3.1d. It is evident from distributions of the grain size that the grains are nearly equiaxed in the rolling plane (x-y plane) with the mean size of 39 μm. The average grain size in the z-direction is about 14 μm. This grain size distribution suggests planar isotropy in the microstructure; it should be noted that this anisotropy is topographical and does not account for the crystallographic orientation, if any, of different grains. In addition to the grains, the optical micrographs also reveal the distribution of second phase particles; one such particle is identified in Figure 3.1b. The composition of these particles was identified through EDS in a scanning electron microscope to be composed primarily of iron; these particles are added in the solidification process. Quantitative estimates of the amount of second phase particles were obtained by thresholding and image analysis methods in NIH ImageJ software. The average size of equivalent ellipses is in the range of 1 to 5 μm; the average volume fraction of the particles was found to be 0.012 and the particle spacing was calculated to be about 25 μm.

3.2. EXPERIMENTS

3.2.1. Uniaxial Tension Test

Uniaxial tension tests were performed on standard dog-bone type specimens in order to characterize the elastic-plastic behavior of the materials. The geometry of the specimens used in the experiments is shown in Figure 3.2. Specimens corresponding to the test geometry were cut by electric discharge machining (EDM) from 2.44 mm thick rolled sheets of Al 6061-T6. These tests were run on an Instron 4482 universal testing machine at a crosshead speed of 0.254 mm/min, resulting in quasi-static loading at a strain rate of 1.18E-04 s^{-1}. The gage displacement was measured using a variation of the digital image correlation technique called Q4-DIC (Besnard et al. 2006). In this method the region of interest is discretized in the same way as in the finite element method and similar continuous shape functions are used to interpolate the displacement within the element. The pattern matching between subsequent images is based on the conservation of optical flow; then the error functional is minimized using the shape functions thereby leading to a set of linear equations that are solved using the Newton-Raphson method. In contrast to the traditional DIC (Sutton et al. 1983), the continuity of displacement field is enforced in this version of the DIC. One key advantage of this method is that by having the same discretization scheme for the measurements and the numerical simulations, the error stemming from intermediate projection steps are reduced (Réthoré et al. 2007). Furthermore, the accuracy of the traditional image correlation technique degrades where there is a strong gradient or discontinuity in the displacement field such as in the vicinity of strain localization and cracks. This issue can be mitigated in the Q4-DIC approach where the kinematics can be enriched with discontinuous and singular functions, as in extended finite element method, to account for these types of irregularities in the full field analysis (Réthoré et al. 2007). This method was implemented in MATLAB and was

used to analyze the displacement and strain fields in experiments. More details on the implementation of this technique can be found in the Appendix A. The surface of the specimens was spray painted to form a random speckle pattern; the speckle size, pattern, contrast, illumination, and the resolution are among the factors that affect the quality of the displacement calculation in digital image correlation. In order to obtain optimum results several different combinations were examined and the best speckle pattern for each specimen was applied to the surface of the specimen in the region of interest. It has been shown that a white background paint with a fine black speckle gives the best results. A CCD camera was used to take digital images of the specimen throughout the test at different stages of the loading. The strain in the specimen was estimated as the average over a gage length of 25.4 mm in the uniaxial tension specimens. Load data were acquired as a function of time and crosshead displacement using the load cell on the Instron testing machine. The two measurements were then correlated to obtain the stress vs. strain variation in the specimen. The nominal stress (force/initial cross-sectional area) vs. normalized gage displacement is plotted in Figure 3.3 for the Al 6061-T6; in an effort to characterize the anisotropy, specimens cut at 0º, 45º and 90º to the rolling direction were considered. Uniform deformation in the gage section is terminated at the Considère point (the point of peak load in Figure 3.3); for the material considered here, this occurs at $\varepsilon_n = 0.08$.

The true stress vs. true strain response of Al 6061-T6 up to the necking can be represented by a power law as follows (in MPa)

$$\sigma = 322\left(1 + \varepsilon / 0.0419\right)^{0.141} \tag{3.1}$$

It is clear that the stress-strain curve can only be obtained up to onset of localization from these dogbone tensile specimens; extrapolating the curve to larger strains by curve fitting is fraught with inaccuracies that cannot be estimated. In order to extend the characterization of material response beyond the point of localization, a few methods, such as the Bridgman correction factor (Bridgman 1964) and compression or torsion tests, have been suggested in the literature. Here, we choose an inverse method to calibrate the stress-strain behavior, where the measured response in other loading configurations is compared to predictions from a finite element simulation.

The sheets of aluminum used in these experiments are expected to exhibit anisotropy resulting from the rolling process used in their manufacture. The measured nominal stress vs. normalized gage displacement curves from uniaxial tension tests performed on dogbone tensile specimens cut in the direction at 0º, 45º and 90º to the rolling direction are shown in Figure 3.3; these curves for different orientations are very close to each other, implying that the planar isotropy maybe assumed. However, the local strains have to be compared in all directions as well in order to verify planar isotropy and characterize the extent of anisotropy. In the tests reported here, the axial and transverse strains $d\varepsilon_\alpha$ and $d\varepsilon_{\alpha+\pi/2}$ were measured for each orientation α using DIC. Therefore, the ratio of the width to thickness strain increment, which is referred to as Lankford's r-value, defined as follows:

$$r_\alpha = \frac{d\varepsilon_{\alpha+\pi/2}}{d\varepsilon_z} \tag{3.2}$$

where $d\varepsilon_\alpha$ and $d\varepsilon_z$ are the strain in direction at an angle α from the rolling direction and in thickness direction, respectively, can be measured from each test. The volumetric strain is assumed to be zero so that the increment of strain in thickness direction can be

easily calculated as $d\varepsilon_z = -\left(d\varepsilon_x + d\varepsilon_y\right)$. The measured r-values for the Al 6061-T6 are given in Table 3.2. It was observed from strain measurements that the ratio $d\varepsilon_y / d\varepsilon_x$ before the onset of necking remains relatively constant suggesting that the anisotropy does not appear to evolve during uniaxial loading in this material. However, a detailed grain-based analysis is required to verify this. It turns out that this anisotropy of the rolled sheets is very important in capturing the true response of the Al 6061-T6 specimens in other loading conditions, such as the notched-tension test.

3.2.2. Notched-Tension Tests

Although the uniaxial tension test is perhaps the simplest and most commonly used test for material characterization, the onset of localized deformation at very low strain levels makes it ill-suited for constitutive and failure characterization; specifically, one cannot determine the stress-strain variation beyond the Considère point. Furthermore, eventual failure occurs within the localized region where strain evolves to much larger levels in a more complex stress state. In order to push the evaluation of the stress-strain diagram to larger strain levels and *to explore the failure behavior under different triaxiality conditions*, we performed tension tests on symmetrically notched flat specimens. It was estimated that the initial value of triaxiality (the ratio of the mean stress to the equivalent stress, σ_m / σ_{eq}), could be increased to about 0.577 in this configuration. The geometry of the specimen is depicted in Figure 3.4a. Two notches of radius 4.06 mm were introduced in 25.40 mm wide strips cut from the aluminum sheet in the direction parallel to the rolling direction. One advantage of this geometry is that it enables reaching significantly larger strain levels, but at the penalty of a nonuniform strain field; therefore, it is essential that local strain fields be monitored using DIC. Another advantage is that it

could decouple strain localization triggered by plastic instabilities from damage processes that result in material separation so that attention may be focused on the latter.

In order to study the onset and growth of damage during deformation under different levels of stress triaxiality and plastic strain, notched tension specimens were loaded in the rolling direction and interrupted at different crosshead displacements. The nominal stress (force/initial minimum cross-sectional area) vs. normalized crosshead displacement curves from five different tests that were interrupted at different displacements are plotted in Figure 3.5. Four other tests under similar conditions were also performed, three to complete failure and one that was unloaded just prior to global failure. The variation in the load at final failure was within 0.9 %; the crosshead displacement at final failure also varied within 1.6 %. This small variation is used as support for considering the specimens that were unloaded just prior to failure as being at the "brink of failure". Specimen A corresponds to unloading from the point of the peak load, Specimen B from a point between the peak load and ultimate failure, Specimens C and D corresponding to just at the brink of failure, and Specimen E corresponding to a fully failed specimen. Contours of the axial and transverse strain as measured with DIC are overlaid on the speckled specimen surface in the images shown in Figure 3.6. These are from Specimen E and correspond to the normalized crosshead displacements of Specimens A, B and C. For specific implementation of DIC used in this work, the displacements are measured at nodes with a spacing of 79.6 μm and strains are determined with a gage length of 159.2 μm. From these results, we note the following:

- The surface strain over much of the specimen is quite small, on the order of 0.02, except in the vicinity of the notch where it increases to values in the range of 0.35 to 0.40. Associated with this, there is significant thinning of the specimen in this

region. Clearly, as expected, the strain ε_x at the notch is significantly higher than that in the middle region of the specimen.

- Near the middle portion of the minimum cross section ($x = 0, y = 0$), the strain $\varepsilon_y \cong 0$, indicating a plane strain state, and thereby an elevated triaxiality at this location.
- With increasing global displacement, the strain contours in Figure 3.6 indicate the emergence of two horizontal bands of elevated strains. For closer observation of this region of large strains, this experiment was repeated with the imaging system tracking the deformation at very high spatial resolution such that only the central 8 mm by 6 mm region of the specimen was observed (see dashed box in Figure 3.4b). Contours of axial strain from this test are shown in Figure 3.7. The variation of the axial strain ε_x along the line x_1-x_2 is shown in Figure 3.8b, corresponding to different values of the gage displacements indicated in Figure 3.6. It is evident that a double humped variation is seen in ε_x along the x direction. The double hump in this figure is a clear indication of the formation of the strain localization across the thickness direction of the specimen. Post-test examination of these specimens indicated that this localization occurred at an angle of 56^o to the loading direction and developed in the thickness direction over the minimum cross section. This is in good agreement with the result from analytical calculation of (Hutchinson and Tvergaard 1980) for the formation of shear bands under plane strain condition in an elastic-plastic solid with strain hardening exponent of 0.1.
- It is clear that strain levels as large as 0.4 develop near the notch tips (see Figure 3.6). It is common practice to take the largest strain measured with the DIC to be the "failure strain" in the material. This, however, ignores a couple of important

aspects of the measurement. First, DIC does not resolve the extremely high strains near the crack tip due to destruction of the speckles, decorrelation and other experimental effects associated with DIC. Second, strain continues to evolve within localized bands as material separation occurs with significantly larger local strains than that captured by the DIC. Although direct images acquired using the DIC system (at 1 frame per second) are typically not able to resolve the final events leading to the failure, visual observation clearly indicated the onset of cracking at the notch region(s), propagating quickly towards the center of the specimen. Therefore, it is expected that the local strains at the point of failure initiation are somewhat higher than the strain obtained by DIC at the last frame. Additional ***local*** measurements must be made *post-mortem* as discussed next in order to identify a material "strain-to-failure".

The notched tension response of the material is explored further through two additional investigations; first, optical and scanning electron microscopy observations and measurements were performed on specimens recovered after unloading to various gage displacement levels in order to reveal the details of the deformation leading to failure. The specimens were cut to expose the planes $y = 0$ as well as $y = 7.14$ mm (denoted as section a-a and b-b, respectively, in Figure 3.4b and in the subsequent discussion) in order to evaluate the local strains as well as to examine the onset and growth, if any, of damage. Second, numerical simulations were performed using J_2-plasticity theory in order to extend the constitutive characterization to larger strain levels. In this process, it became evident that plastic anisotropy played a key role in dictating the response. These are discussed in the following sections.

3.3. MICROSCOPIC EXAMINATION OF DEFORMATION AND DAMAGE

Specimens A through D that were unloaded from different loading stages of the flat notched specimens and Specimen E that was taken to the final failure were cut along lines a-a and b-b indicated in Figure 3.4b to reveal the x-z planes (thickness direction), and prepared for metallographic examination. Optical microscopy was used first for examining the grain evolution and scanning electron microscopy was used next to examine the extent of damage. The optical micrographs of the sections a-a and b-b for specimens interrupted at stages C and D and section a-a for Specimen E are shown in Figures 3.9 – 3.10. High magnification images of the region near the neck are shown in Figures 3.11 – 3.15. Comparing these images with the initial microstructure shown in Figure 3.1d, the elongation of the grains in the direction of tension and the decrease in grain size in the thickness direction at different stages of the deformation can be identified clearly. In order to obtain a quantitative measure of deformation at the grain level and to correlate the grain level strain with the progression of damage or failure, the methodology discussed in Section 2.3.2 was again used. As is apparent from the micrographs in Figures 3.11 – 3.15, and further verified by our analysis of the grain measurement, grain rotation does not seem to be significant, and hence no corrections for grain rotations were performed. The variation of the grain size across the dashed lines in Figures 3.11 – 3.15 was obtained, and divided by the mean grain size in the x-z direction to obtain an estimate of the strain in the thickness direction $\varepsilon_t = \ln\left(t/\hat{T}\right)$, where $\hat{T}$ is the mean initial grain size and t is the size of the deformed grain. The equivalent plastic strain can be estimated if the strain in the transverse direction (y-direction) is determined. For section a-a, based on the DIC measurements, we assume that a condition of plane-strain is satisfied, and hence the equivalent plastic strain can be estimated to be $\varepsilon_{eq} = \left(2/\sqrt{3}\right)\ln\left(\hat{T}/t\right)$; for the section b-b, the DIC measurements suggest that we may

assume a state of uniaxial stress, and hence the equivalent plastic strain can be estimated to be $\varepsilon_{eq} = 1.6 \ln\left(\hat{T}/t\right)$; note that the effect of anisotropy of the material has been taken into account in obtaining this estimate of the equivalent plastic strain. The variation of the equivalent plastic strain across lines marked as Line-1 through 5 in Figures 3.11 – 3.15 is plotted in Figure 3.16 as open symbols. Note that there is quite a large scatter in the grain based strains; this, however, does not arise from errors in experimental measurements. Rather, this is inherent in the process, since we divide the current grain size by the average initial grain size. In order to interpret this strain data better, the deformed grain size was averaged over eleven neighboring grains, five on either side, to obtain the mean deformed grain width, $\hat{t}_{11}$ and its standard deviation, $\Delta\hat{t}_{11}$. Then the best estimate for the true strain in the thickness direction, and its standard deviation are obtained as $\bar{\varepsilon}_t = \ln\left(\hat{t}_{11}/\hat{T}\right)$ and $\Delta\varepsilon_t = \left[\left(\Delta\hat{T}/\hat{T}\right)^2 + \left(\Delta\hat{t}_{11}/\hat{t}_{11}\right)^2\right]^{1/2}$, respectively, where $\Delta\hat{T}$ is the standard deviation of the initial grain size; the corresponding equivalent plastic strain can be estimated as indicated earlier. The red solid lines in Figure 3.16 indicate the equivalent plastic strain averaged over eleven grains. It is important to note a few points regarding these strain measurements.

- There is only a small difference in the strain magnitudes between the sections in plane strain (a-a) and the sections in uniaxial stress (b-b), but the maximum observed strain levels in both locations are quite large, in the range of 0.5 to 1.3.
- In the locations where shear bands appear, the local mean strains can be as large as 1 ± 0.3; in comparison, the maximum surface strains measured by DIC just prior to failure are only about 0.5. This indicates that the final stage of the ductile failure is a localized process where large strains occur due to flow localization of microstructure in a thin layer of the material.

- There are large local fluctuations in the strain distribution, and furthermore, the specimen to specimen variation appears to be quite high. With particular reference to Specimens C and D, both of which were unloaded just prior to reaching final failure, it can be seen that the maximum strains are significantly larger in Specimen C than in Specimen D.
- It is interesting to contrast these strain measurements with the usually postulated strain-to-failure models such as the Johnson-Cook and related failure models. We will return to this aspect in Section 3.4 where we show that these local strains are significantly larger than typical values used in the Johnson-Cook model where the strain-to-failure is obtained from macroscale measurements.
- Emergence of the macro-shear bands across the cross-section at an angle of 56^{o} to the loading direction, with highly localized strains within the bands, and the associated high level of stress triaxiality in the specimen triggers failure processes such as nucleation, growth and coalescence within this plane of localization. The resulting fracture is slanted in the x-z plane as can be seen clearly in Figures 3.9, 3.10 and 3.15; it should be noted that final failure is due to the merging of failure along the two equivalent planes of shear banding, resulting in a zig-zag shape of the fracture surface observed in these images.

The spatial resolution of the optical micrographs of the etched specimens is not sufficient to reveal the nucleation of damage at the location of the second phase particles. In order to investigate the formation and evolution of cavities and damage in the material, the same metallographic samples were examined in a scanning electron microscope. The micrographs of Specimen A did not reveal any differences from the unstrained material; there is a distribution of second phase particles, but there is no indication of fracture or

debonding of these particles from the matrix. A typical micrograph of section a-a of Specimen B is shown in Figure 3.17a. The irregularly shaped white areas represent the second phase particles. Sporadic breakage and debonding of a few second phase particles, especially the larger particles could be seen; a high magnification image of a fractured second phase particle is shown inset in Figure 3.17b. However, it should be emphasized that very few of the particles had fractured with most of the second phase particles undamaged and still bonded to the matrix. If particle fracture is associated with ***nucleation*** of cavities for a ductile void growth model (Tipper 1949; Puttick 1959), then correlating the grain based strain measurements in the optical micrographs, and the damage identified in the scanning electron micrographs, these observations and measurements indicate, that cavities are not nucleated until very high strain levels on the order of 0.5 to 1 are reached. In contrast, the typical value of ε_N (mean nucleation strain of a normal distribution model introduced by Chu and Needleman 1980) used in literature is 0.3 (Brocks et al. 1996; Zhang 1996).

Note that the Specimen B corresponds to macroscopic response that is *well beyond the peak load and approaching failure conditions*; the absence of significant fracture or debonding of the second phase particles indicates that much of the descending portion of the nominal stress vs. normalized crosshead displacement curve corresponds to plastic deformation of the material and not to damage accumulation; of course, it is important to recognize that this conclusion is applicable to Al 6061-T6 and could be material dependent. Scanning electron micrographs of the sections a-a and b-b of Specimens C and D are shown in Figures 3.18 and 3.19; these show the regions where the final failure is expected to develop. Clearly, a few scattered cavities can be identified in these micrographs. Such features in the micrographs are typically interpreted as evidence for the nucleation and growth of voids. However, before confirming such a conclusion,

one must rule out damage resulting from metallographic specimen preparation procedures. The typical argument that is put forward to exclude polishing damage is that other regions in the specimen have also been subjected to the same polishing procedures, but did not reveal any such damage. In order to pursue this idea further, we consider quantitative comparison of the optical micrograph that reveals grain and grain boundaries with the scanning electron micrograph of the same region of the specimen. This comparison is shown in Figure 3.20 where Figure 3.20a is an optical micrograph, Figure 3.20b is a scanning electron micrograph of the same region and Figure 3.20c is a composite overlay of the SEM image over the optical image, with an opacity of about 0.5. With the overlaid image as a guide, attention is now focused on regions marked by the blue, dashed circle and square in Figure 3.20b; high magnification images of these features are presented in Figure 3.21 where the grain boundaries can be easily identified. Clearly the entire grain appears to be missing in Figure 3.21a; if a nucleated void were to grow, the grain surrounding it has to deform to accommodate such a large growth and should be identifiable in the micrograph. However in the regions outlined by the dashed circles in the micrographs, the entire grain is lost suggesting that these grains must have been pulled out during polishing. Such pull-out may, of course, be facilitated by the fact that these grains have probably at least partially debonded from the second phase particles when a combination of critical stress state and plastic strain is reached. We do not observe such large pulled out grains in Specimens A, B and even C. This raises the issue of accurate metallographic quantification of porosity: since even under precise conditions the presence of artifacts resulting from metallographic preparation is unavoidable, new non-destructive techniques such as x-ray tomography are being developed as potential candidates. Attempts to obtain the reconstructed 3D x-ray

tomography images of the voids in interrupted specimens, however, did not succeed due to insufficient spatial resolution of images.

In order to develop quantitative measures of damage from the micrographs in Figures 3.18 and 3.19, a grid of square cells of size 150 μm is overlaid on the images to provide a symbolic representative area element of the material. Discounting cavities that have been identified to be the result of pullout of grains, the area fraction of the remaining cavities are calculated for three cells at the center of the section marked in each of Figures 3.18 and 3.19; these measures of these voids are given in the Table 3.3.

The size of cavities is in the range of 1-5 μm; the spacing between these cavities is on the order of 35-45 μm. Comparing this to the average spacing of the second phase particles (25 μm), it is clear that not all second phase particles are trigger points for voids; this is also identifiable from the micrographs. It is seen from the Table 3.3 that the area fraction of cavities is larger in Specimen D than in Specimen C at the two sections a-a and b-b. This is of particular importance in that both Specimens C and D were unloaded at about the same point in the nominal stress vs. normalized crosshead displacement response; yet the different damage levels experienced by the two specimens can be attributed to the stochastic nature of the void nucleation, which, in turn, stems from the variation in the microstructure of the material. Furthermore, the local strains in Specimen C exhibiting smaller amount of voids is larger than in Specimen D. The absence of significant damage in Specimens A and B, and the appearance of a small number of voids in Specimens C and D that were loaded to the brink of failure indicates that nucleation of damage from the second phase particles in the form of debonding and/or particle fracture occurs rather late in the overall straining of the material. Correlating the local grain based strain in the Specimens C and D, as shown in Figure 3.16, to the emergence of the voids, we can suggest that nucleation of damage in Al 6061-T6 occurs at equivalent strain levels

close to ~ 0.5. Of course, one must bear in mind that the nucleation strain level will be a strong function of the properties of the matrix, the second phase particles, the interface characteristics and stress state. Lee and Mear (1999) made an estimate of the stress concentration in ellipsoidal inclusions in a power law hardening material. Their results indicated that the stress concentration at the cavity boundaries saturated after rising quickly with strain. This is often taken as indication that cavity nucleation must occur either at very low strain levels or not at all. The present results suggest that cavity nucleation could occur at high strain levels.

Fractographs of Specimen E at the intersection of sections a-a and b-b with the fracture plane are shown in Figures 3.22a,b. These images exhibit numerous dimples that are characteristics of the development of ductile fracture through the nucleation, growth and coalescence of cavities. Almost all of the larger dimples contain a second phase particle inside its boundary, indicating that these particles are, indeed, the nucleation sites. The void surfaces themselves appear 'terraced' or stepped, suggesting crystallographic slip as the deformation process during void growth; there is no evidence of any other mechanism of failure. The overall fracture plane is tilted at an angle about 56º to the loading direction, which is in line with the inclination of the shear bands that developed preceding the final failure (see Figure 3.15). While dimpled images of fracture surface are typically shown to provide qualitative support for the mechanism of failure, it is possible to obtain significant quantitative measures of fracture. We begin with a consideration of the statistics of cavities: by identifying the boundaries of each cavity, as indicated in Figure 3.22a (only half the image was analyzed), we identify the centers and equivalent diameters of each cavity in the fracture plane. The distribution of areas of the cavities is shown in Figure 3.22c; the histogram appears to indicate three groups or clusters of void areas; first, there is a large number of very small voids (diameter < 10

μm); these appear typically at the junctions between larger cavities and are most likely the secondary voids that arise during coalescence between primary voids. Second, there seems to be a cluster of voids of size ~25 μm, and another cluster ~18 μm; these appear to correlate to the mean size of the grains in the y-z plane. From these measurements, we estimate that the primary voids are nearly of the shape of the grains, and cause separation of the grains; some of the voids that are of the average size of the grain in the y-z plane are identified in Figure 3.22a by the red lines. Smaller, secondary voids appear in the region of coalescence of the primary voids or at grain boundaries; a few of these smaller cavities are highlighted by the blue lines in Figure 3.22a. But the most important observation that deserves reiteration is that the *entire fracture surface is tiled with the dimpled features* and, therefore, every point in the y-z plane belongs to a void.

We now contrast this with an examination of the plane orthogonal to the fracture plane. SEM micrographs of the Section b-b of Specimen E' (another broken specimen) is shown in Figure 3.23; these micrographs allow an examination of damage in the planes that are below the fracture plane. A depth of about 500 μm below the fracture surface at two different locations is shown in this figure; a higher magnification view of the region just below the fracture surface is also shown inset in Figure 3.23c. A small number of second phase particles can be seen to have been broken and/or debonded from the matrix; the 'voids' resulting from such damage appear to have elongated slightly in the direction of tension. However, the damaged particles appear in clusters, leaving large regions of the material below the fracture plane completely undamaged, exhibiting no systematic development of voids. Grain boundaries are clearly visible in the micrograph and these appear to be undamaged as well. In contrast to the appearance of the fracture surface that was tiled with voids, we can see that *almost no point below the fracture plane at locations that are as close as 30 μm experiences nucleation or growth of voids* and

therefore in contrast to the fracture plane, *almost* no point in the x-z plane is part of a void/nucleation or growth process.

Comparison of the number and distribution of voids on the fracture plane and the planes below the fracture plane indicates that, indeed, ductile fracture in Al 6061-T6 occurs by void nucleation, growth and coalescence; however, it occurs in an extremely localized manner, with almost no statistically significant void nucleation or growth at locations as close as 30 μm away from the fracture plane. It is easy to recognize that this scale must be set by the grain size by the following argument: nucleation of voids is seldom a homogeneous process, but governed by the heterogeneities, especially by the extreme fluctuations. Therefore, we can postulate that the first failure of a single grain by void growth would be triggered by the weakest heterogeneity in the region of the largest stress; when failure of this grain occurs, the load is shed to the neighboring grains, triggering the nucleation and growth of the next void in these grains, even if the heterogeneities in this grain are not as weak. The cascading of such a process results in a localization of the failure process to the "failure plane". Outside of this plane, plastic deformation occurs to very large equivalent plastic strain levels without significant damage (see Figure 3.16).

The optical and scanning electron micrographs of specimens that failed as well as those that were interrupted prior to failure provide a picture of the evolution of deformation, damage and failure in Al 6061-T6; we summarize our observations here.

1. Nucleation of damage does not appear to occur until equivalent plastic strains of at least about 0.5; much of the post-peak response of the specimen, can be attributed to the formation of necking and shear bands in the specimen and not to development of material damage.

2. Once damage in the form of breakage or debonding of the second phase particles begins, subsequent failure occurs with little further increase in macroscopic strain. Specimens that were unloaded, and specimens that were fractured, reveal that there is not a significant number or distribution of voids left in the wake of the fracture at distances greater than about 30 μm from the fracture plane.
3. The fracture plane is tiled with voids indicating that void nucleation, growth and coalescence is the essential mechanism of crack growth; however, dominated by the fluctuations in the distribution of second phase particles, failure by void nucleation, growth and coalescence occurs in a highly localized region on the order of the grain width.

3.4. NUMERICAL SIMULATION

As mentioned earlier, the variation of stress throughout the notched specimens in experiments can only be evaluated by means of numerical simulations. A commercial finite element software ABAQUS™ was used to perform these calculations. Finite element models are created for each test using two different material models – an isotropic von Mises plasticity model and the Hill quadratic anisotropic plasticity model, both available in the ABAQUS standard material library. The Lankford r-values identified from DIC measurements and shown in Table 3.2 were used to represent the material anisotropy; these parameters were used in the Hill's anisotropic plasticity material model in ABAQUS/Standard. Comparisons of different material models with experimental responses will be presented for each specimen.

3.4.1. Uniaxial Tension Test

The uniform region of the dog-bone specimen was modeled in ABAQUS with 3D linear continuum elements with reduced integration (C3D8R). A very fine mesh was adopted in the middle part where the necking occurs, and gradually coarsened towards the ends. The minimum mesh size was 0.20 mm; 9 elements were used across the 2.44 mm thickness of the specimen. Nodal displacements in the axial direction were prescribed at the top and bottom boundaries of the specimen; the transverse tractions were set to zero in order to mimic the uniaxial tension test. The elastic–plastic constitutive model of the material used in the finite element simulations are extracted from the uniaxial tensile test up to the onset of necking. In order to trigger the localization, 3 elements at the center surfaces of the model parallel to the x-z plane were given a yield strength of about 0.1 of the rest of the model to serve as imperfection site. The post-necking material behavior was obtained by an inverse method; in this method the hardening behavior of the material is extrapolated linearly according to the current tangent modulus and the nominal stress vs. normalized gage displacement response from numerical simulation is compared with the experimental response, and iterating by decreasing the modulus until acceptable agreement of the load is reached. This trial-and-error process is continued until the entire nominal stress vs. normalized gage displacement response of the specimen is recovered in the simulation. Special care should be taken in this process as the elastic-plastic response has a great influence in determining of deformation modes in different types of loadings. The simulated nominal stress vs. normalized gage displacement curve is compared to the experimental measurement in Figure 3.24a; the true stress-true plastic strain curve obtained by the iterative process is shown in Figure 3.24b. It is seen that Hill's anisotropic model captures the experimental response of the uniaxial tension test reasonably well.

3.4.2. Notched Tension Test

The response of the flat, notched tension specimen is considered next. Due to symmetry half the specimen was modeled with 3D continuum elements (C3D8R) with 31 elements through the thickness; a finer mesh size of 50 μm was used in the minimum cross section (Figure 3.25).

The nominal stress vs. normalized gage displacement curve from simulations using isotropic plasticity (von Mises yield function) and anisotropic plasticity (Hill quadratic yield function) are compared to that from the experiment in Figure 3.26.

As can be seen from Figure 3.26, the Hill anisotropic plasticity model captures very well the material response during the deformation history while the isotropic model prediction is not satisfactory. Note that no failure model or criterion has been used in the simulations; thus the response is entirely due to plastic deformation. This also means that the termination point is not obtained in the simulations. The nominal stress vs. normalized gage displacement response gives the global response of the material where the effects of localization are smeared out; therefore, we consider comparison of local field measurements to assess the capability of the constitutive model. To this end, the variation of surface axial strain ε_x along the lines y_1-y_2 and x_1-x_2 (see Figure 3.4b) from simulations and experiments for three different normalized gage displacements (corresponding to Specimens A, B and C) are plotted in Figure 3.27. It is seen that the numerical simulation with Hill anisotropic yield function captures the essential features of the deformation observed in the experiment. From the Figure 3.27a it is observed that the strain prediction is in fairly good agreement with the experiment for much of the line y_1-y_2. The peak near the notch tip that occurs at $y = 7.14$ mm due to the necking at this

location is also realized; however the simulation results are slightly higher with the difference increasing with the overall deformation. In Figure 3.27b, the double peaks that correspond to the formation of shear bands across the thickness of the specimen are also captured with the Hill plasticity model. After the localization of deformation in the form of intense shear bands, the central portion of the specimen outside these localized bands experience a smaller increase in strain.

The quantitative discrepancy between the experiment and the numerical simulations can be attributed to the following: first, adopting an appropriate constitutive material model that takes into account different characteristics of the material microstructure such as grain morphology and crystallographic texture during the multiaxial deformation is of great importance in order to achieve precise numerical predictions. For aluminum alloys, plasticity models based on a non-quadratic yield function that accounts for anisotropy have been developed and implemented in finite element software (Barlat et al. 2003; Korkolis and Kyriakides 2008a,b); however these complex models require calibration of several parameters and has not been attempted in this work. However, as mentioned earlier the main focus of this work is on the events leading to the final failure in ductile materials rather than building a plasticity constitutive relation. The Hill anisotropic plasticity model adopted here seems to capture the essential characteristics such as onset of necking as well as the development of shear localization through the thickness. Therefore, it is concluded from comparison to the experimental results that the Hill anisotropic plasticity model can be used as a reliable tool to predict the evolution of stress state especially stress triaxiality during the deformation.

The numerical simulation allows us to correlate the strain at the grain level with the stress triaxiality at the critical points in the specimen. Figure 3.28a shows a sectioned view from the simulation indicating contours of triaxiality; the variation of the stress

triaxiality at different gage displacements across the dashed line marked in Figure 3.28a is shown in Figure 3.28b. Initially, the maximum triaxiality occurs in the center of the specimen (~plane strain, 0.50) and decreases gradually towards the notch which is in uniaxial tension state. However this trend changes with the deformation; it is seen that at the brink of failure (Specimen C) the maximum triaxiality of about 0.82 occurs near the notch ($y = 7.14\text{mm}$) while it is about 0.68 at the center. The change in the location of maximum stress triaxiality from the midpoint of the specimen to the notch tip region during the deformation should particularly be emphasized as it potentially determines the location of macro crack initiation that finally leads to final failure of the specimen; experimental observations indeed confirmed nucleation of failure in the notch tip region. This was also the main reason for selecting the section b-b for metallographic examination and measurements.

Phenomenological fracture models such as Johnson-Cook and modified Mohr-Coulomb criteria have been developed and used extensively in the numerical simulation of fracture in ductile material. In these models the model parameters are usually calibrated by measuring the strain in the gage section of a broken specimen or using a hybrid experimental-numerical method; in the latter the force-gage displacement response of the specimen is used as the measure of fitness and the calculated strain at the critical point corresponding to global failure is taken as the intrinsic material strain-to-failure for a given level of triaxiality. Just as in the case of OFHC copper (Chapter 2), in this section we give a conservative lower bound estimate of the strain-to-failure for Al 6061-T6 that is rooted in the grain based measurement of strain. It was shown in Section 3.3 that strains in the range of 0.5 – 1.0 could be measured in the specimens just before the final failure. The stress triaxiality in the region b-b at this stage of deformation is obtained from the finite element analysis to be about 0.82. We now place this point

represented as a red band on a plot of strain-to-failure vs. triaxiality (see Figure 3.29); for comparison, the Johnson-Cook model calibrated for Al 6061-T6 by Lesuer et al. (2001) is also shown. As readily seen from the Figure 3.29 the strain-to-failure obtained at the level of grains that are building blocks of the material lies distinctly above the fracture locus of Johnson-Cook; the arrow on the red band indicates that the true fracture strain could be even larger as we report the strain in the specimens just before the final failure; furthermore, we consider the lower bound of the measured range of strain values. The difference from the Johnson-Cook type models arises from the fact that we have used an intrinsic length scale based on the microstructure – the grain size – as the basis for the definition of an invariant strain measure.

3.5. SUMMARY

Tension tests and interrupted flat notched tension tests were performed on Al 6061-T6 in order to examine the evolution of the microstructure at different stages of the deformation. The macroscopic strain fields were monitored with a variation of the digital image correlation method called Q4-DIC which was adopted and implemented in MATLAB.

Samples from interrupted tests were sectioned, polished and etched following standard procedure for metallographic examination. The initial microstructure of the Al 6061-T6 was examined and the grain size was determined; it is evident from distributions of the grain size that the grains are equiaxed in the rolling plane (x-y plane) with the mean size of 39 μm. The average grain size in the z-direction is about 14 μm. This grain size distribution suggests planar isotropy in the microstructure. The microstructure of this

material shows a dispersion of mostly iron-based second phase particles with volume fraction in the range of 0.012 and mean particle spacing in the range of 25 μm.

Evolution of deformation in the microstructure was obtained by direct measurements of grain size using optical microscopy. Correlation of strain estimates at the grain level with the process of damage evolution using scanning electron microscopy was made at different levels of macroscopic deformation. This allows characterization of the damage in a multi-scale frame work.

It was concluded that in Al 6061-T6 under tensile loading, nucleation of damage does not appear for much of the deformation history until plastic strain levels of at least about 0.5-1 is reached. Once damage in the form of particle fracture or decohesion at the interface initiates, subsequent failure follows with a small increase in the overall strain. The final separation; dominated by the fluctuation in the distribution of second phase particles, occurs by the void nucleation, growth and coalescence in a highly localized layer of material on the order of the grain size.

Numerical simulation of the experiments using von Mises isotropic and Hill's quadratic anisotropic plasticity models were performed in the finite element software ABAQUS 6.9. Lankford *r*-values were extracted by performing uniaxial tension tests in different directions. The hardening behavior was obtained through a hybrid experimental-numerical procedure. It was shown that anisotropy plays a significant role in capturing the global as well as local features of the experiment such as diffuse necking and shear banding; therefore, Hill quadratic anisotropic plasticity model was used to obtain the variation of stress state during the deformation. Values of stress triaxialities and the corresponding deformation at the grain level were compared with strain-to-failure ductile failure models such as the Johnson-Cook model. It was shown that the lower-bound

strain-to-failure estimates measured at the grain level are more than double the values usually calibrated into this model.

Table 3.1. Chemical composition of Al 6061-T6.

Wt%	Si	Fe	Cu	Mn	Mg	Cr	Zn	Ti	Others	Al
Min.	0.4	—	0.15	—	0.8	0.04	—	—	—	
Max.	0.8	0.7	0.40	0.15	1.2	0.35	0.25	0.15	0.15	Bal.

Source: Alcoa

Table 3.2. Lankford r-values at different orientations to the rolling direction.

	r_0	r_{45}	r_{90}
r-values	0.57	0.60	0.58

Table 3.3. Microstructure analysis of sections a-a and b-b of Specimens C and D.

	Mean spacing - μm			Average void area fraction		
Cell #	1	2	3	1	2	3
C- a-a	34	39	36	0.00285	0.00467	0.00226
D-a-a	41	38	72	0.00564	0.00783	0.00204
C-b-b	36	29	37	0.00447	0.00117	0.00596
D-b-b	33	41	45	0.01785	0.0107	0.00734

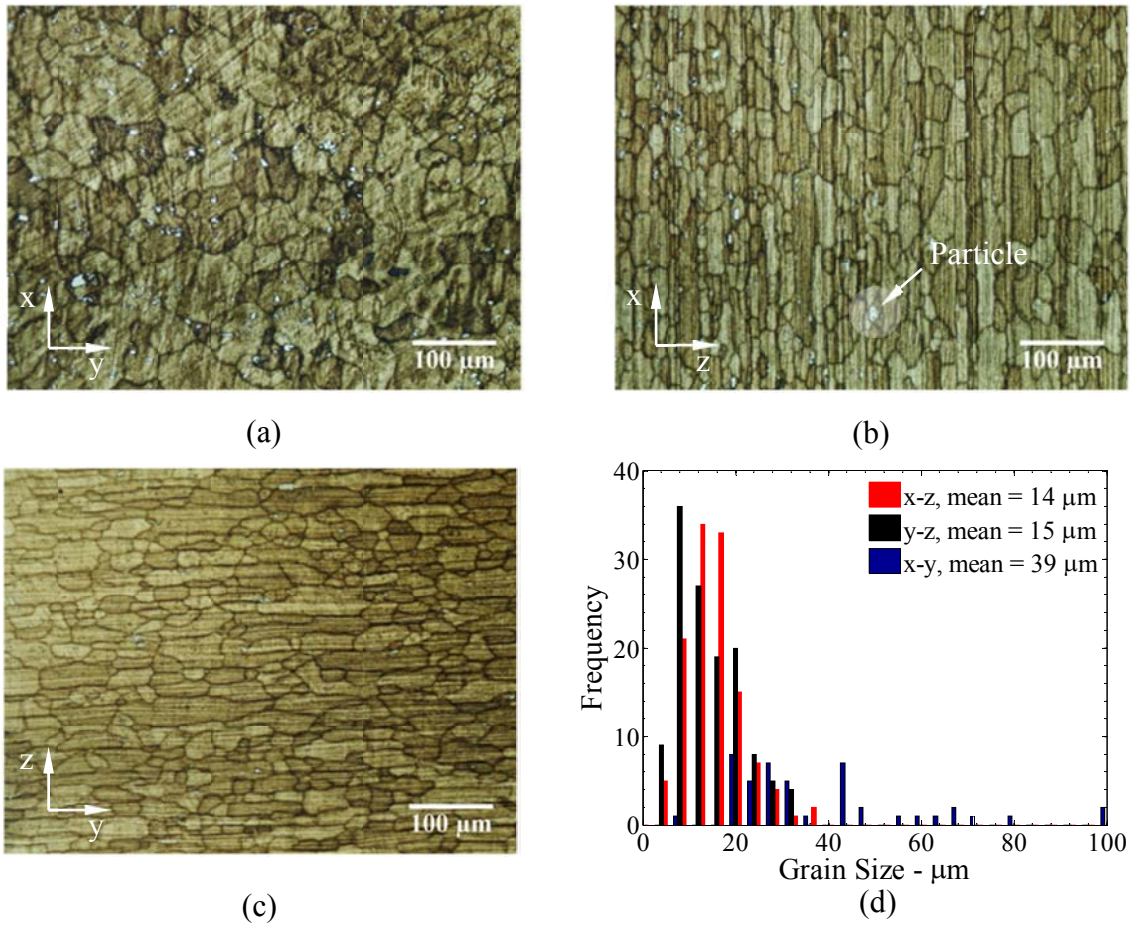

Figure 3.1. Microstructure of Al 6061-T6 in the (a) x-y, (b) x-z and (c) y-z planes. The (x,y,z) directions are the rolling, transverse and thickness directions, respectively. The distribution of the grain size in the three directions is shown in (d).

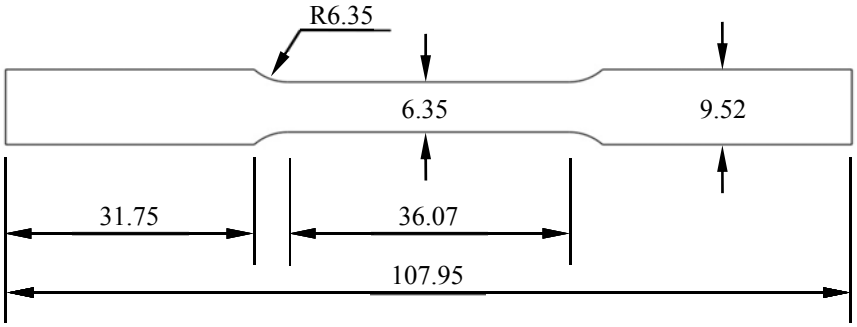

Figure 3.2. Schematic diagram of the uniaxial tension specimens (dimensions in mm).

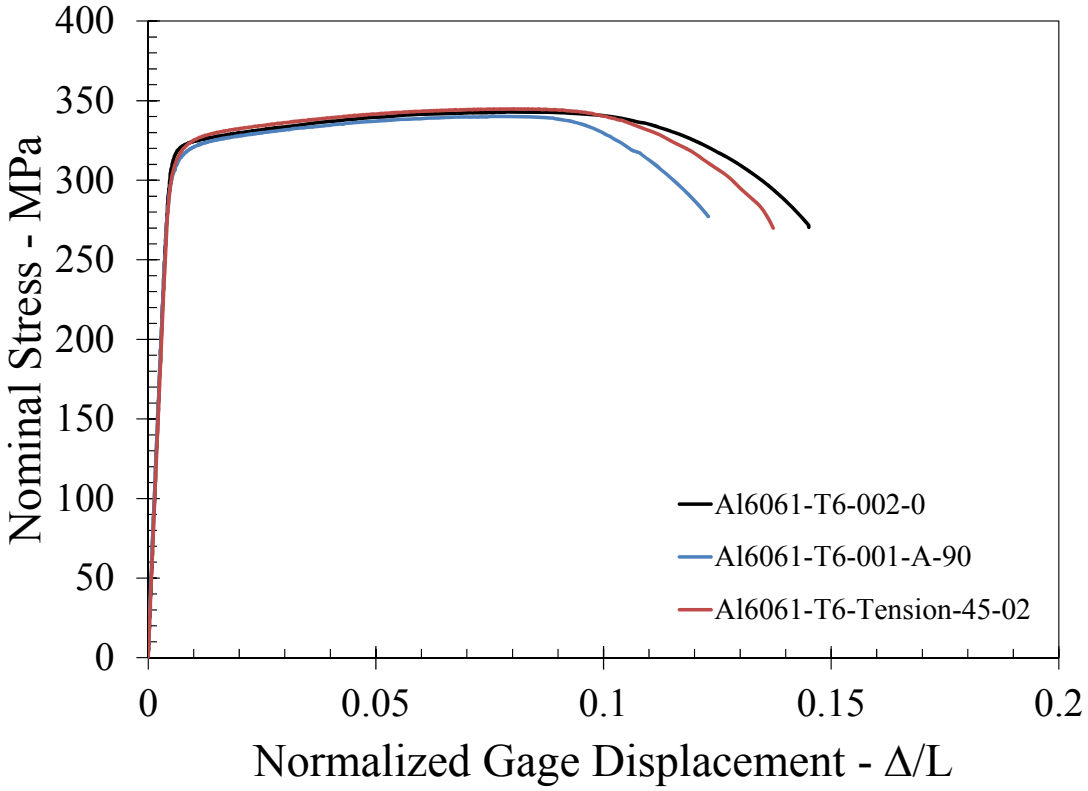

Figure 3.3. Nominal stress (force/initial cross-sectional area) vs. gage displacement (Δ) normalized by gage length (L) response at 0º, 45º and 90º to the rolling direction for dogbone specimens made of Al 6061-T6.

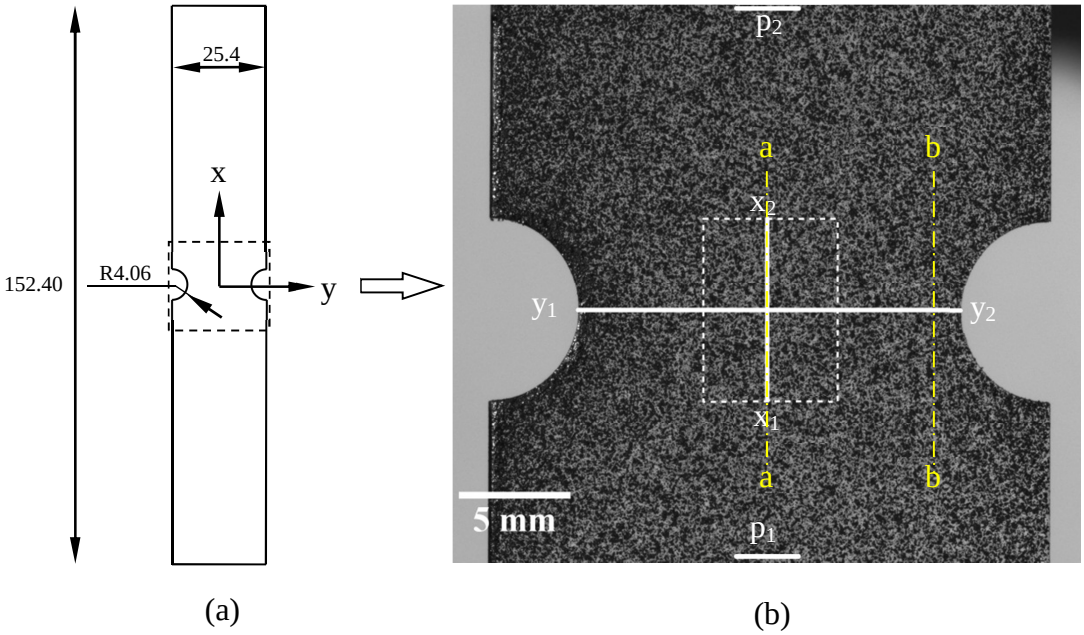

Figure 3.4. (a) Schematic diagram of the flat notched specimen (dimensions in mm). (b) Photograph of the surface of the flat notched specimen. p_1-p_2 is used to define a gage length (24.02 mm). DIC based strain measurements are reported along lines labeled x_1-x_2 and y_1-y_2. Metallographic examinations are performed on sections cut along a-a and b-b.

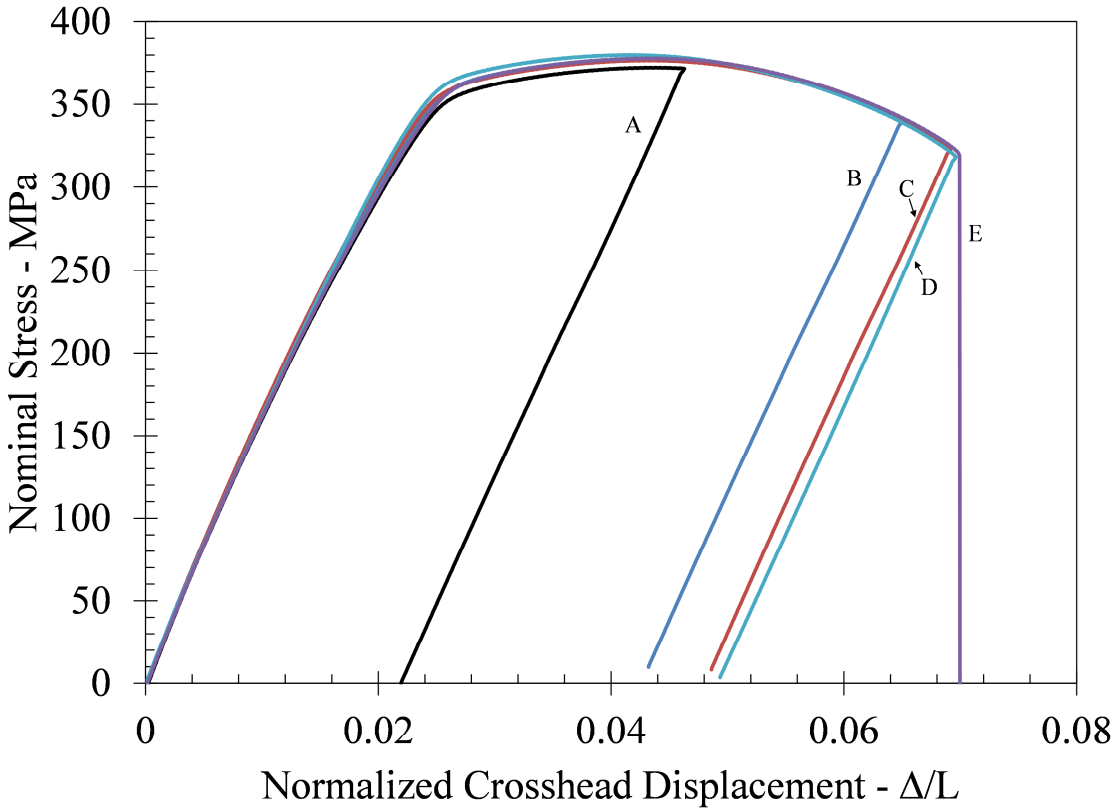

Figure 3.5. Nominal stress (force/initial minimum cross-sectional area) vs. crosshead displacement (Δ) normalized by gage length (L) (see Figure 3.4b for the definition of the gage length) curves of Al6061-T6 flat-notched specimens interrupted at different stages during the deformation.

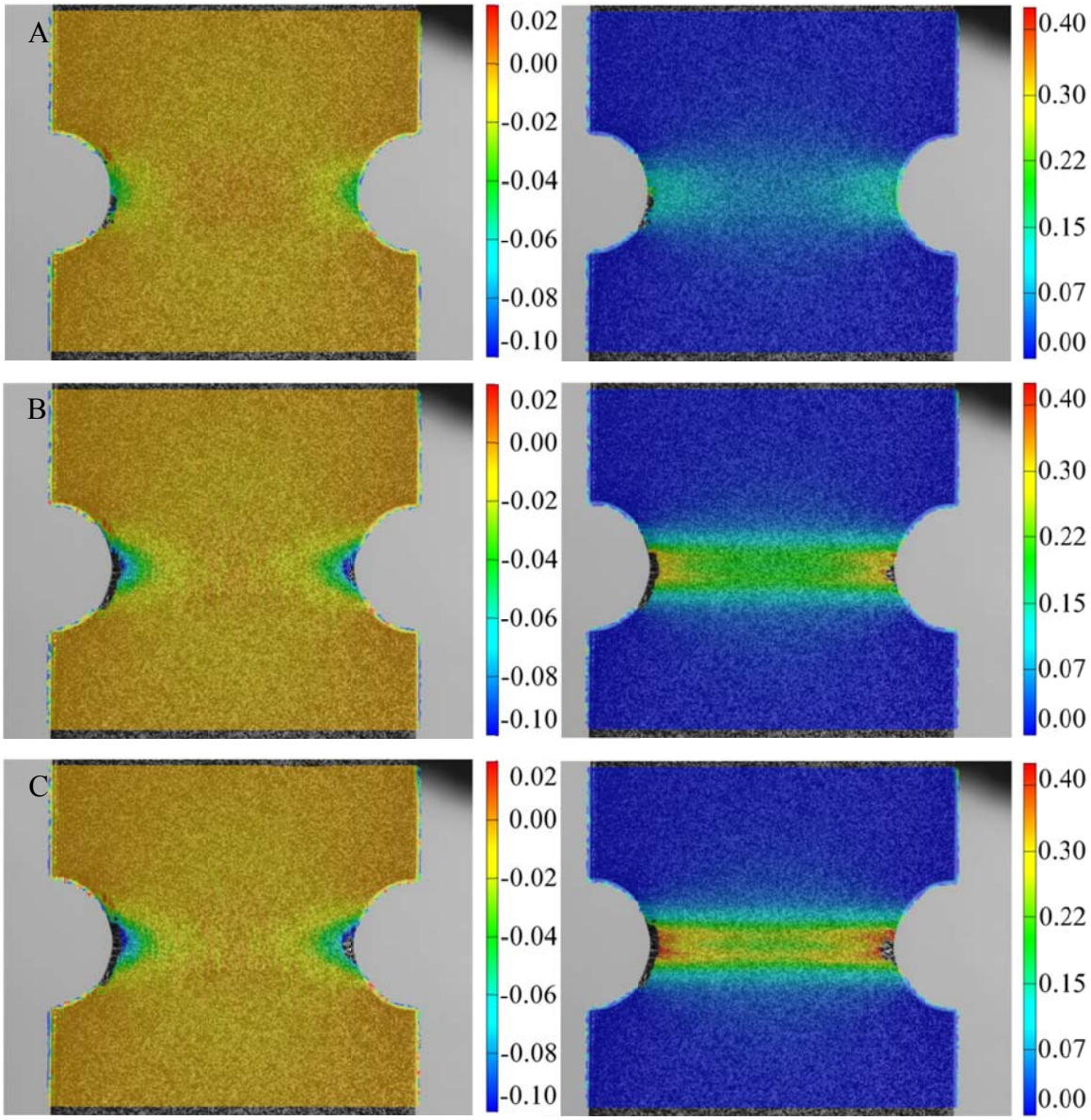

Figure 3.6. Contour plots of transverse (left column) and axial (right column) strain (ε_y and ε_x, respectively) of Al 6061-T6 flat notched specimens corresponding to three different normalized crosshead displacements (Specimens A, B and C on Figure 3.5).

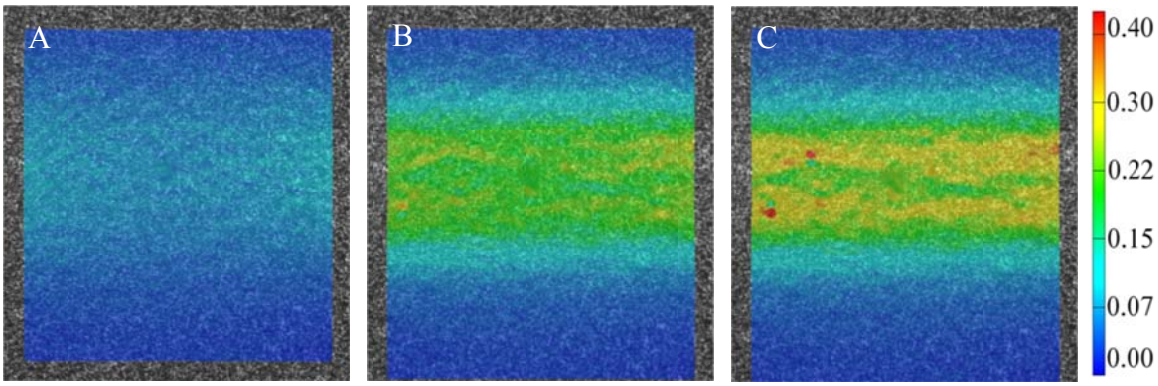

Figure 3.7. Close-up view of axial strain (ε_x) contour plots of Al 6061-T6 flat notched specimens corresponding to three different normalized crosshead displacements (Specimens A, B and C on Figure 3.5).

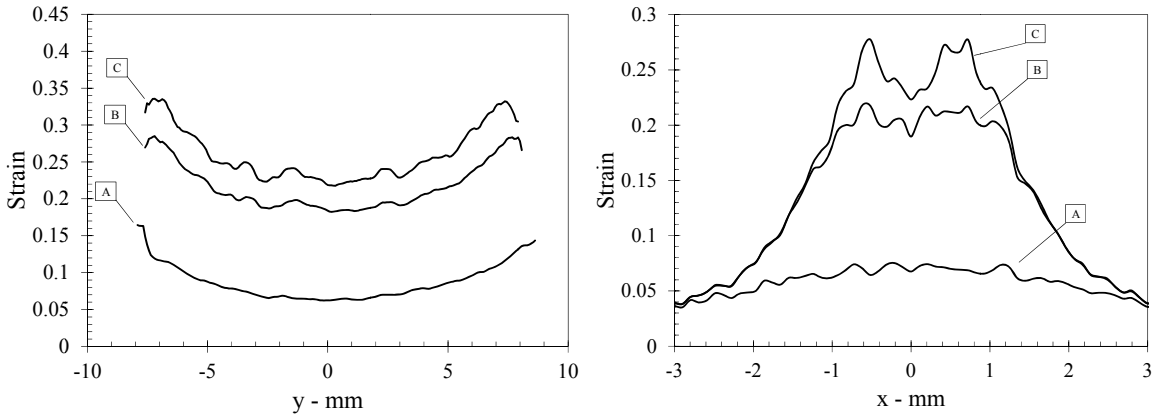

(a) (b)

Figure 3.8. Variation of the axial strain (ε_x) along lines (a) y_1-y_2 and (b) x_1-x_2 for Specimens A, B and C.

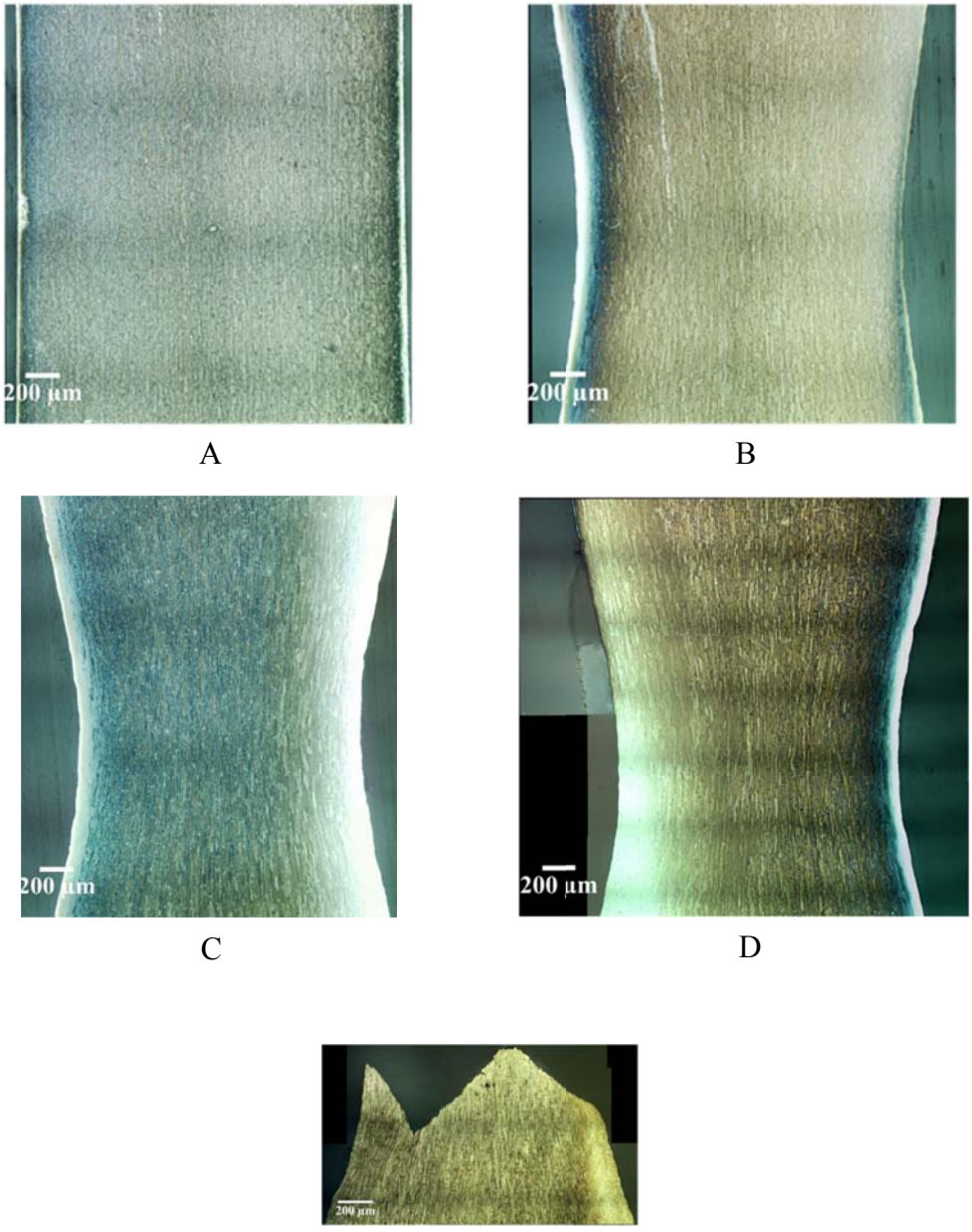

Figure 3.9. Micrographs of x-z sections of Specimens A-E at a-a.

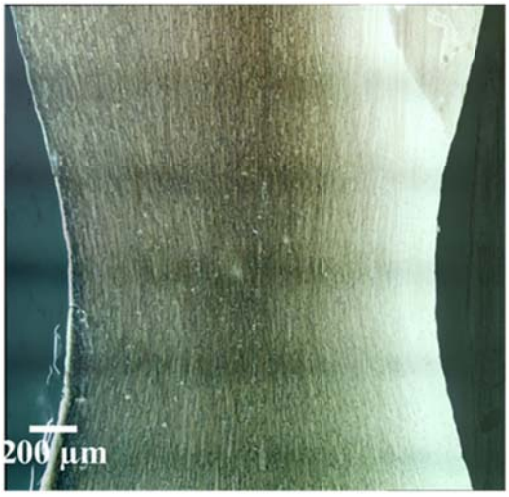

C

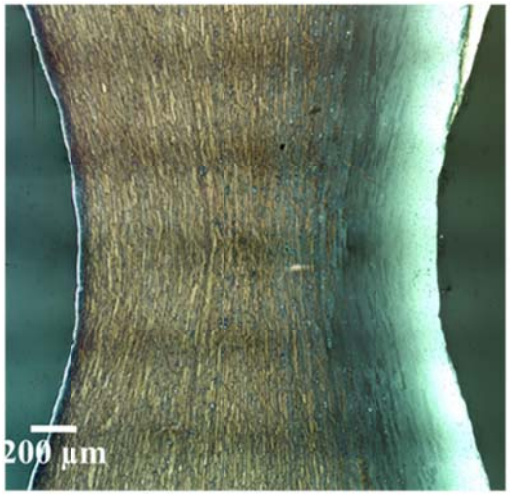

D

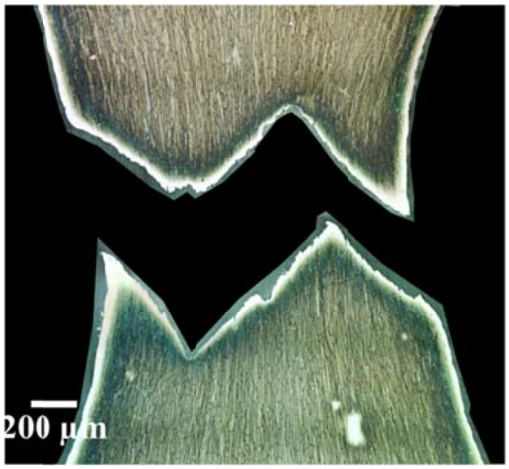

E

Figure 3.10. Micrographs of x-z sections of Specimens C, D and E at b-b.

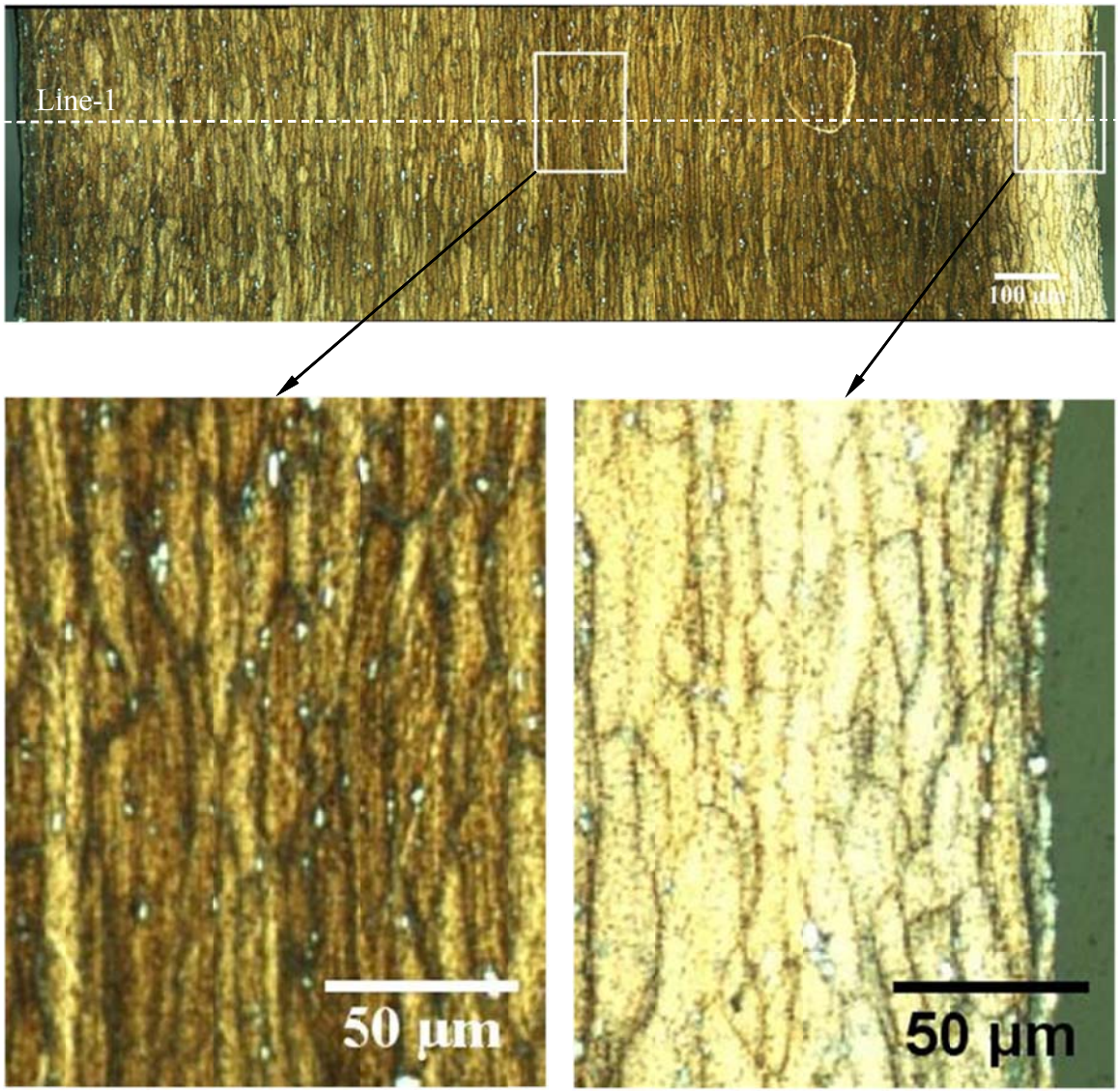

Figure 3.11. High magnification views of micrographs of the neck region of section a-a of Specimen C.

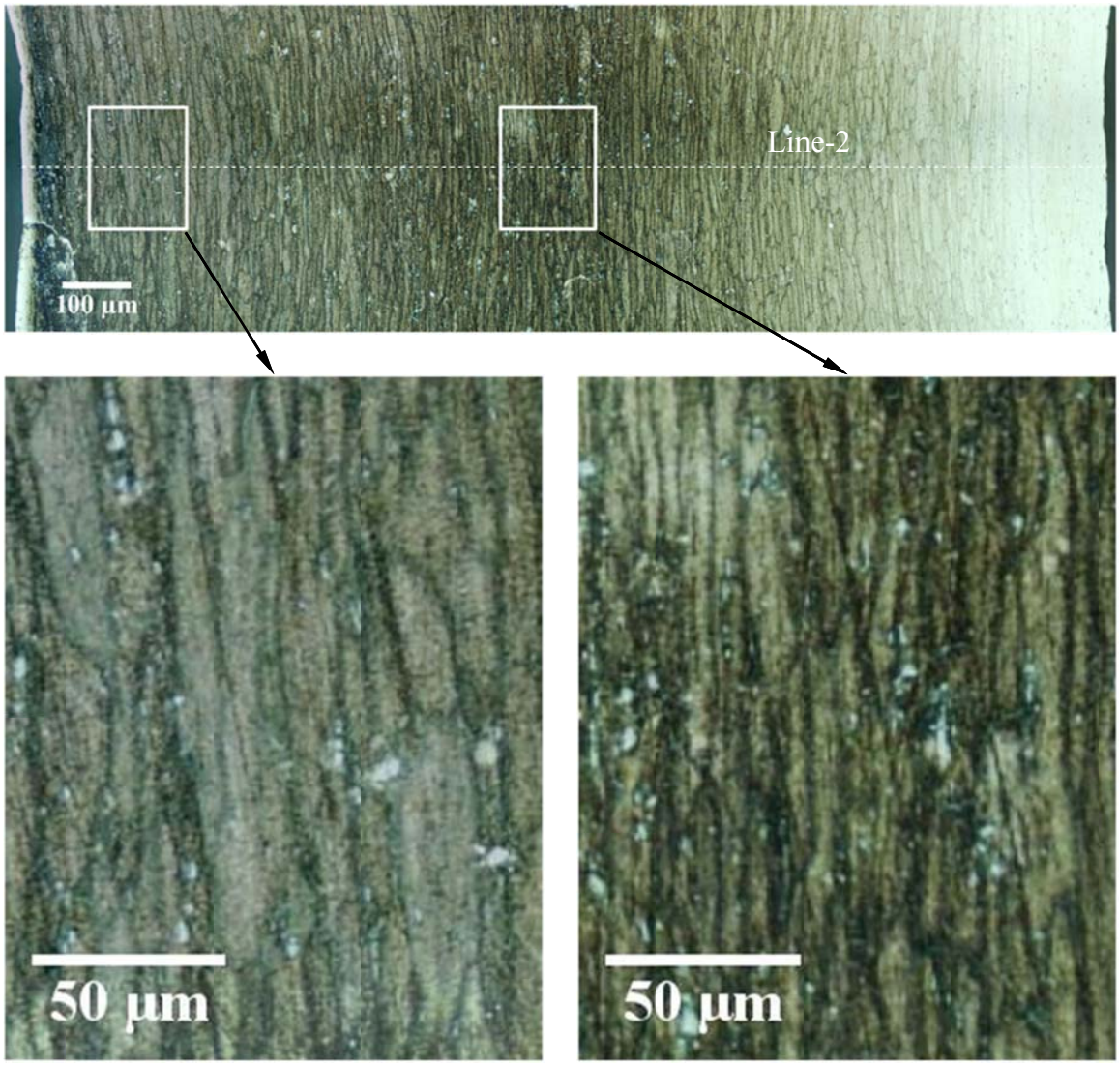

Figure 3.12. High magnification views of micrographs of the neck region of section b-b of Specimen C.

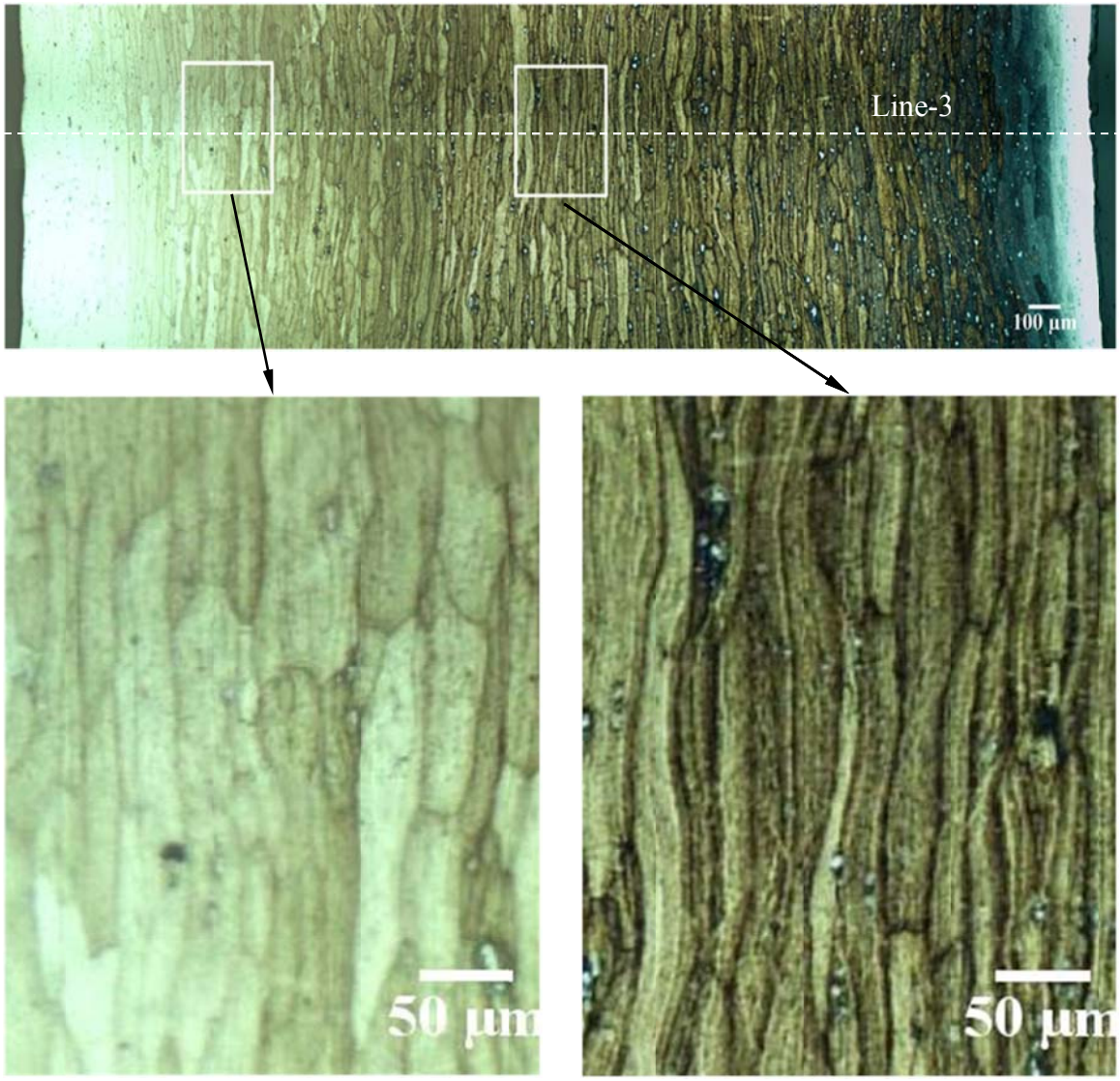

Figure 3.13. High magnification views of micrographs of the neck region of section a-a of Specimen D.

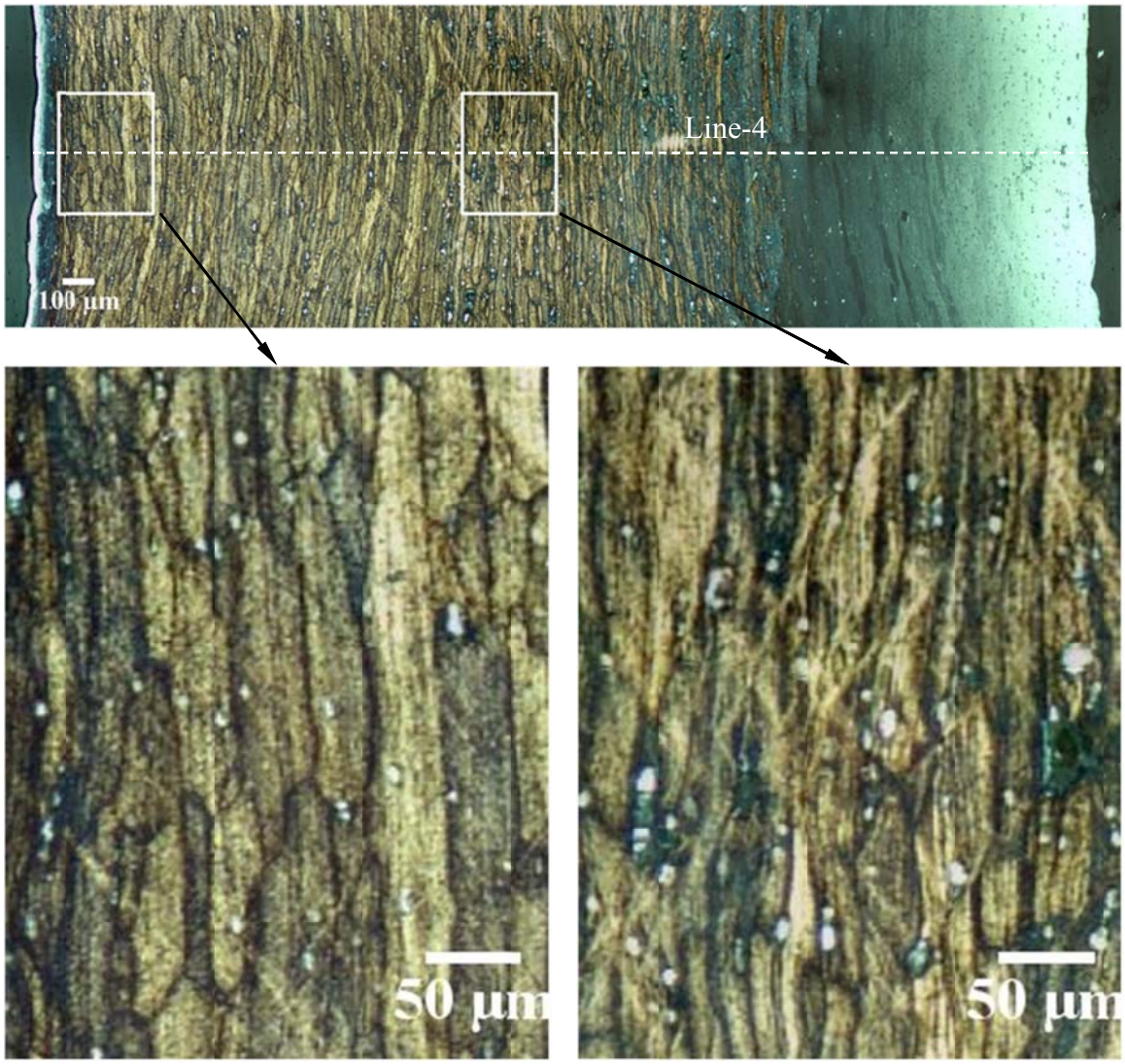

Figure 3.14. High magnification views of micrographs of the neck region of section b-b of Specimen D.

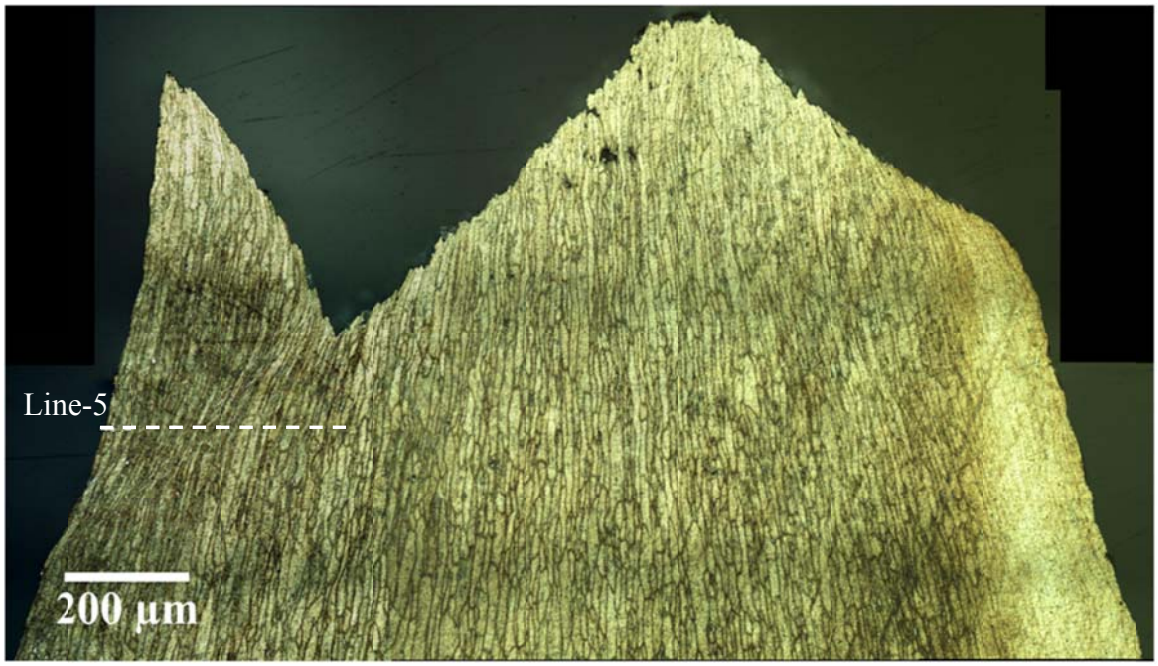

Figure 3.15. High magnification view of micrograph of section a-a of Specimen E showing a shear band along which the failure seems to occur.

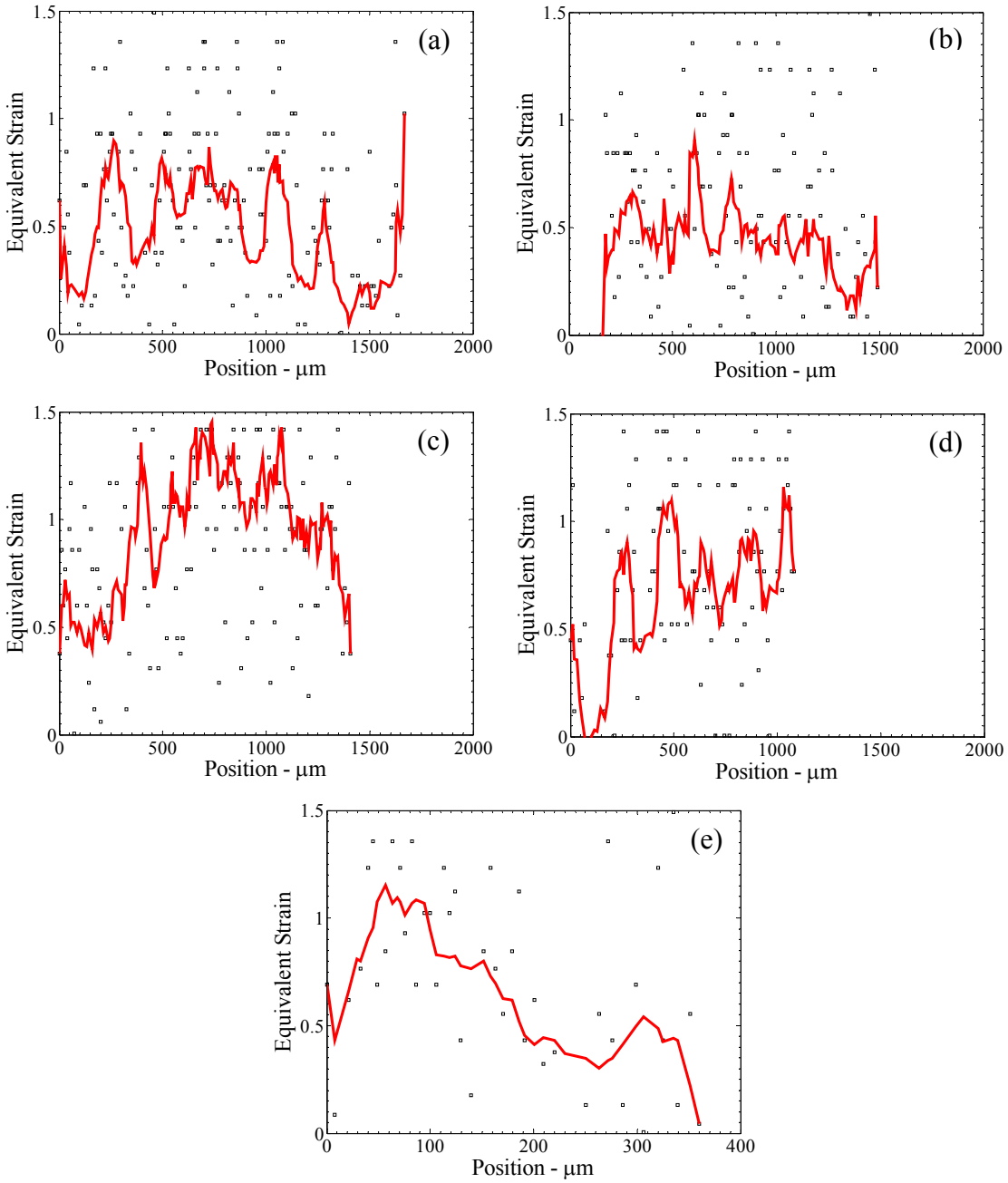

Figure 3.16. Variation of equivalent strain across the section a-a of Specimen C (a) and Specimen D (b), the section b-b of Specimen C (c) and Specimen D (d) and across Line-5 on the section a-a of Specimen E (e). Open symbols correspond to strain estimate for each grain; red line corresponds to averaging the deformed grain size over eleven neighboring grains, five on either side.

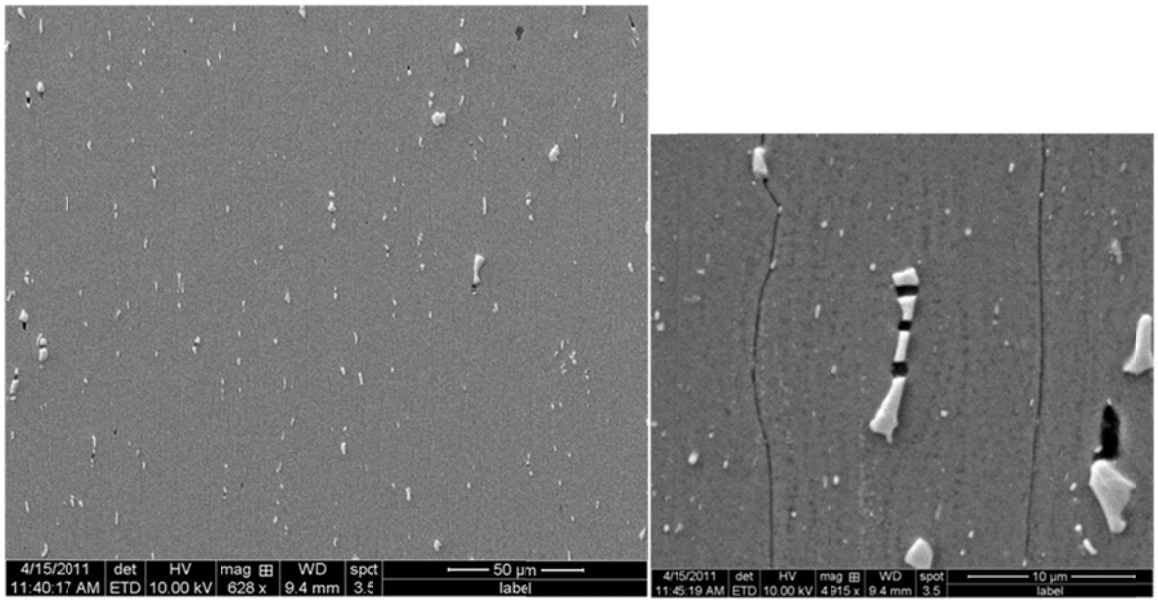

(a) (b)

Figure 3.17. SEM micrographs of the section a-a of Specimen B at different magnifications showing sporadic nucleation of cavities at second phase particles.

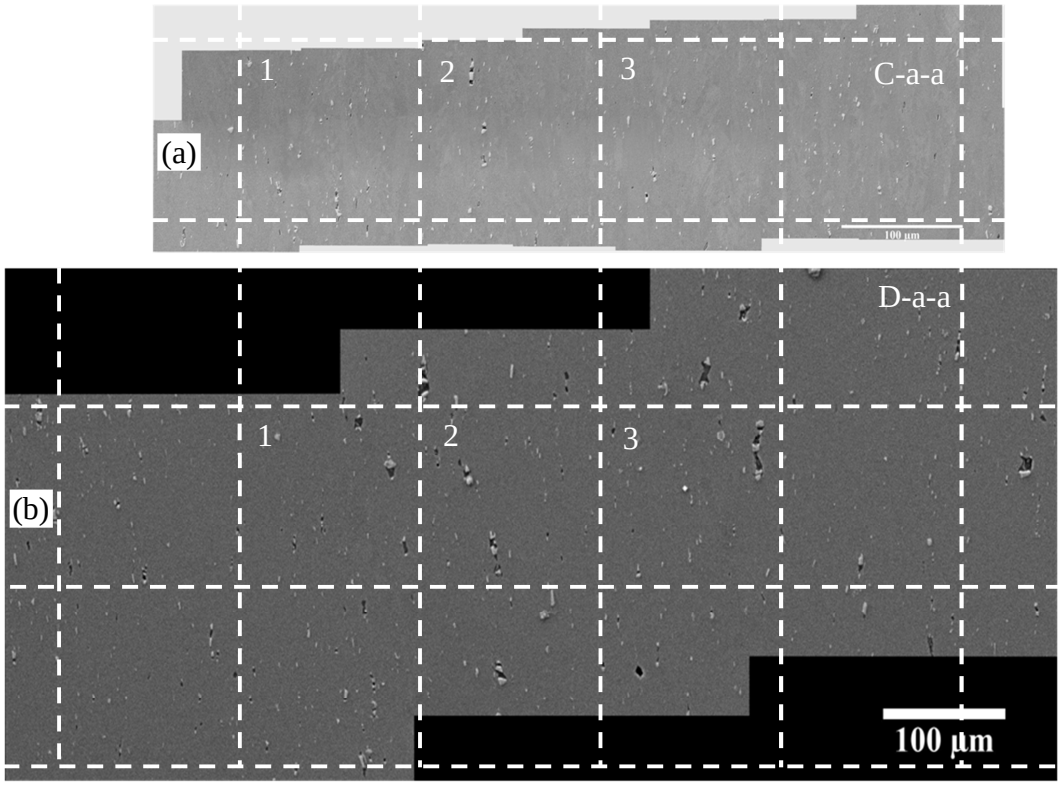

Figure 3.18. SEM micrographs of section a-a of (a) Specimen C and (b) Specimen D.

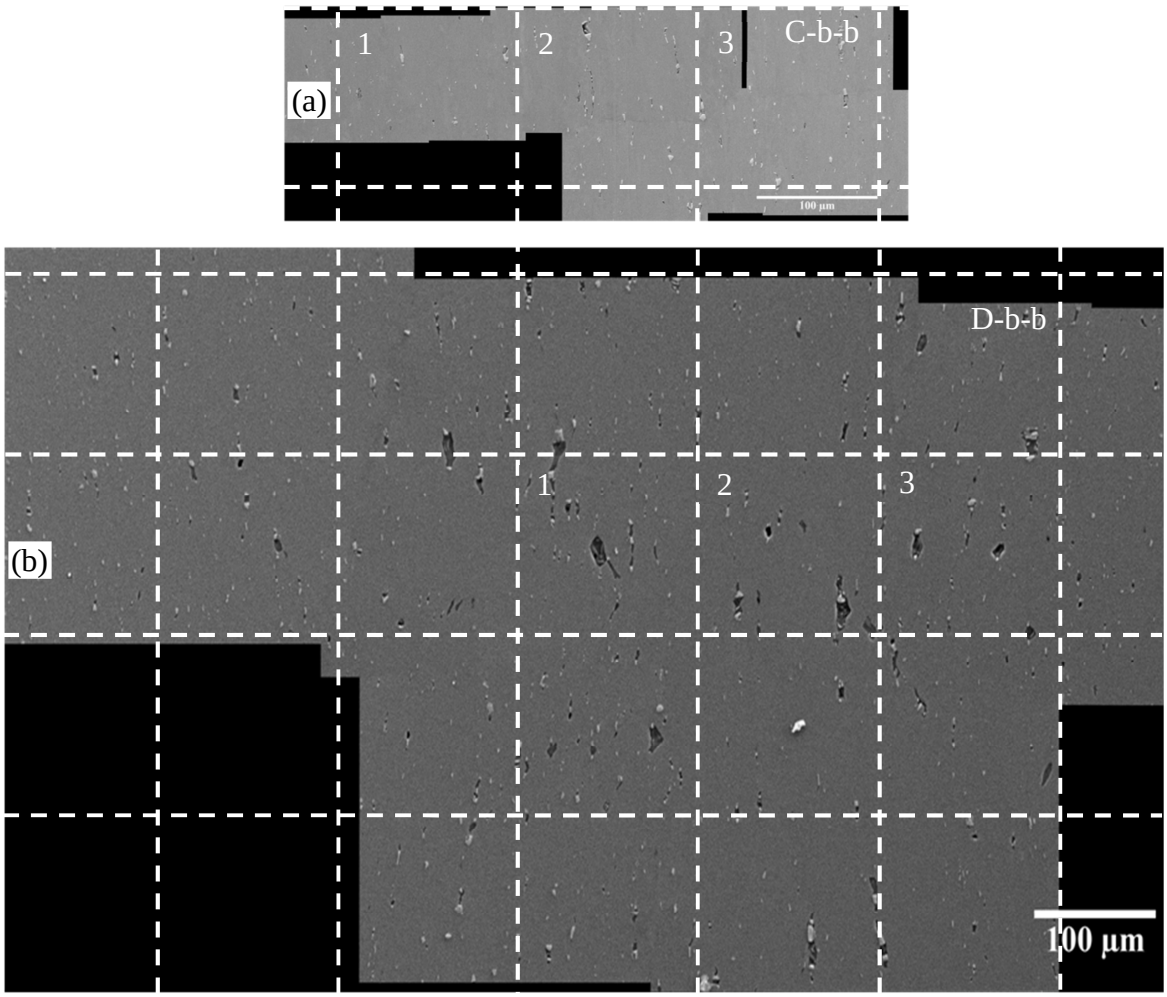

Figure 3.19. SEM micrographs of section b-b of (a) Specimen C and (b) Specimen D.

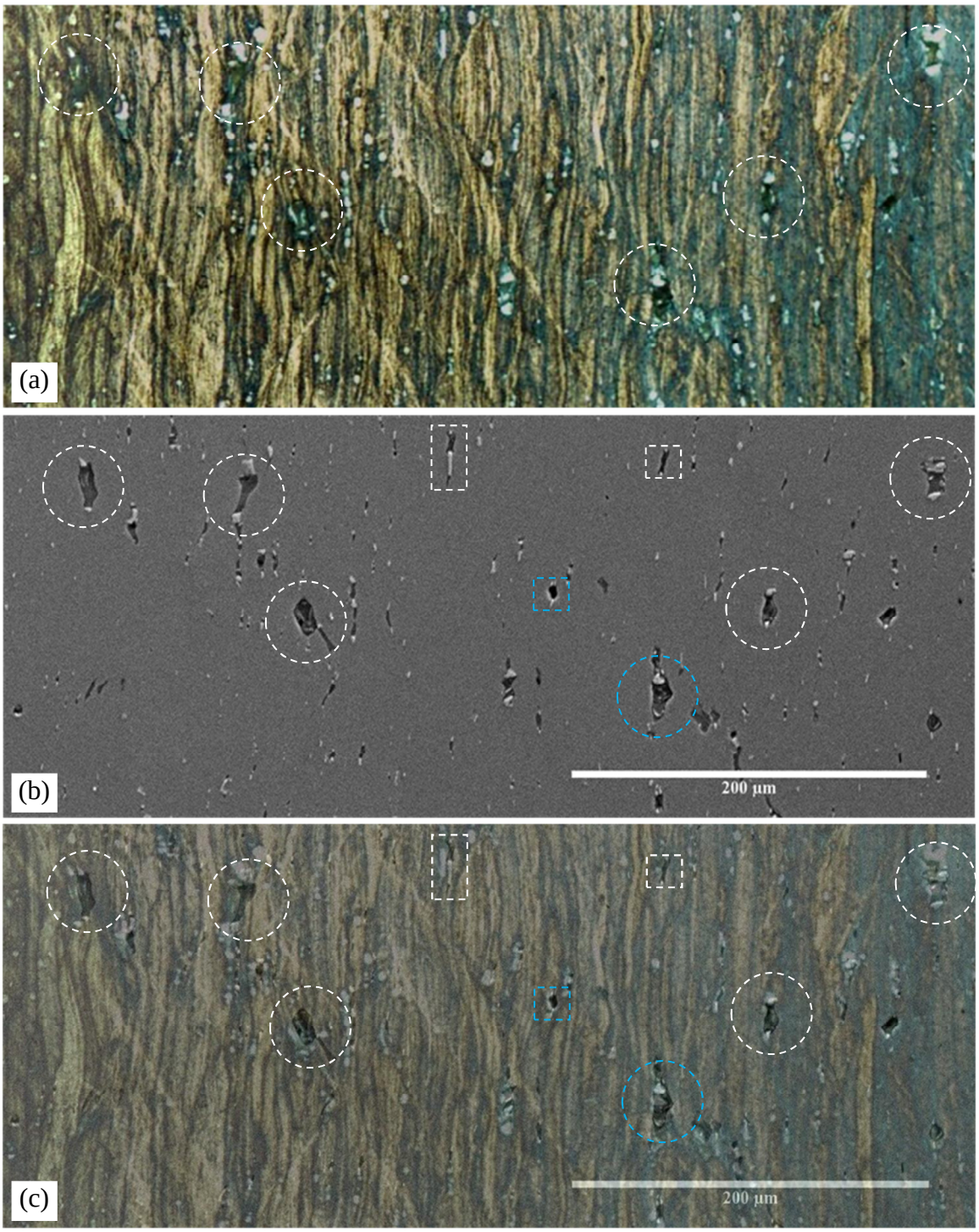

Figure 3.20. (a) Optical, (b) SEM and (c) composite overlaid image of central portion of section b-b of Specimen D distinguishing cavities from grain pull-out.

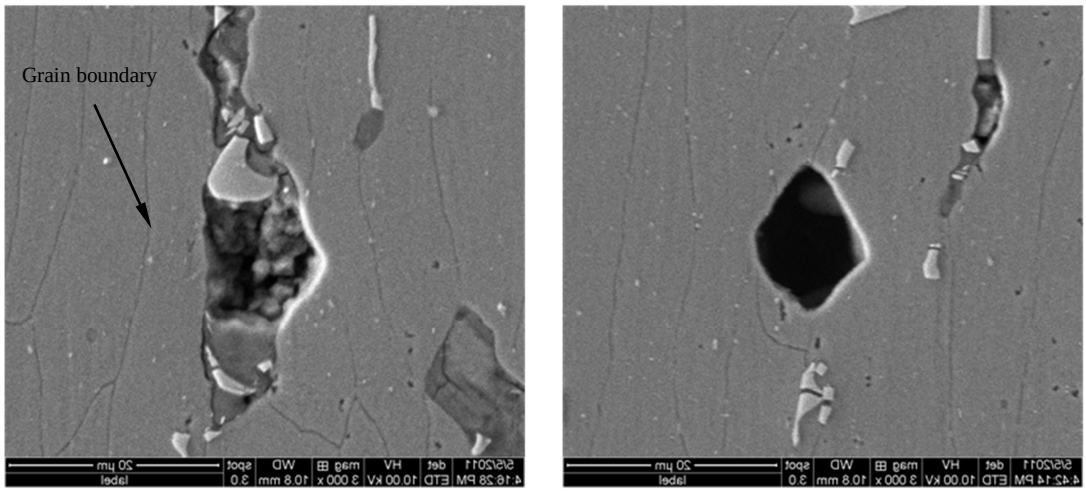

(a) Grain pullout (b) Cavity growth

Figure 3.21. Higher magnification images indicating differences between possible grain pull-out (a) and cavity growth (b).

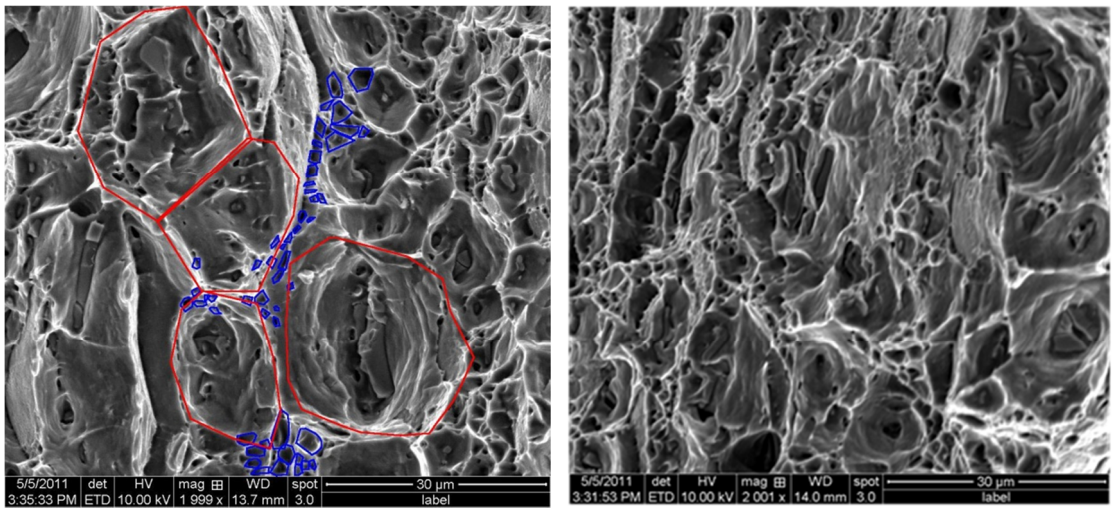

(a) (b)

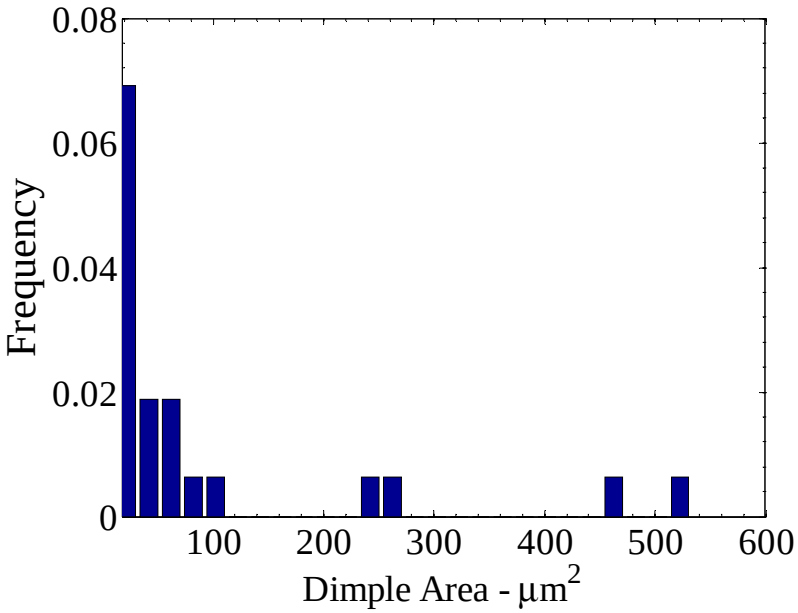

(c)

Figure 3.22. SEM fractographs at the intersection of (a) section b-b and (b) section a-a with fracture surface in Specimen E. (c) Distribution of dimple area over half the fractograph shown in (a).

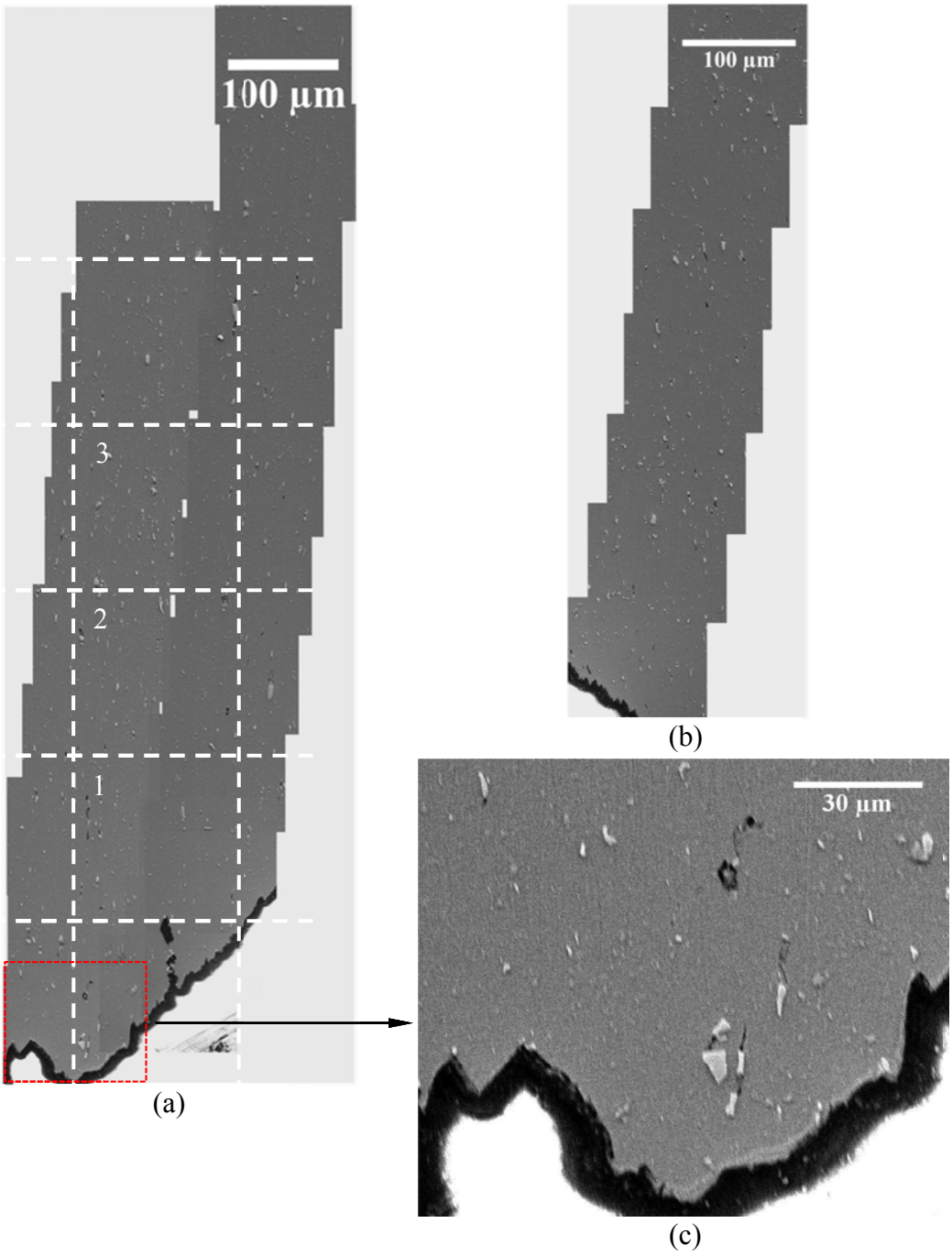

Figure 3.23. (a) and (b) show the SEM micrographs of the section b-b of Specimen E. (c) Higher magnification of red box in (a).

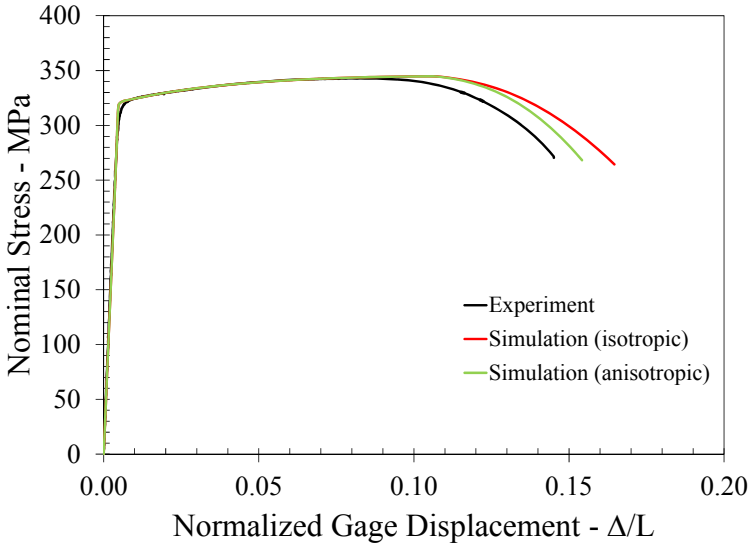

(a)

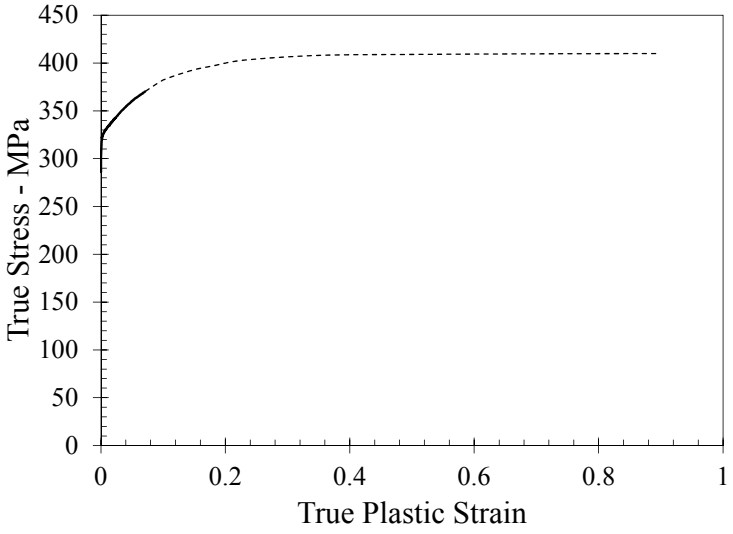

(b)

Figure 3.24. (a) Nominal stress vs. normalized gage displacement response from experiment and numerical simulations using isotropic von Mises and Hill's anisotropic quadratic yield functions. (b) True stress-true plastic strain curve from experiment (solid line) and its extension by fitting to the nominal stress vs. normalized gage displacement response from experiment (dashed line).

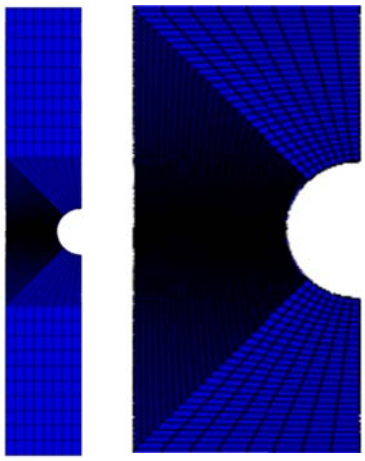

Figure 3.25. Discretized model of the flat notched specimen; due to symmetry only half the geometry was considered.

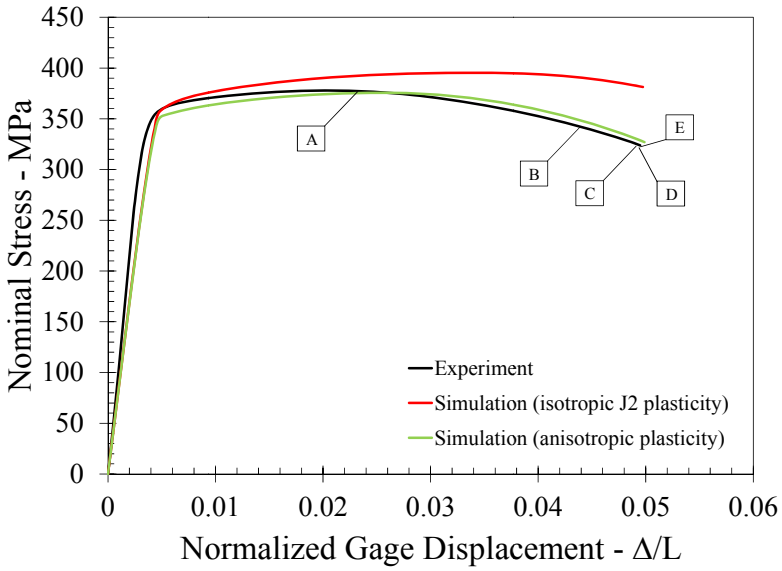

Figure 3.26. Comparisons of nominal stress (force/initial minimum cross-sectional area) vs. gage displacement (Δ) normalized by the gage length (L) (see Figure 3.4b for definition of the gage length) responses from experiment and simulation using isotropic von Mises and Hill's anisotropic quadratic yield functions.

(a)

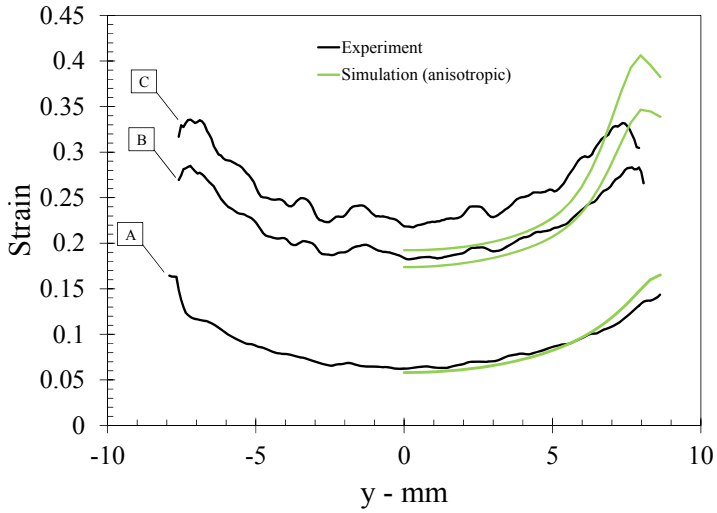

(b)

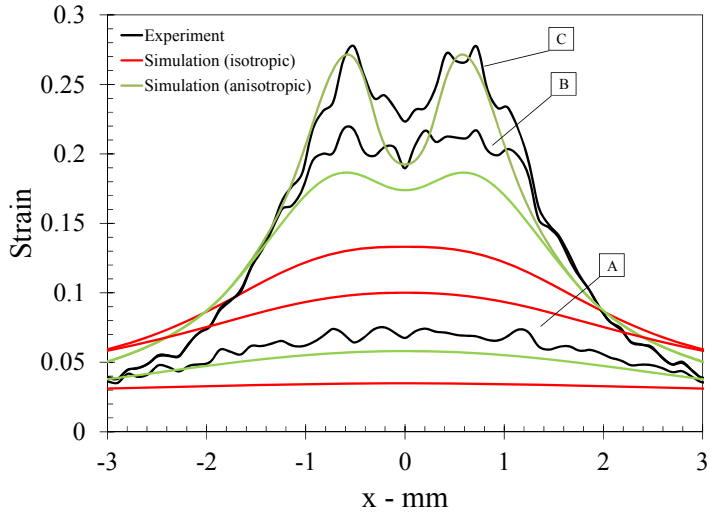

Figure 3.27. Comparisons of surface axial strain ε_x along (a) line y_1-y_2 and (b) line x_1-x_2 from experiment and numerical simulations.

(a)

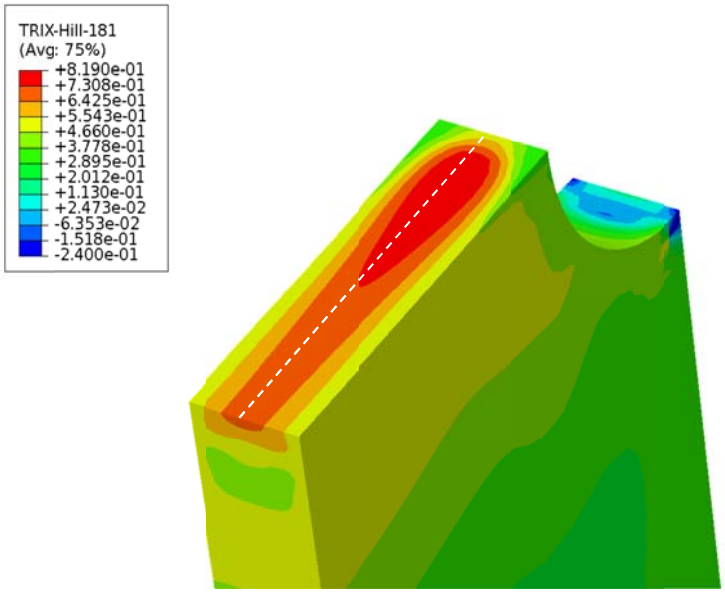

(b)

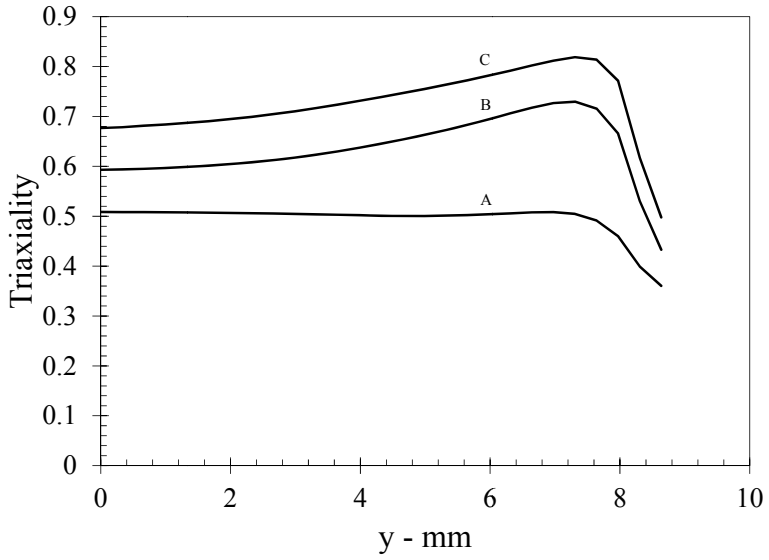

Figure 3.28. (a) Contour plot of the stress triaxiality in y-z plane at the minimum cross section (x = 0) corresponding to Specimen C. (b) Variation of the stress triaxiality at different stages of deformation (Specimens A, B and C) along the minimum cross section in the mid-plane in the thickness direction ($0 < y < y_2$, $z = 0$).

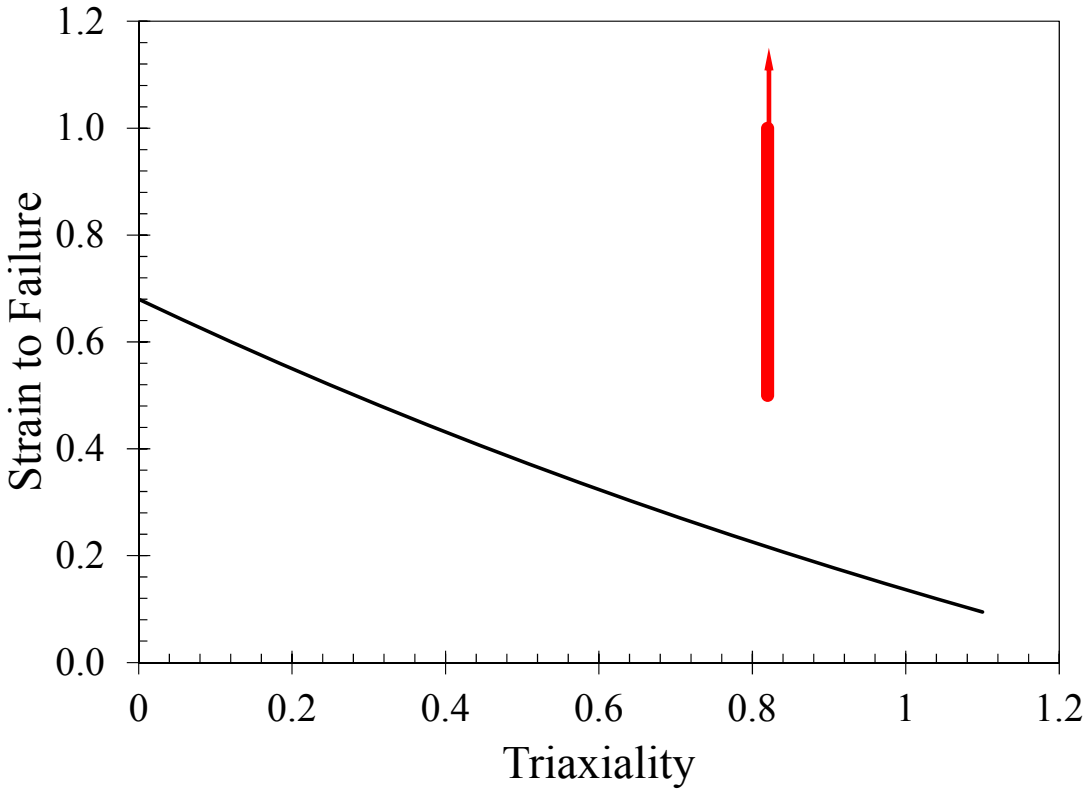

Figure 3.29. Red band representing a lowerbound fracture strain in comparison with the Johnson-Cook model (Lesuer et al. 2001) with parameters $D_1 = -0.77$, $D_2 = 1.45$, $D_3 = -0.47$ and $D_4 = 0$.

Chapter 4: Failure under Dominant Shear Loading

Models for ductile failure based on void growth and coalescence indicate no accumulation of damage under pure shear deformation where the triaxiality is zero; therefore, no localization or failure could be predicted under these loading conditions. In this Chapter, we address the issue of how failure occurs under pure shear condition with particular attention to Al 6061-T6.

Lindholm et al. (1980) developed a torsion apparatus for subjecting specimens to large strain levels at various strain rates; they examined the shear response of thin-walled tubes of annealed OFHC copper in the strain rate range of 0.009 s^{-1} to about 330 s^{-1}. The grain size in the specimen ranged from about 25 to 35 μm. Specimens strained at rates below 10 s^{-1} exhibited positive strain and strain-rate hardening; more importantly, *no localization of deformation was observed even at a true (logarithmic) strain level of about two*. At strain rates greater than 174 s^{-1}, localized shear deformation was observed at a strain level of about 1.6; failure under shear was not attained in these tests. This inability to trigger failure under pure shear in a torsion test is rather well known; however, in recent years, Bao et al. (2004), Beese et al. (2010) and others have investigated failure under low triaxiality conditions using a butterfly shaped specimen, where both the triaxiality and the Lode angle – a measure of stress state related to the third invariant of the deviatoric stress tensor – can be controlled by selecting the orientation of the specimen appropriately. Barsoum and Faleskog (2007) also examined failure under low triaxiality conditions by performing combined tension-torsion experiments in specially notched tubular specimens. In many of these experiments, the reported strain-to-failure under low triaxiality conditions is significantly lower than the strain-to-failure at higher triaxiality conditions. An example of such a trend, obtained by

Beese et al. (2010) for Al 6061-T6, is shown in Figure 4.1. The main difference between these results and the earlier experiments of Hancock and Mackenzie (1976) and Johnson and Cook (1985) is in the region of low triaxiality; while the earlier results reported a monotonic increase in the equivalent strain-to-fracture with decreasing triaxiality, the results of Beese et al. (2010) and Barsoum and Faleskog (2007) indicate a nonmonotonic dependence, with a cusp at different triaxiality levels for different materials and a drop in the strain-to-failure at lower triaxialities. While results of this type have led to the development of void growth models that incorporate shear effects in a phenomenological manner (see Nahshon and Hutchinson 2008), it is important to understand the experimental procedure used to identify such a strain-to-failure. The strain-to-failure reported in these works is obtained using a hybrid procedure: an experiment is performed under pure shear or a shear plus a normal load under combined torsion and tension or compression. The force–elongation response of the specimen is monitored to identify the onset of failure; Beese et al. (2010) use the surface strain in the gauge section, measured using the digital image correlation technique, as the strain-to-failure, while Barsoum and Faleskog (2007) use a numerical simulation of the experiment to calculate the strain at the midpoint in the specimen and use this value as the strain-to-failure. As we demonstrated in Section 3.4.2, these procedures are not quite suitable for determination of the local strains at failure; characterization of failure requires careful identification of the exact location of failure initiation and a proper definition of a gage length over which such strains are measured. Under complex loading conditions, failure is seldom within the gauge section of the specimen where observations and measurements are typically performed. In this chapter, we explore failure under shear loading through local measurements.

4.1. EXPERIMENTS

We perform experiments in an Arcan type specimen; digital image correlation, grain based measurements, and optical and scanning electron microscopy are used to monitor the strain, to identify the onset of failure, and to explore the mechanisms of deformation and failure under shear dominant loading conditions. The Arcan specimen has been used in numerous studies of composite materials (see for example, Hung and Liechti 1997, 1999). There have also been some investigations aimed at characterizing the effects of the notch angle on the shear response of the specimen (Hung and Liechti 1997, 1999); in the present work we used a 45° notch angle. The geometry of the Arcan specimen is shown in Figure 4.2a; specimens were cut from the same rolled sheet stock (2.44 mm thick) used for the tension tests described in Chapter 3, with the rolling direction oriented as indicated in Figure 4.2a. These specimens were loaded in a modified Arcan fixture shown in Figure 4.2b. The nominal stress (force/initial gage cross-sectional area) vs. normalized crosshead displacement response curves from three tests are shown in Figure 4.3; these specimens (S-1, S-2, S-3) were fabricated by electric discharge machining (EDM), resulting in a radius of curvature at the notch tip of 0.16 mm. One specimen was loaded to complete failure and the other two were unloaded after partial crack growth from the notches. Note that all specimens were preloaded in order to remove any slack in the loading fixture. The development of strain in all these tests was monitored using DIC; for the specific implementation of DIC used in this work, the displacements are measured at nodes with a spacing of 82.5 μm and strains are determined with a gage length of 165 μm; the displacement resolution is ~10 μm. The maximum principal strain contours at two selected stages, one corresponding to the onset of crack growth and the other corresponding to the last loading stage where image correlation is able to provide measurements of local strain for Specimen S-2 are shown in

Figure 4.4. Note that the specimen continues to strain beyond this point; however, local stain measures are not available. The variation of the maximum and minimum principal strains between the two notches at selected stages in the loading history is shown in Figure 4.5. From these experiments, we record the following observations:

a. The nominal shear stress vs. normalized crosshead displacement response of all specimens follows a similar trend until crack initiation (see Figure 4.3). The point of crack initiation, identified visually from the digital images, is marked in the figure; there is a small variability in the load at onset of crack growth, attributable to errors in visual identification of crack initiation and to statistical variability in the material and specimens.

b. It can be seen from Figure 4.4 that the overall deformation is concentrated between the two notches. Quantitative variation shown in Figure 4.5 suggests that maximum and minimum principal strains along the line $(x = 0)$ are nearly uniform over the mid-region of the specimen in the early stages of loading, but become significantly nonuniform with increasing global strain; in particular the notch tip regions experience significantly enhanced tensile and compressive strains. It is, of course, to be expected that cracks would nucleate and grow from the two notches; indeed, this is what is observed, significantly before the peak load is reached; nucleation of the crack was identified visually from the speckled images. With further global loading, these cracks grow across the width towards each other until they reach each other near the center of the specimen leading to the final separation.

c. Comparing the maximum and minimum principal strain variation shown in Figure 4.5, and using plastic incompressibility, it is easy to see that the strain in the

thickness direction of the specimen must be nearly zero; therefore, it can be assumed that only in-plane strains are present in the specimen until significantly large strain levels approaching failure are attained.

d. Strain measurements obtained with DIC could not resolve the strains in the vicinity of the crack tips at the onset of final failure due to the highly localized deformation in the vicinity of the propagating cracks. Even in the central portion of the specimen, as the true strain levels reach about 0.6, the speckle patterns become decorrelated and larger strain levels could not be measured accurately. The strain contour corresponding to the last analyzed image for specimens S-2 is shown in Figure 4.4; the corresponding points are marked on the nominal shear stress vs. normalized crosshead displacement response in Figure 4.3. It is seen that principal strain levels at the central region of the gage section are in the range of 0.6. These strain values are similar to the ones reported by Beese et al. (2010) as the failure strain for pure shear, but it should be emphasized that these are not estimates of the strain at which the material fails; these are merely the strains at the center of the specimen, when failure occurs in the specimen. Actual failure of the material initiates from the strain concentration at the notch tips which then generates a crack at both tips and then occurs at the central locations as these cracks propagate gradually towards the center. We will investigate the strains in these regions further in the next section through optical and SEM microscopy.

e. The deformed shape of a 2 mm long segment of the centerline $(-1 < x < 1; y = 0)$ of the specimen S-2, as determined from DIC, is shown in Figure 4.6 at different stages in the overall loading of the specimen; from these lines, it is easy to visualize the deformation of this line segment. However, image correlation is lost in the regions of large strains as a result of changes in the surface texture,

reflectivity of the specimen or due to the paint peeling off (see Stage F). Even though the maximum strain levels *measured* using DIC are only about 0.6, it is clear that these are not the maximum strain levels in the specimen; the central portion of the specimen continues to strain even after the DIC method fails to provide estimates of the strain; a simple extrapolation based on connecting the displacements of points correlated by DIC yields shear strain levels of 0.83. We will extract the actual strains in this region using grain-based strain measurements and compare the DIC based deformation with grain based measurements in the next section.

Four additional tests were performed; in these tests, the specimens were loaded in the Arcan fixture shown in Figure 4.2b at three different angles (0 , 15 and -15) giving rise to three different loading combinations – pure shear (Specimens S-4 and S-5), shear plus tension (ST) and shear plus compression (SC), respectively. These specimens were mill-cut and therefore the notch tip radius was 0.80 mm. The nominal stress vs. normalized crosshead displacement response curves from three of these tests are shown in Figure 4.7. The maximum principal strain contours at two selected stages, one corresponding to the onset of crack growth and the other corresponding to the last loading stage where image correlation is able to provide measurements of local strain for Specimens S-4, ST and SC are shown in Figure 4.8. As with the pure shear specimens, the specimen continues to strain beyond the point where DIC fails; therefore; local stain measures are not available beyond this point. The response of the specimen appears to be very similar to that observed under pure shear. In particular, the maximum and minimum principal strains along the specimen center are in the same range as the pure shear specimens. In all these tests, the maximum strains recorded by DIC are in the range of

0.6, but as noted before this does not correspond to failure of the material. In order to determine the strain at failure, one must make measurements at the level of the grains. This is addressed in the next section.

4.2. MICROSCOPIC EXAMINATION OF DEFORMATION AND DAMAGE

In an effort to determine the local strains, the Arcan specimens recovered after partial or complete failure were mounted in epoxy, polished, and etched using Weck's etchant as discussed in Section 3.1 to reveal the microstructure in x-y plane. In order to examine the evolution of deformation at the grain level, optical micrographs of the prepared sections were taken and stitched together to explore a large spatial domain. Damage nucleation and evolution in the same specimens was investigated in an SEM.

Optical micrographs of the regions near the left notch and at the center of the specimen are shown in Figures 4.9a and 4.9b, respectively. The deformation at the grain level can be identified clearly by comparing these images with the undeformed grain structure in the x-y plane in Figure 3.1. Greater detail of the rectangular regions marked as '1', '2' and '3' in these optical micrographs are shown in Figure 4.10. At locations far away, the grains remain nearly undeformed; these grains shown in Figure 4.10a can be compared to the initial grain distribution in the x-y plane shown in Figure 3.1. As indicated there, the undeformed grains in the x-y plane are nearly equiaxed, with an average grain size of about 46 μm in the x-direction and 39 μm in the y-direction. Large deformation and rotation of the grains can be readily identified from the micrographs in Figures 4.10b and 4.10c, within the regions near the notch as well as the center of the specimen. The images in Figure 4.9a and 4.9b indicate that these large deformations are confined to a very narrow region in the specimen. We now turn to quantitative estimates

of the deformation. The grain width changes are measured and interpreted in terms of the equivalent plastic strain at the grain level using the procedures indicated in Section 2.3.2; however, the deformed grain thickness was averaged over five neighboring grains, two on either size, as opposed to the eleven grains used in Chapter 3. The variation of the grain level strain across five lines, marked as Lines 1 – 5 on the micrographs of Specimen S-2 in Figures 4.9a and 4.9b is shown in Figure 4.11.

a. It is possible to reconcile the grain based measurements with the image correlation based measurements. Recall that the deformed shape of the line $(-1 < x < 1; y = 0)$ was plotted at different stages of the macroscopic loading in Figure 4.6; the last of these lines corresponds to the final stage of loading. While digital image correlation was not able to provide the displacements in the central region, displacements outside this region were indeed measured. The grain flow lines can be identified from Figure 4.9b and correlated with the DIC measurements, but only in regions far from the large gradients observed in the middle.

b. Line 5 corresponds to the centerline of the specimen $(-1 < x < 1; y = 0)$, where the crack has not yet propagated. It is clear from Figure 4.11e that very high strains, in the range of about 1.5 appear over a band of about 500 μm thickness in the central part of the specimen. These strain levels are significantly larger than the largest strains measured by digital image correlation because they arise after the point where the DIC technique fails to correlate. Outside of this band, the strains decrease sharply.

c. The highest strain levels near the crack surface and crack tip (along Lines 1 – 4) are in the range of 2. The grains can be seen to have rotated by nearly 90° and

appear to be aligned along the horizontal direction as can be seen in Figure 4.10b. The size of the band over which the strain is localized in the vicinity of the crack is smaller (~ 0.4 mm) than the band in the central portion of the specimen.

d. Specimens SC and ST were both loaded to complete failure; the micrographs of these specimens resemble closely the deformation of Specimen S-2.

While second phase particles are visible in the optical micrographs, debonding, particle fracture and/or void nucleation and growth cannot be identified easily in these images. Therefore, in order to explore the onset of failure, optical and scanning electron micrographs of Specimen S-5, which was completely broken under pure shear, were obtained. Figure 4.12a shows an optical micrograph of the central region of this broken specimen; Figure 4.12b shows a scanning electron micrograph of the same region. A composite image is made by overlaying an SEM image onto the corresponding optical image with opacity of 0.6 (see Figure 4.12c); this enables identification of the relationship between the location of the grain boundaries and the second phase particles. The following features can be observed:

a. While the second phase particles are distributed randomly in the initial microstructure, (see Figure 3.17a), these particles appear to have been aligned by the deformation, and more or less collected together in clusters at the grain boundaries!

b. A very high magnification SEM image of the crack tip region in Specimen S-4 is shown in Figure 4.13. While clustering of second phase particles is observed, the SEM images do not indicate the development of cavities near the second phase particles; the equivalent plastic strains in these regions are on the order of 2.

There are a few elongated cracks or cavities very close to the crack surface as seen in Figures 4.12b (at a distance of less than about 10 μm). These appear to be along grain boundaries.

c. A fractograph of this specimen is shown in Figure 4.14; it is difficult to obtain pristine fracture surfaces since the two mating fracture surfaces rub against each other during continued loading and destroy most of the features. However, some regions survive without such damage and the images of these regions exhibit elongated dimples on the fracture surface. These are, of course, suggestive of nucleation, growth and coalescence of voids. However, as in the case of the flat-notched tension tests, this failure process occurs in a very narrow localized plane; this can be argued by noting that the number density of the dimples on the fracture surface is a couple of orders of magnitude larger than cavities observed below the crack surface in Figure 4.12b.

d. In the middle regions of the Arcan specimen, the triaxiality is expected to be close to zero. The observations reported here imply that nucleation of damage does not occur at least until $\varepsilon = 2$. This lower bound is shown in Figure 4.15. This result is in complete contrast to the cusp-like behavior reported by Beese et al. (2010) and Barsoum and Faleskog (2007). Note that the present results are based on local measurements of strain, and microscopic identification of the onset of damage.

In summary, the deformation and failure of Al 6061-T6 under dominantly shear loading still occurs by the nucleation, growth and coalescence of voids, but the process is confined to a very small region near the fracture plane and arises only after very large plastic strains are established without generating significant damage in the material. Strain levels at the nucleation of damage were found to be greater than two.

The results shown in Figure 4.15 indicate that the strain-to-failure in the Al6061-T6, when measured at the grain level is significantly larger than strains obtained by measurements based on specimen size.

4.3. SUMMARY

Ductile fracture models based on void growth and coalescence are not able to capture the damage accumulation in low stress triaxialities. In this chapter, the mechanism of failure in Al 6061-T6 in shear dominant condition is investigated. The microstructural characterization of Al 6061-T6 was given in Section 3.1. Arcan type specimens under pure shear, and superposed tension and compression were interrupted prior to complete failure, and metallographically prepared for microstructural observations. Digital image correlation was used to obtain strain evolution at macro-scale. The grain-based strains through direct measurements of the change in grain size were estimated to obtain the deformation at micro-scale. Scanning electron microscopy was employed to track the evolution of damage in the microstructure. It was observed that cracks initiate at the notches at some point during the deformation; these cracks propagate with further deformation until they reach each other at the center of the specimen resulting in the final separation of the specimen. Strain levels in the range of 1.5 were measured in the center portion of an interrupted specimen (partially fractured). Quite strikingly, no damage was observed in this region of high strain. Strain levels in the range of 2 was observed near the crack surface and crack tip; there are a few elongated cracks or cavities very close to the crack surface at a distance of less than about 10 μm. the fracture surfaces exhibit elongated dimples characteristic of void nucleation, growth and coalescence; however, as in the case of the flat-notched tension tests, this failure

process occurs in a very narrow localized plane. Comparison with some strain-to-failure-models such as the Johnson-Cook model and modified Mohr Coulomb model shows that the strain values measured at grain level are significantly larger. The discrepancy between these models and our experimental results is attributed to the selection of an inappropriately large gage length over which the strain is measured in conventional tests; in contrast, the present experimental results use a gage-length that is based on the characteristic microstructural length – the grain size.

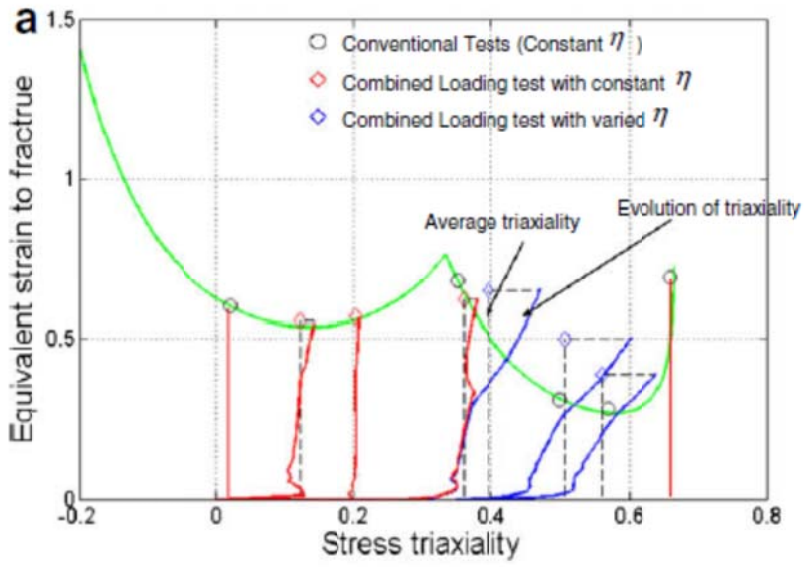

Figure 4.1. Modified Mohr Coulomb fracture criterion proposed by Beese et al. (2010).

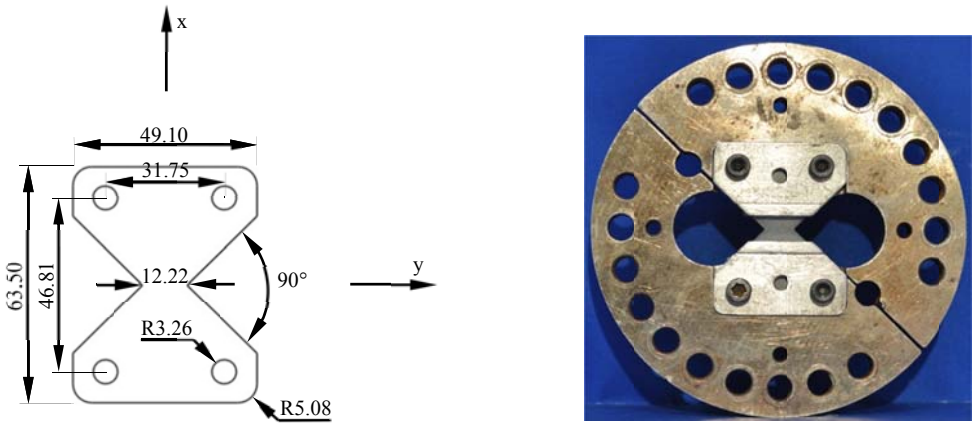

(a) (b)

Figure 4.2. (a) Geometry of the Arcan specimen (all dimensions are in mm). Rolling direction is along the x-direction. (b) Geometry of the fixture used in Arcan tests.

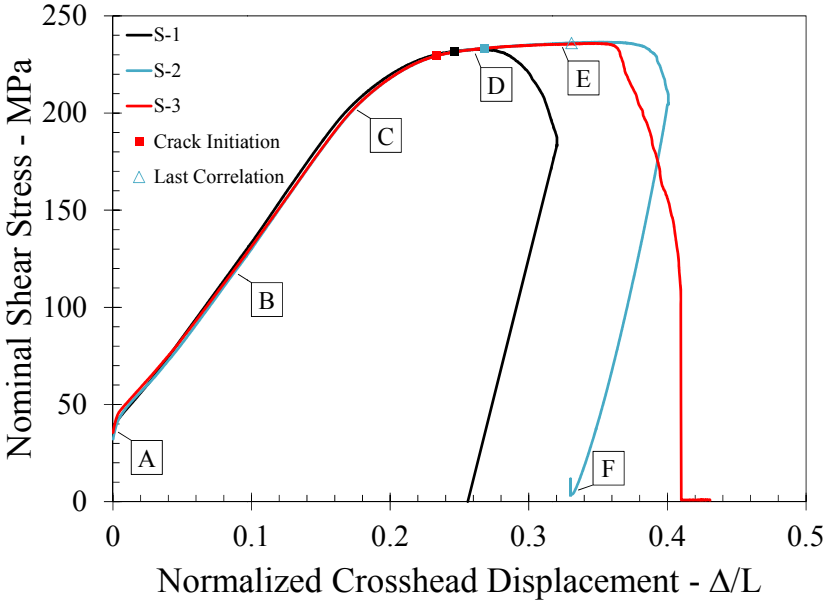

Figure 4.3. Nominal shear stress (force/initial gage cross-sectional area) vs. crosshead displacement (Δ) normalized by the gage length (L=12.22 mm) (see Figure 4.2a) response of Specimens S-1, S-2 and S-3. Square symbols mark the initiation of the crack at the notch tips for the three specimens and triangle symbol marks the last image of Specimen S-2 that DIC was able to correlate.

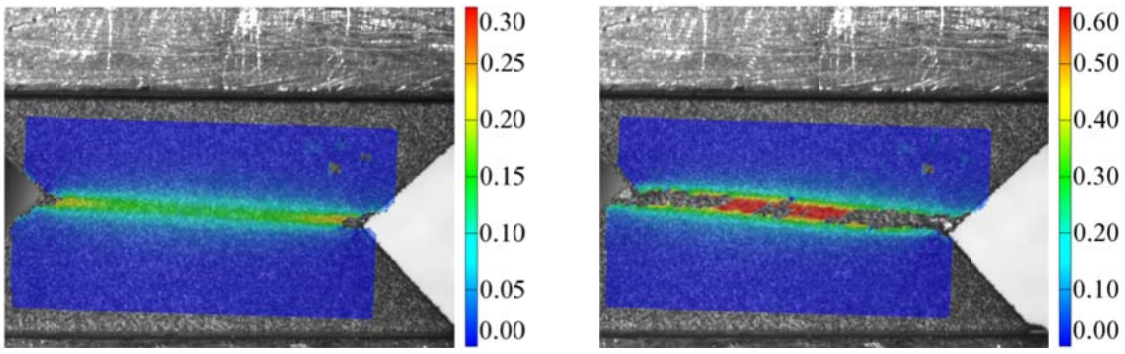

(a) (b)

Figure 4.4. Contour plots of the maximum principal strain (a) corresponding to crack initiation at the notch tips and (b) at the last stage where digital image correlation still provides an evaluation of strains.

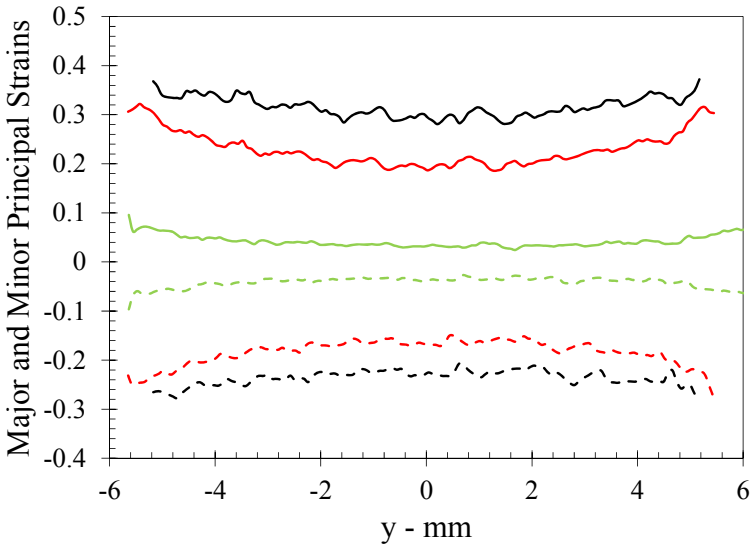

Figure 4.5. Variation of the maximum and minimum principal strains between the two notches at normalized crosshead displacements 0.199, 0.255 and 0.272.

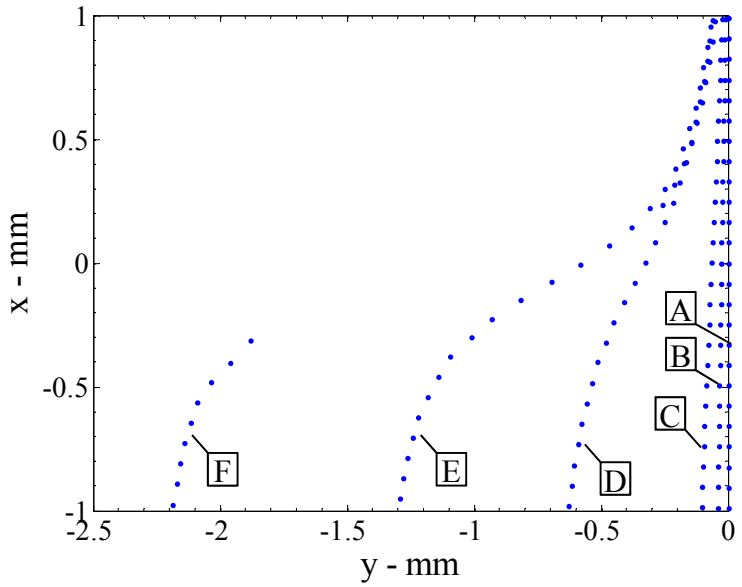

Figure 4.6. Deformed shape of a 2 mm long segment of the centerline ($-1 < x < 1$; $y = 0$) of the specimen S-2, as determined from DIC at different stages in the overall loading of the specimen (see Figure 4.3).

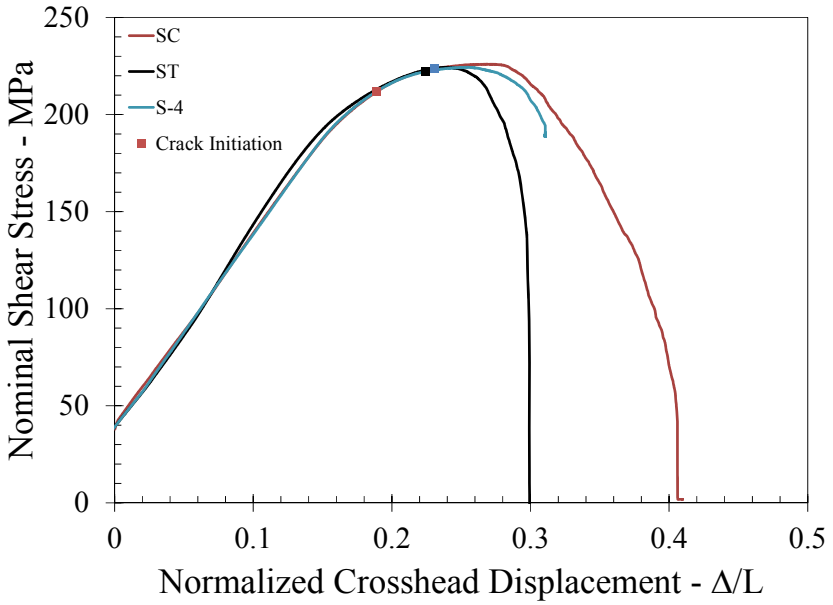

Figure 4.7. Nominal shear stress (force/initial gage cross-sectional area) vs. crosshead displacement (Δ) normalized by the gage length (L=12.22 mm) (see Figure 4.2) response of Specimens SC, ST and S-4. Square symbols mark the initiation of the crack at the notch tips for each specimen.

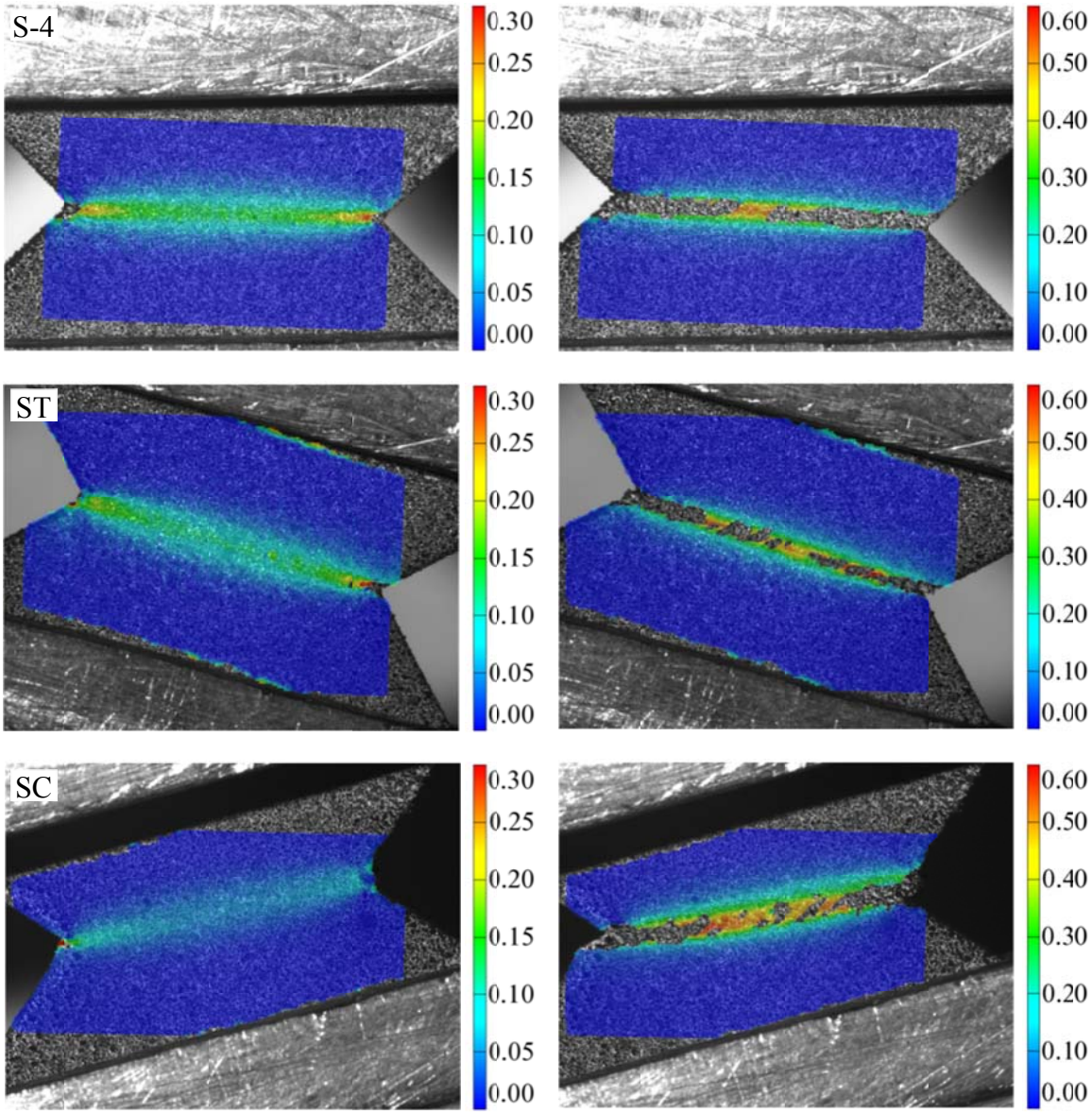

Figure 4.8. Contour plots of the principal strain in Specimens S-4, ST and SC.

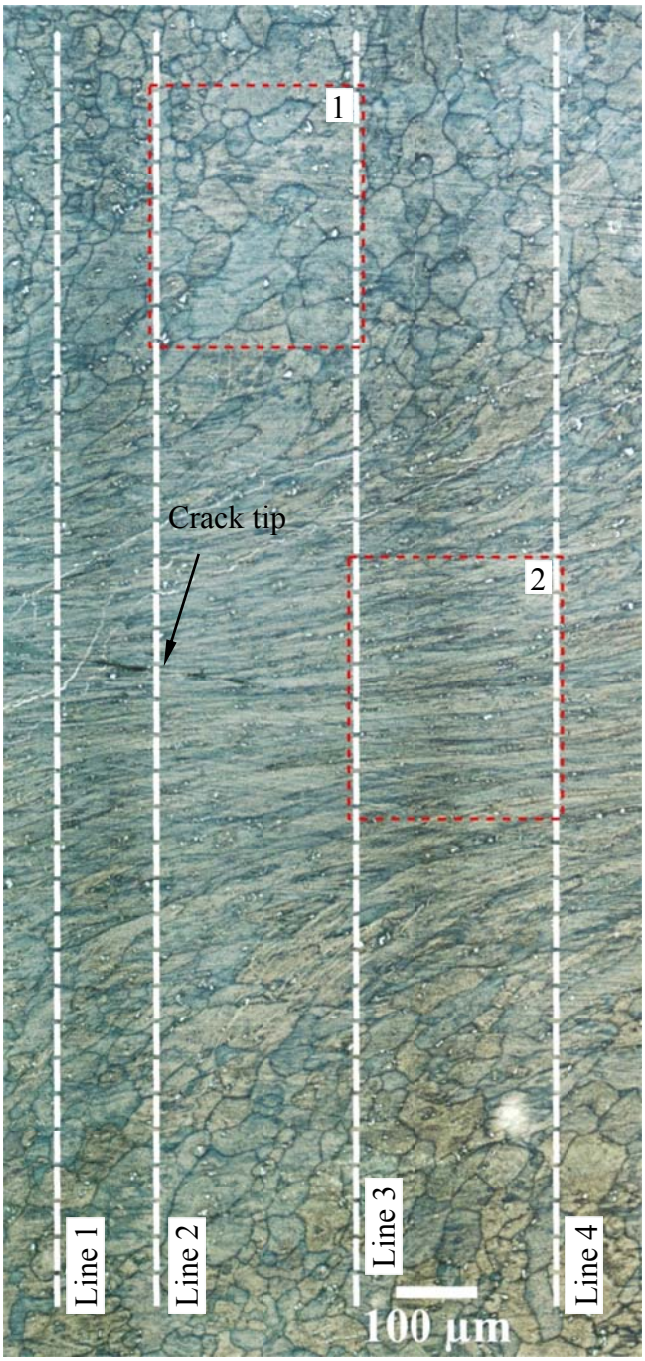

Figure 4.9a. Micrograph of the region near the notch of Specimen S-2.

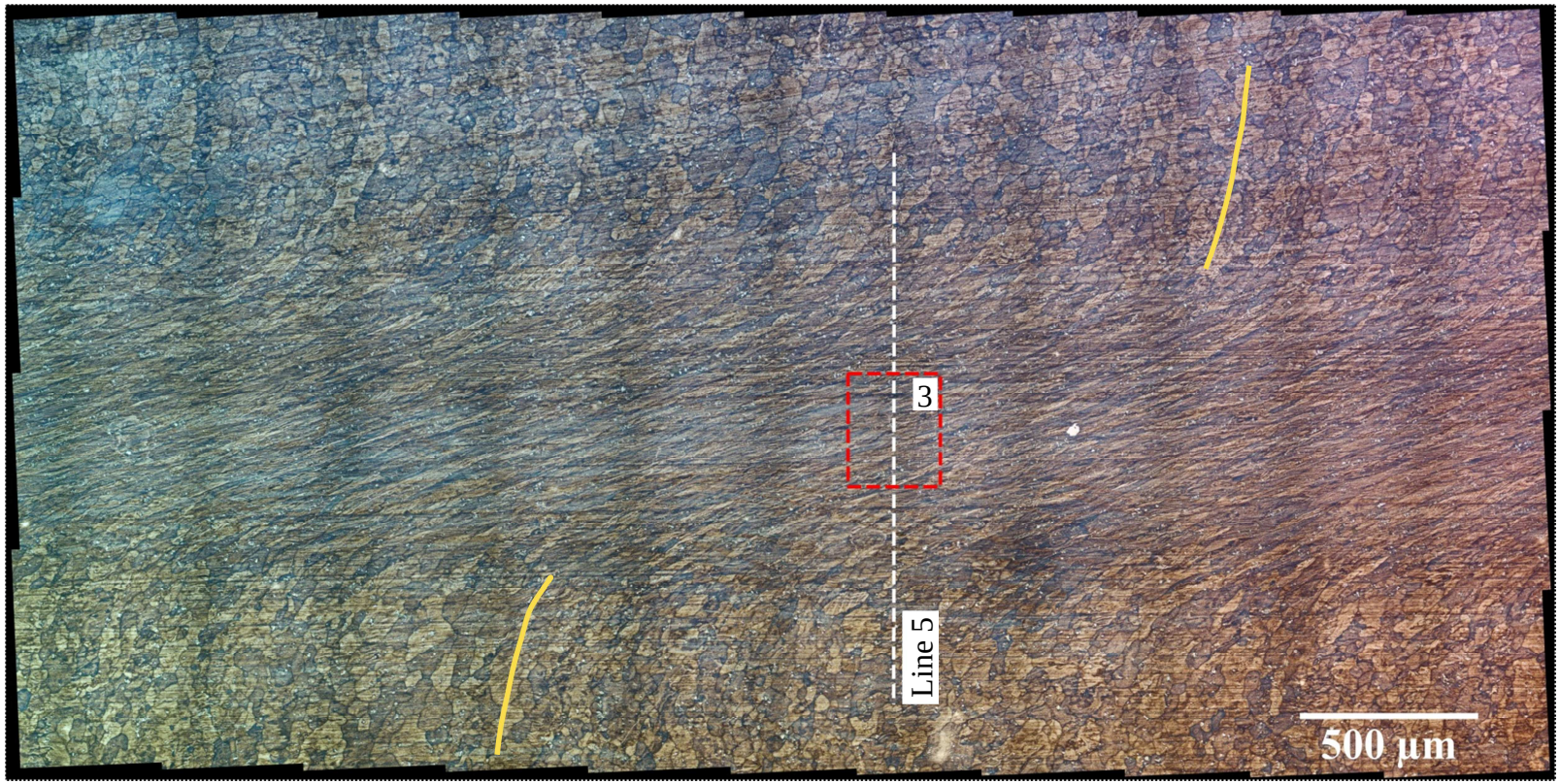

Figure 4.9b. Micrograph of the region near the center of Specimen S-2.

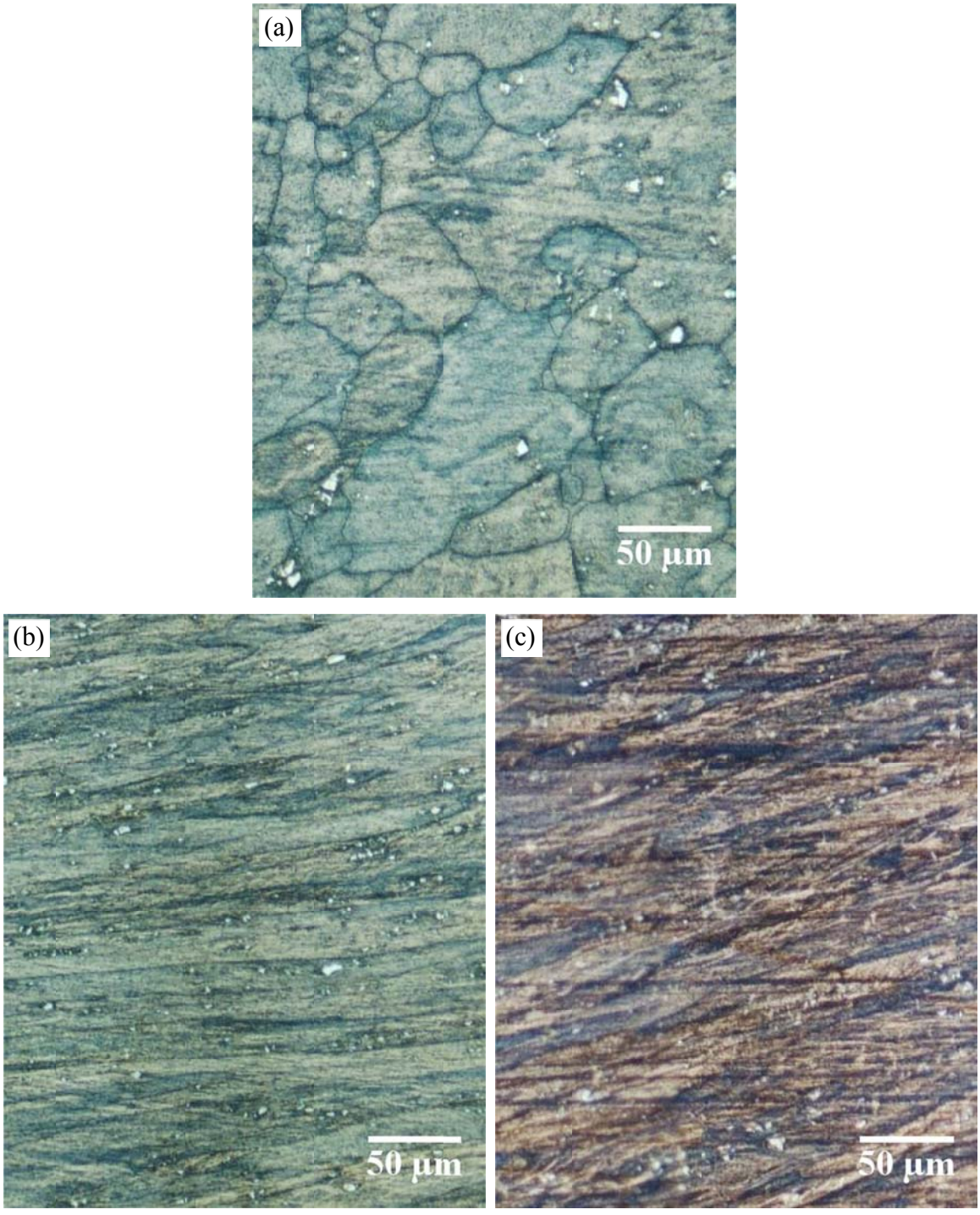

Figure 4.10. High magnification images of (a) region 1, (b) region 2 and (c) region 3 marked in Figures 4.9a,b.

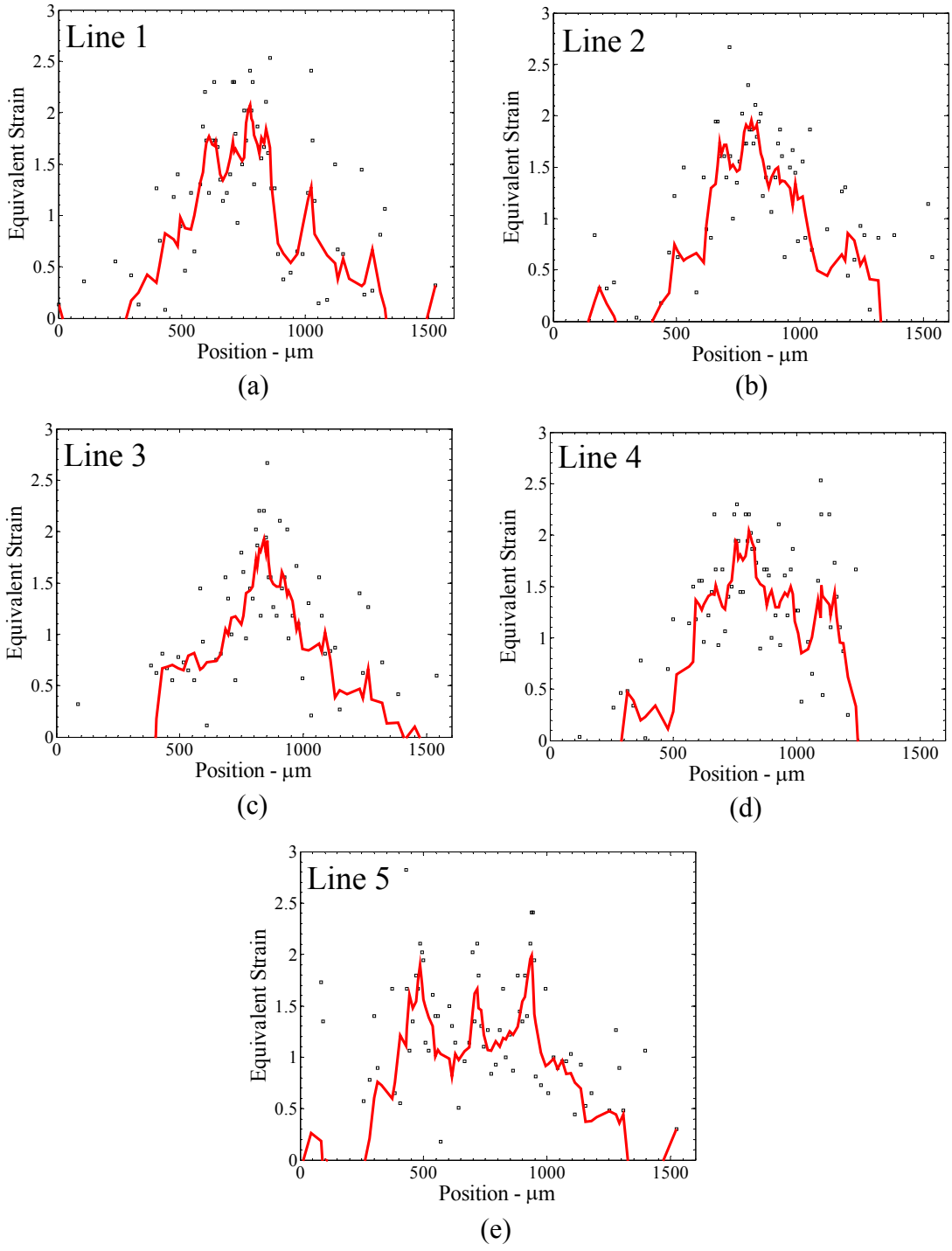

Figure 4.11. Variation of the grain-based equivalent strain across Lines 1 – 5 marked on the Figure 4.9a,b.

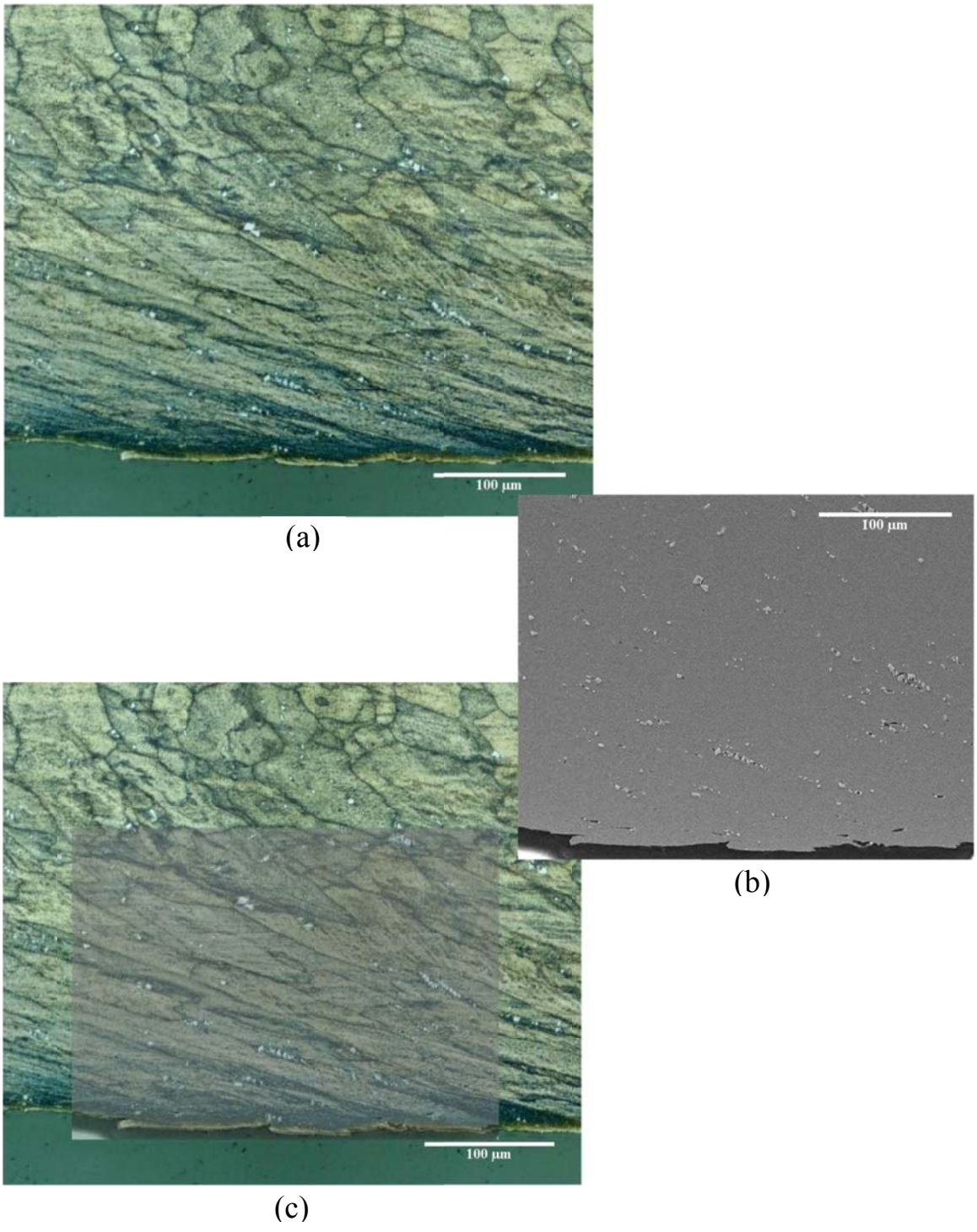

Figure 4.12. (a) Optical micrograph and (b) SEM micrograph of the central region of Specimen S-5, and (c) composite overlay of (b) onto (a) with opacity of 0.6.

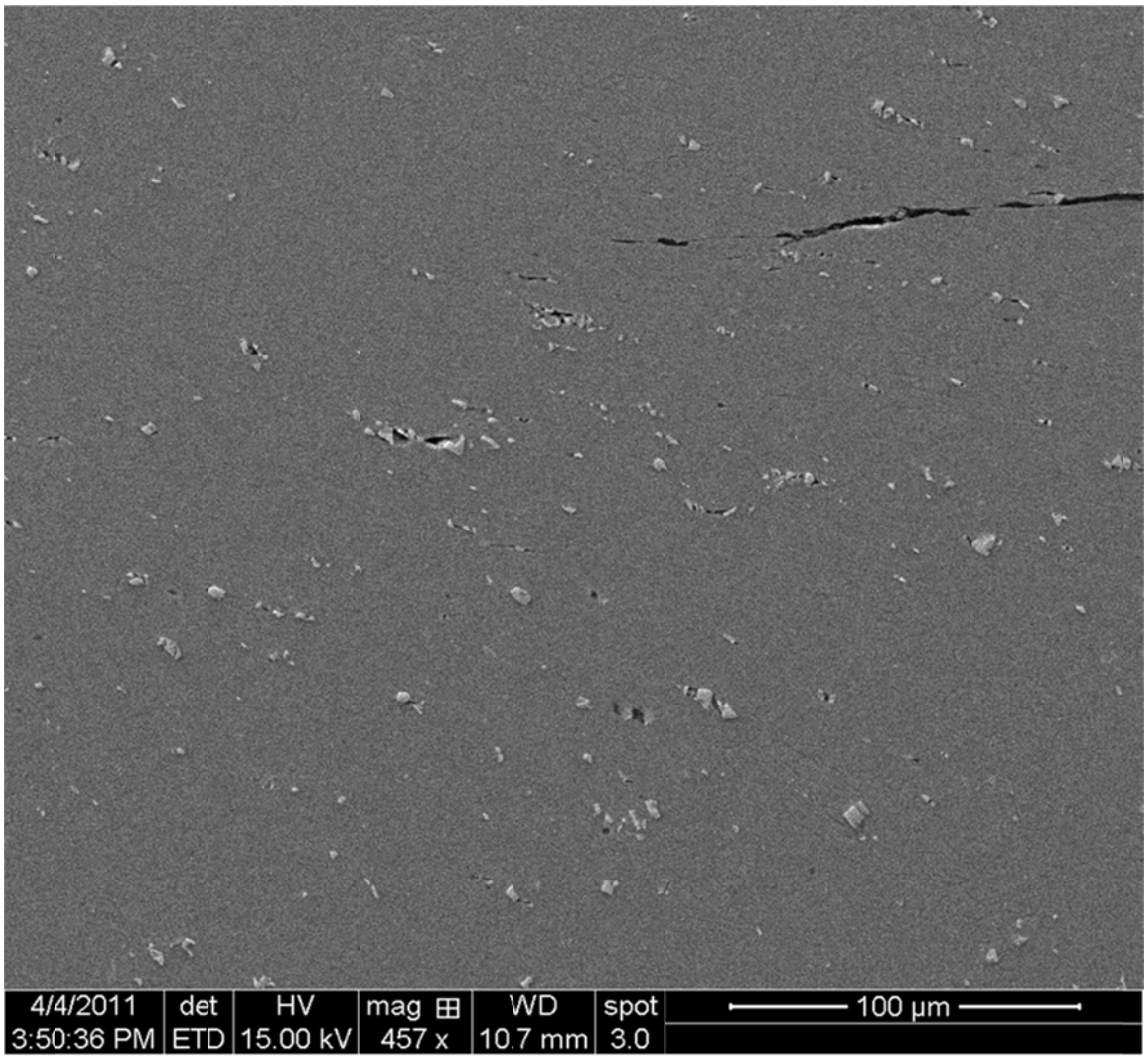

Figure 4.13. Very high magnification SEM image of the crack tip region in Specimen S-4.

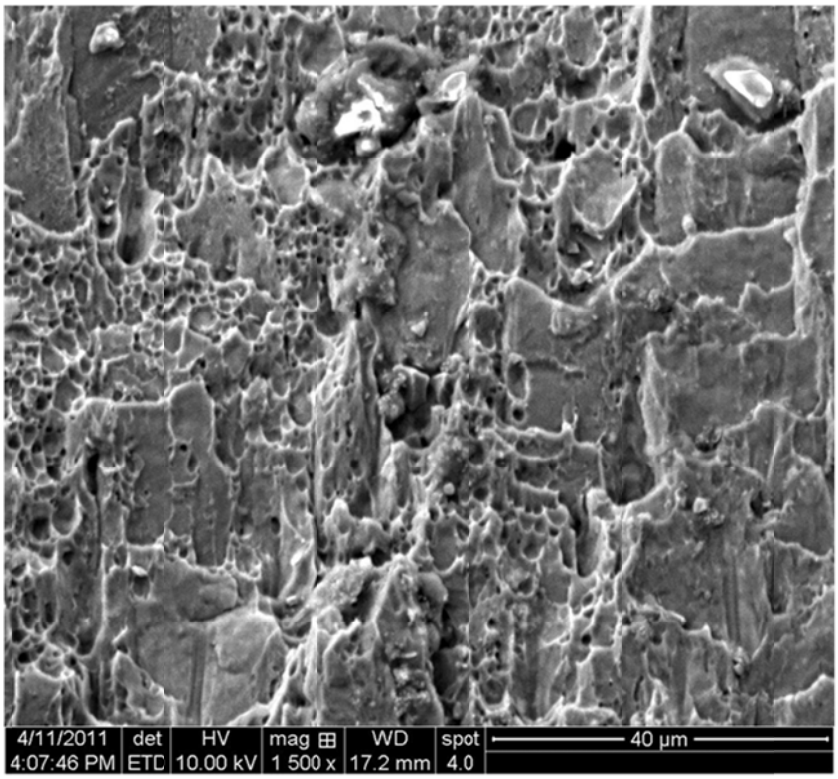

Figure 4.14. Fractograph of Specimen S-5.

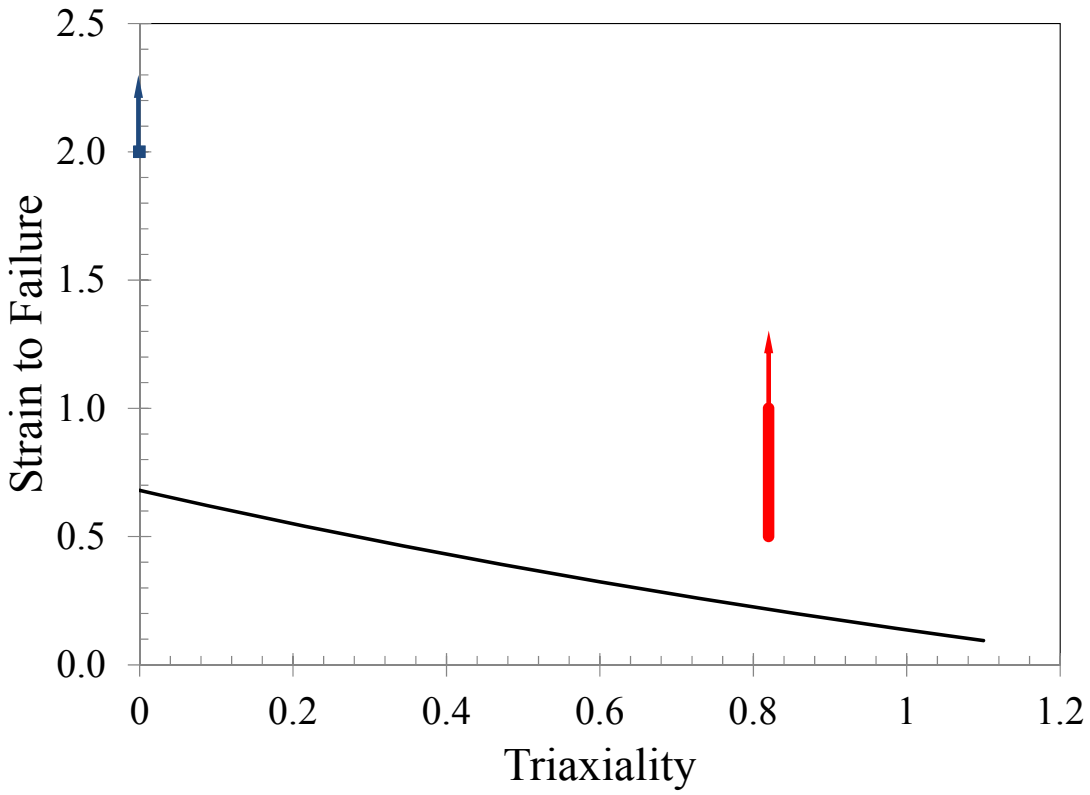

Figure 4.15. Blue square and red band representing lowerbound fracture strains in comparison with the Johnson-Cook model (Lesuer et al. 2001) with parameters $D_1 = -0.77$, $D_2 = 1.45$, $D_3 = -0.47$ and $D_4 = 0$.

Chapter 5: Deformation and Failure in Nodular Cast Iron

In this chapter, we investigate the process of deformation and evolution of failure in initially porous materials. This choice of material was made with the goal of decoupling the process of void growth from the process of void nucleation, and thus avoiding the difficulty of modeling the complex nucleation process; this allows us to monitor the microstructural evolution of the pre-existing voids. For this purpose, three different materials – sintered iron, spheroidized sintered iron and nodular cast iron – were considered. However, the sintered iron specimens could not sustain strains over 2%; spheroidized sintered iron specimens strained up to 16%; however, the uncontrolled heat treatment produced a highly nonhomogeneous microstructure where no meaningful correlation could be made between specimens interrupted at different stages of the deformation. Therefore, sintered and spheroidized sintered iron specimens were not considered further in this thesis.

5.1. MATERIAL

Ductile cast iron or nodular cast iron (NCI) is a type of cast iron where the graphite takes a nearly spherical shape (ASM 2002). Magnesium particles are usually added as an inoculant in the casting process to provide nuclei at which the graphite nodules can grow. The cooling time during the manufacturing process plays a very important role in determining the microstructure and the mechanical properties of the cast iron. Therefore, the microstructure of different sections of the cast material varies in the size and count of nodules, and hence in the mechanical behavior. In order to ensure consistency in the material used in the experiments, all the specimens were cut from the

central portion of the blank. Metallographical observations and mechanical testing support the consistency in the material microstructure and material properties.

The nodular cast iron used in this study is an ASTM A536 grade 65-45-12[4] ductile cast iron with a ferritic matrix that contains about 5-25% pearlite. The chemical composition of the cast iron, as provided by the supplier, is listed in Table 5.1.

Metallographic samples were prepared by sectioning the tensile specimens in the longitudinal direction, mounting in epoxy, and polishing following the standard procedures down to the final polishing with 0.05 μm silica particles in a colloidal suspension. Special care was exercised so as to not cause to flow the material over the pores during the polishing process thereby enabling accurate measurements of the porosity. In order to remove the polishing compounds from the surface, the samples were cleaned in an ultrasonic cleaner. The samples were finally etched to reveal the grain structure. Thirty images were taken of each sample in a Nikon Eclipse microscope at 200X magnification and then stitched together to a size of 1.40 by 4.00 mm area; these images were then used to obtain quantitative measures of grain size, void distribution and other microstructural features. The unetched microstructure and etched microstructure at a higher magnification of the nodular cast iron are shown in Figures 5.1a and 5.1b, respectively. As can be seen in the micrograph, in this hypoeutectic alloy, the graphite nodules are surrounded by grains of ferrite. The dark phase identifiable outside the ferritic domains is pearlite; the alternating layers of ferrite and cementite are extremely fine and not resolved in this micrograph. In order to obtain a quantitative measurement of the microstructural features, an image analysis software (ImageJ) was used. It should be emphasized that even though extra caution was taken in polishing the specimens to

[4] The grade code number indicates the tensile strength (ksi), yield strength (ksi) and percent elongation at failure, respectively.

protect the surface from polishing artifacts, due to the nature of the polishing process there exists a number of features that resemble graphite nodules in the micrographs that should be excluded in order to obtain as accurate results as possible. Observations of the microstructure at higher magnification showed that most of these types of impurities are of size smaller than 47 μm^2; therefore in all the microstructural analysis performed, dark patches smaller than 47 μm^2 have been filtered out. A shape factor $F = 4\pi A / p^2$ where A and p are the area and perimeter of the nodules, respectively, is defined to characterize the shape variation of the graphite nodules. A value of $F = 1$ corresponds to a perfectly round particle and the shape becomes more irregular with decreasing F. The average grain size of ferrite and the diameter of graphite nodules were found to be about 26 ± 9 and 27 ± 25 μm, respectively; the mean spacing of the nodules is about 95 ± 60 μm.

It has been documented in the literature (Dong et al. 1997; Steglich and Brocks 1997) that the weak interface between the graphite nodules and the ferritic matrix triggers decohesion of the nodules at very low plastic strains; however, there have also been investigations that showed debonding occurring continuously over the course of deformation (Guillemer-Neel et al. 2000). We assume that the initial distribution of graphite nodules is equivalent to the initial distribution of voids.

In order to obtain quantitative measures of the microstructure, a MATLAB code was implemented to construct a Voronoi tessellation diagram on the stitched optical images from which the local porosities were measured (Figure 5.2). Two measures of porosity are evaluated: the *local porosity* is calculated by dividing the pore area denoted by A_p by the area of the assigned cell denoted by A_v. The *bulk porosity* is calculated by the ratio of total area of nodules to the area of the representative volume. Although the stereological characteristics of the pores are not included in the calculations, as pointed out by Argon and Im (1975), the frequency distribution of a pore size measured on a

sectioned plane is a good approximation of the density in a volume equal to $\sqrt{2}$ times the area in sectioned plane. However, the results reported here are not corrected for this approximation.

Identification of the length scale of a representative volume element (RVE) plays a big role in the determination of effective properties of the material. In order to characterize the effect of the length scale on the mean as well as the standard deviation of the local porosity, sub-regions of sequentially reduced dimensions (1/4, 1/9, 1/16, 1/25, 1/36, 1/49 and 1/64 of the area of the largest region) are analyzed (see Figure 5.3). The variation of the mean local porosity A_p/A_v calculated from Voronoi tessellation procedure as a function of the RVE size is plotted in Figure 5.4a. The variation of the bulk porosity calculated as the ratio of the total area of the nodules in a sub-region to the area of the sub-region is also included in the plot for comparison. Figure 5.4b shows the variation of the standard deviation of the local porosity with the RVE size. From these results, it appears that above an RVE size of about 1200 μm, the mean local porosity becomes less sensitive to the size of the RVE. The change in standard deviation also seems to decrease at a length scale about 1200 μm. Based on the above observations a proper size of the RVE for the material at hand would be 1200 μm; note that this is an extremely 'large' size in comparison to overall specimen dimensions typically used in experiments on NCI. In the present work, the specimen thickness contains only two RVEs. This estimate of the RVE is entirely from a point of view of the geometry of the porosity; it does not indicate anything regarding whether estimates of effective field quantities homogenized with respect to this RVE could represent actual material response; this requires further examination of the deformation and stress fields. However, all the microstructural analyses described in the following sections were performed on an area of 1400×4000 μm^2.

We examine the evolution of void size with deformation through interrupted uniaxial and flat notched tension tests. While the macroscopic deformation and stress in uniaxial tension test are uniform throughout the gage length (before any plastic instabilities in the form of diffuse or localized necking) with stress triaxiality of 1/3, the deformation and stress in the flat notched specimens are non-homogeneous with a nearly constant stress triaxiality of about 0.577 for the particular notch geometry considered in this work. The flat notched tests are particularly useful to assess the effect of stress triaxiality on evolution of void nucleation and growth in nodular cast irons.

5.2. UNIAXIAL TENSION TEST

Uniaxial tension tests were performed on standard dog-bone type specimens in order to characterize the elastic-plastic behavior of the materials. The geometry of the specimens used in the experiments is shown in Figure 3.2. Dogbone specimens of 2.54 mm thickness were cut in the longitudinal direction from a blank of 38.1×38.1×160.0 mm dimensions. The tensile tests were run on an Instron 4482 universal testing machine at a crosshead speed of 0.254 mm/min, resulting in quasi-static loading at a strain rate of 10^{-4} s^{-1}; three specimens were tested at a strain rate of 10^{-4} s^{-1}. A gage length of 20 mm was specified over which the strain and displacement measurements were made using DIC. Specimen A corresponds to an unstrained sample for characterizing the initial microstructure. Specimens B and C were unloaded before the final failure at different levels of homogeneous straining ($\varepsilon_B = 0.056$, $\varepsilon_C = 0.094$) in order to quantify the microstructural evolution. The final specimen (D) broke at overall true strain of $\varepsilon_D = 0.145$. The true stress-true strain responses from the tension tests are shown in Figure 5.5. The Young's modulus and Poisson's ratio were found to be $E = 170$ GPa and

$\nu = 0.3$, respectively. As can be realized from Figure 5.5 the load increases monotonically until abrupt failure. Thus this specimen does not exhibit plastic localization in the form of either diffuse or localized necking. A power law relation was used to fit the true stress-true strain curve as follows:

$$\sigma^{\mathrm{NCI}} = \sigma_0^{\mathrm{NCI}}(1+\beta\varepsilon^p)^n \tag{5.1}$$

where $\sigma_0^{\mathrm{NCI}} = 227.5$ MPa is the initial yield strength, $n = 0.17$ is the hardening exponent, ε^p is the plastic strain and $\beta = 2439$. The Considère point corresponding to this material is at $\varepsilon_n = 0.17$; hence the absence of diffuse necking suggests that fracture or failure by link up of microscopic damage must have preceded the onset of diffuse necking.

The optical micrographs in Figure 5.6 show the evolution of the porosity of Specimens B, C and D corresponding to different strain levels in comparison to the initial microstructure. The evolution of the microstructure with deformation is evident from the micrographs in Figure 5.6 where the voids appear to grow with a subtle elongation in the direction parallel to applied tensile loading. Of course, the spatial distribution of the nodules does not change during the deformation.

The evolution of the distribution of local porosity, estimated using the Voronoi tessellation procedure discussed above, is plotted in Figure 5.7a; the evolution of the distribution of void area is shown in Figure 5.7b. While there does not appear to be a noticeable change in the statistical distribution of local porosity in the different specimens, the average porosity has increased from 0.10 to 0.13. However, in view of the standard deviation in the local porosity shown in Figure 5.4b, the observed increase in average porosity may not be statistically significant. This is not surprising in light of the fact that the RVE is quite large. A slight decrease in the average shape factor from

$F = 0.685$ for Specimen A to $F = 0.670$ for Specimen D can be seen as a subtle change in the shape of the voids which appear visibly to be elongated in the loading direction (see Figure 5.6). This indicates the change in void shape in addition to volumetric enlargement during the deformation of the microstructure.

5.3. FLAT NOTCHED TENSION TEST

In order to extend the strain range over which the evolution of porosity is examined, flat-notched specimens cut longitudinally in strips of 2.54 mm thickness from the center portion of the cast iron blank were used (Figure 5.8a). Two semi-circular cut-outs are introduced to increase the stress triaxiality in the center portion of the minimum cross section. This modification allows us to promote and evaluate the void growth process in a different stress state. Two tests were run with Specimen B straining all the way to failure and Specimen A interrupted slightly before the final failure so that the evolution of the void growth can be correlated to the macroscopic strain fields measured by DIC. The nominal stress (force/initial minimum cross-sectional area) vs. normalized gage displacement (over a gage length of 20 mm) responses for both tests are shown in Figure 5.8b. Just as in the uniaxial tension tests, these curves continue to exhibit a positive slope until the onset of final failure; no instability in the form of necking or shear bands was observed in the flat-notched specimens. Figures 5.8c and 5.8d show the contour plots of the axial and transverse strains superimposed onto the speckled surface of the specimen; these figures correspond to Specimen A. The axial strain is seen to be concentrated near the notch regions, reaching values as high as 0.165. The transverse strain is close to zero in the middle portion of the specimen width indicating a nearly plane-strain state and attains a maximum value near the notch tip region that is expected

to be in a state of uniaxial stress. It can be seen from Figure 5.8e that the axial strain on the surface of the specimen across the minimum cross section varies from 0.037 at the mid-point to 0.165 at the notch tip; onset of final failure occurs rather abruptly at the notch tip. A complete numerical analysis of the problem is required to obtain the variation of the stress field in the specimen; however, it can be noted that due to the geometrical constraint, the region close to the root of the notch will be in a stress state close to uniaxial tension whereas the middle part is in a plain strain state. Therefore a gradual increase in stress triaxiality from $1/3$ at the notch tip to $1/\sqrt{3}$ at the minimum cross section is expected.

Specimen A was sectioned along lines a-a, b-b, and c-c indicated in Figure 5.8a to reveal the x-z planes; these sections were polished, and observed in a microscope to identify the changes in the voids; these micrographs are shown in Figure 5.9, where surface strain corresponding to each image is also identified. The distributions of local porosity and void area were obtained as discussed earlier and are plotted in Figure 5.10. As in the uniaxial tension tests, these plots indicate that there is very little change in the void size distribution, but a slight decrease in the shape factor indicating ovalization of the voids. A small increase in the overall porosity that varies from about 0.10 at section a-a to about 0.13 at section c-c is observed as the strain varies from 0.037 to 0.165 but once again, this is not statistically significant. Interestingly, sections a-a and b-b do not indicate significant void growth even though the stress triaxiality is higher here than that at the notch; it should be noted, however, that the strain levels are quite low in these regions.

Figure 5.11a shows scanning electron micrographs of the fracture surface of Specimen B. The fracture surface consists of three main features: first, equiaxed dimples are observed surrounding each graphite nodule (see Figure 5.11a and 5.11b); as discussed

earlier, each nodule acts as a void that grows subsequently with strain. Coalescence with neighboring voids results in ridges that outline the large equiaxed dimples. Second, voids that are about one order of magnitude smaller than primary dimples are also seen on the fracture surface (see Figure 5.11c); these secondary voids are typically observed at the boundaries of the larger dimples and are found at the ridges where the primary voids meet or link up. Such a secondary field of small voids has been experimentally observed in fracture surfaces of tensile specimens of steel and aluminum alloys (see for example, Cox and Low 1974; Hahn and Rosenfield 1975; Marini et al. 1985) and is called void-sheets that occur during coalescence of neighboring voids. Lastly, cleavage facets that are typical of ferrous alloys are also present on the fracture surface as indicated in Figure 5.11d. The topology of the facet hints at a transgranular mode of fracture. It is concluded that initially, the nodules create voids that grow by plastic flow, but the coalescence can occur either by void-sheets with a field of smaller voids or through cleavage in favorably oriented grains. However, the region in which voids grow to such large extent needs to be examined through additional micrography.

Optical micrographs of section a-a, b-b, and c-c of Specimen B are shown in Figure 5.12. The highly localized nature of the void growth and final failure is evident from a qualitative comparison of the void dimensions in these sections with the fracture surface. The distribution of void area acquired at section c-c of Specimen A and from the fractographs of Specimen B are shown in Figure 5.13. The mean dimple in the fracture plane occupies an area of 2500 μm^2 which corresponds to a mean diameter of 56 μm; we note that this is significantly smaller than the mean spacing of the nodules (95 μm), but this is to be expected since the failure plane typically runs through the more closely spaced nodules. In contrast, the mean void area in the plane c-c of Specimen A at distances about 20 μm from the fracture surface is only about 1052 μm^2, which

corresponds to a mean diameter of 36 μm – comparable to the initial nodule size. The main upshot of this measurement is the implication that fracture through void growth and coalescence occurs in an extremely narrow zone near the "fracture plane". These observations suggest that an appropriate description of the material-specific aspects of nucleation, growth and coalescence needs to be generated for each type of material in formulating constitutive relations based on porous plasticity.

5.4. SUMMARY

In this chapter, we investigate the process of deformation and evolution of porosity in initially porous materials. Nodular cast iron was used as an example of a material with pre-existing porosity, thus avoiding the complexity of modeling the nucleation process. The nodular cast iron used in this study is an ASTM A536 grade 65-45-12 ductile cast iron with a ferritic matrix that contains about 5-25% pearlite. The average grain size of ferrite and the diameter of graphite nodules were found to be about 26 ± 9 and 27 ± 25 μm, respectively. Interrupted tension tests and flat-notched tension tests were performed in order to quantify the evolution of void growth with deformation and stress state.

An optical image analysis software (ImageJ) was used to obtain microstructural characteristics of the material at different stages of the deformation and stress state; Voronoi tessellation diagram was employed to quantify the distribution of the local porosity. No significant change in the statistical evolution of the local porosity or void size distribution was observed. The evolution of the average overall porosity appeared to be the only statistically discernible parameter in the experiments.

The fracture surface indicates the following features: each nodule acts as a void that grows subsequently with strain. Coalescence with neighboring voids results in ridges that outline the large equiaxed dimples. Voids that are about one order of magnitude smaller than primary dimples are typically observed at the boundaries of the larger dimples and are found at the ridges of the primary voids. Cleavage facets that are typical of ferrous alloys are also present on the fracture surface. It was concluded that initially the nodules create voids that grow by plastic flow but this is terminated by transition of deformation into a very localized region over which the coalescence occurs either by void-sheets or through cleavage.

Table 5.1. Chemical composition of nodular cast iron.

Carbon	Silicon	Manganese	Sulfur	Phosphorus
3.50 – 3.90	2.25 – 3.00	0.15 – 0.35	0.025 Max	0.05 Max

Source: Dura-Bar, www.dura-bar.com

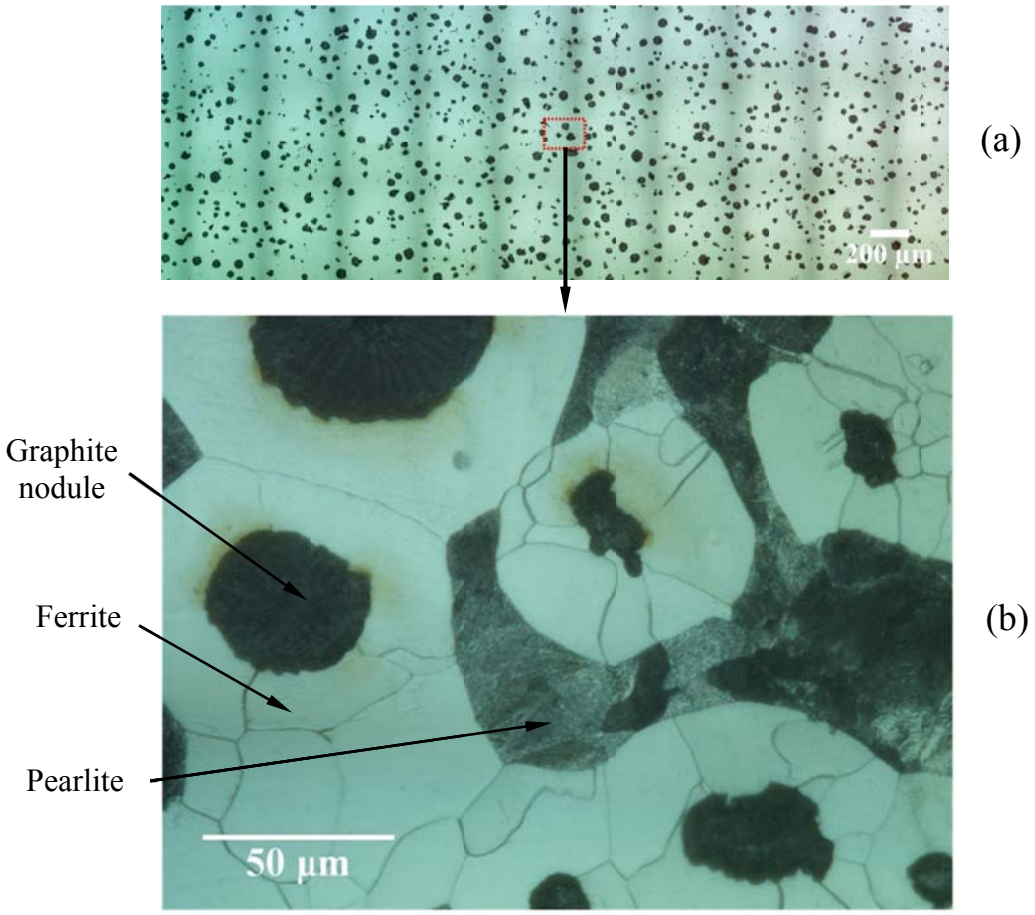

Figure 5.1. Microstructure of nodular cast iron (a) in unetched and (b) etched conditions. Different phases present in the microstructure are identified in the lower image.

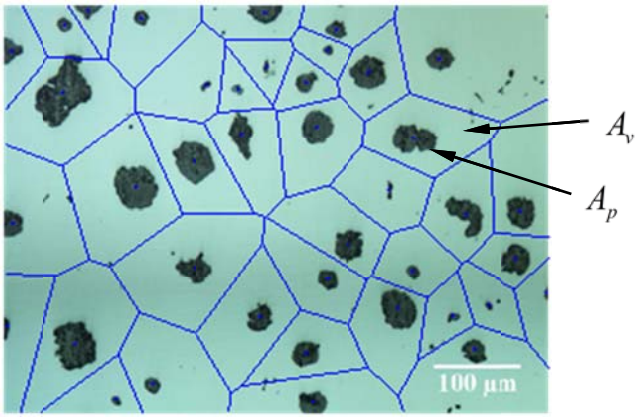

Figure 5.2. Voronoi tessellation diagram used in calculating the distribution of local porosity.

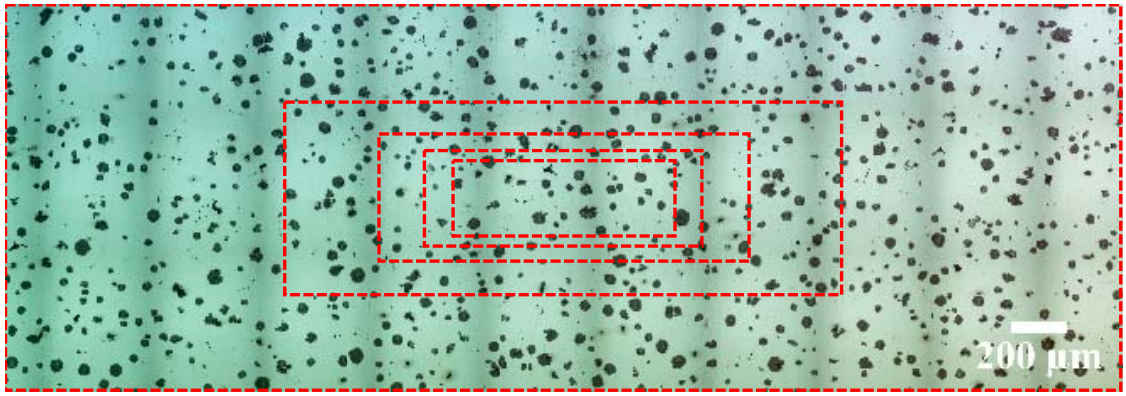

Figure 5.3. Subregions of the initial microstructure with different length scales.

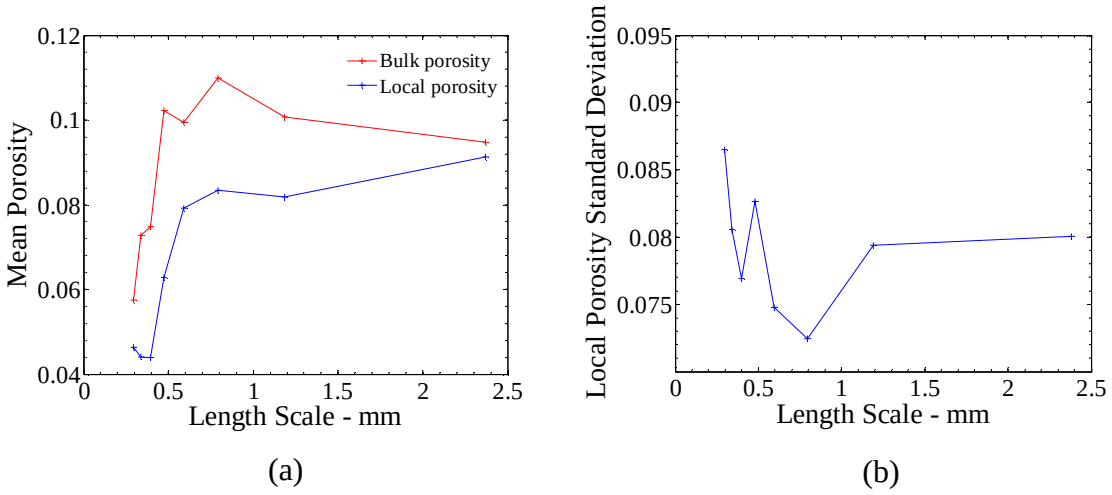

Figure 5.4. Variation of (a) the mean and (b) the standard deviation of porosity with RVE size.

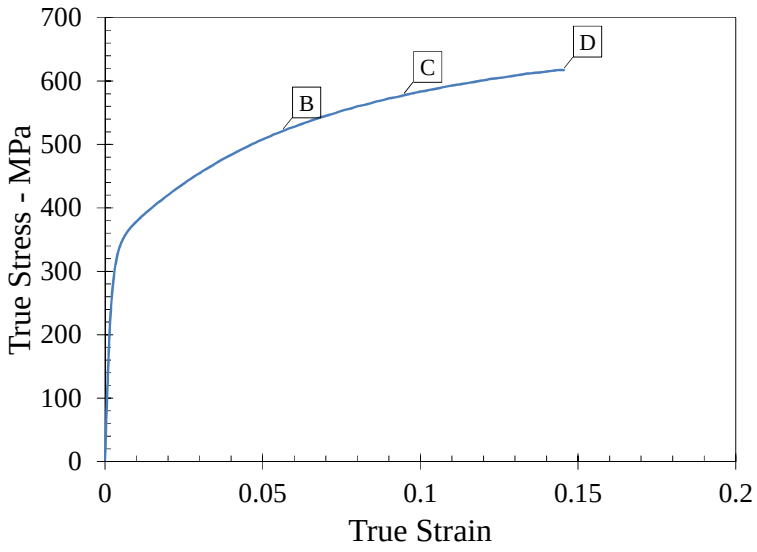

Figure 5.5. True stress-true strain response of the nodular cast iron.

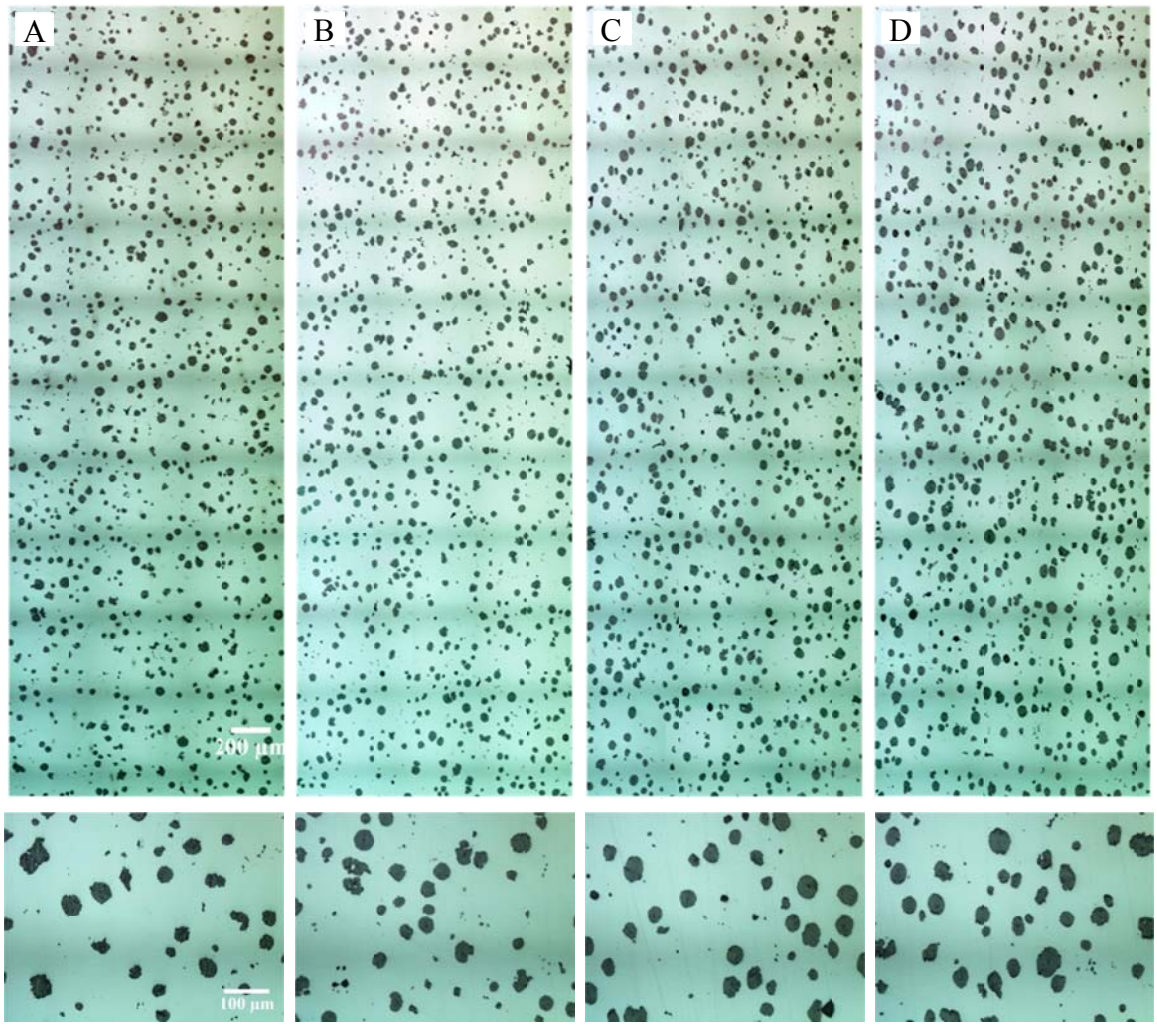

Figure 5.6. The evolution of the microstructure at different stages of tensile tests: (a) $\varepsilon_A = 0$, (b) $\varepsilon_B = 0.056$, (c) $\varepsilon_C = 0.094$ and (d) $\varepsilon_D = 0.145$. All images are to the same scale; scale bar is shown in (a). Note that these are stitched images and the dark horizontal bands are artifacts of the image compositing. Higher magnification images are shown in the bottom row.

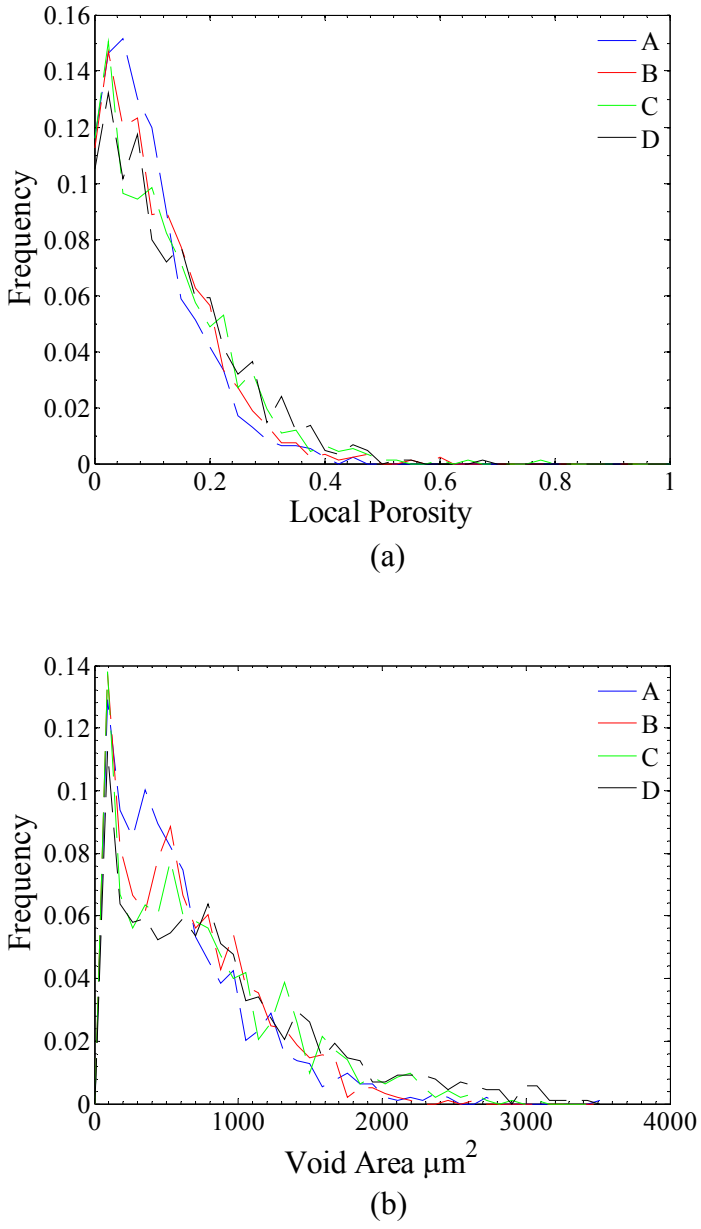

Figure 5.7. Evolution with strain of the distribution of (a) local porosity and (b) void area.

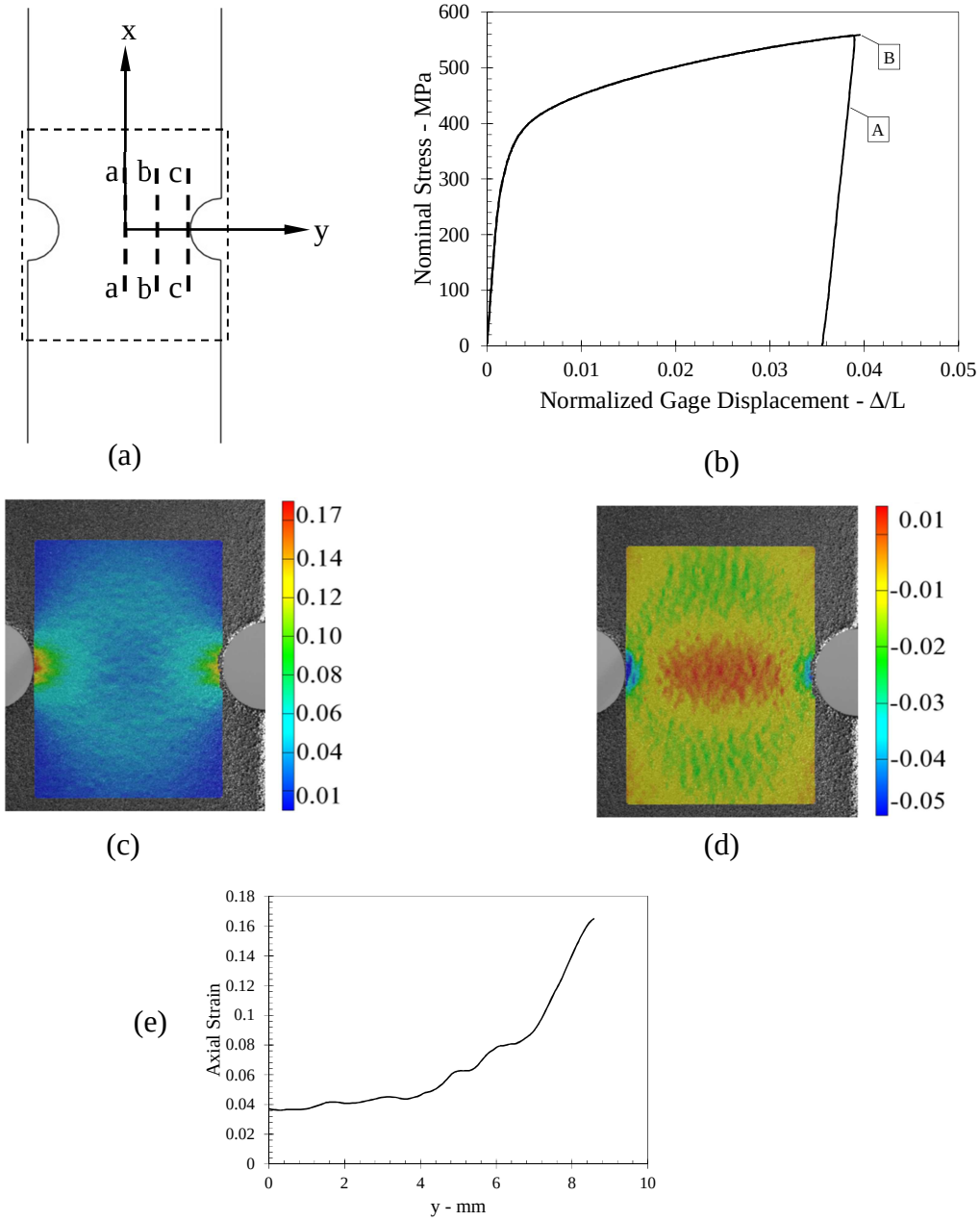

Figure 5.8. (a) Schematic diagram indicating sections a-a, b-b and c-c made across the minimum cross section. (b) Nominal stress (force/initial minimum cross-sectional area) vs. gage displacement (Δ) normalized by gage length (L= 20 mm) response curves of the flat-notched specimens. (c) Contour plot of the axial strain at the onset of final failure. (d) Contour plot of the transverse strain at the onset of final failure. (e) Variation of the axial strain along $x = 0$.

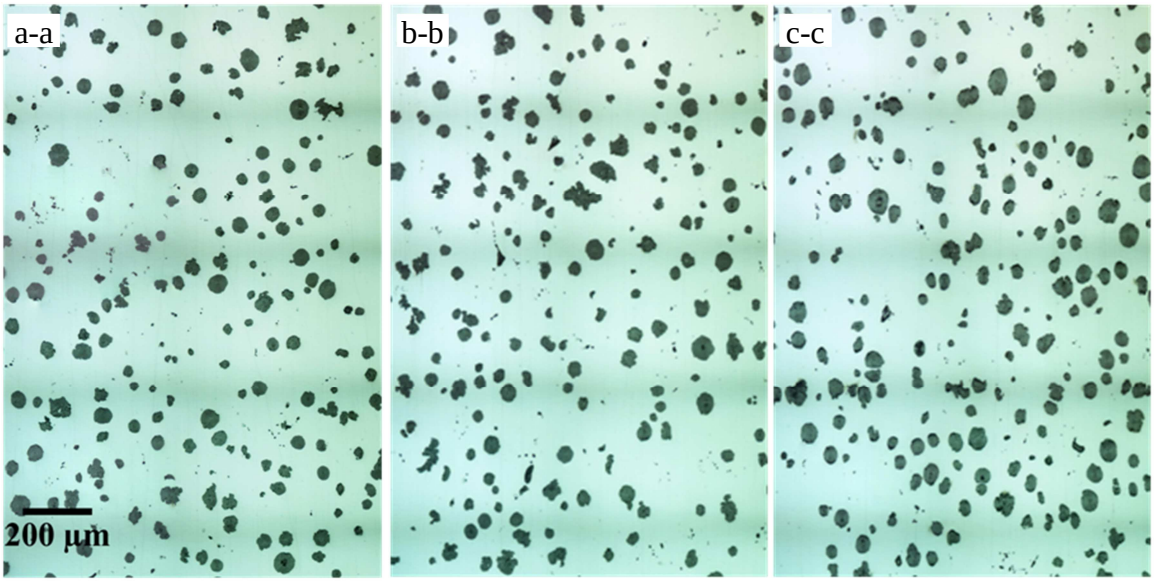

Figure 5.9. Optical micrographs of the sections a-a, b-b, and c-c; the corresponding surface strain levels are ε = 0.037, 0.049 and 0.165, respectively.

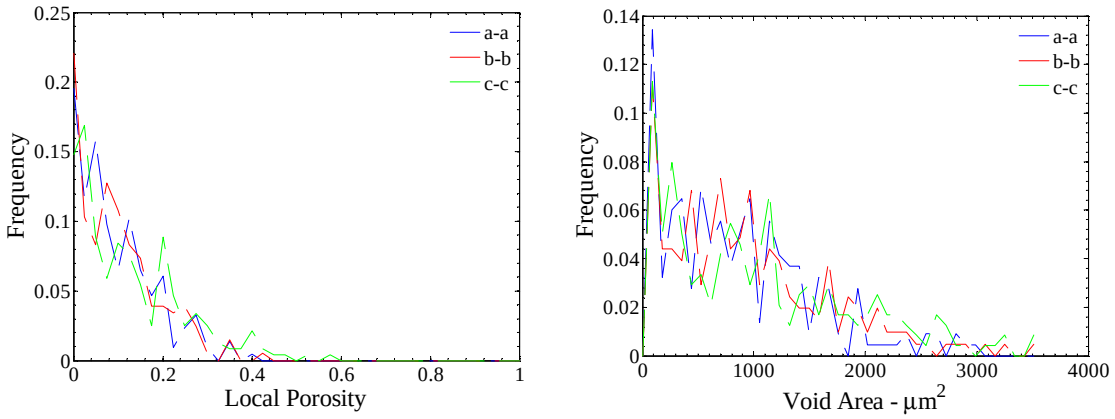

(a) (b)

Figure 5.10. Evolution of the distribution of (a) the local porosity and (b) void area for Specimen A.

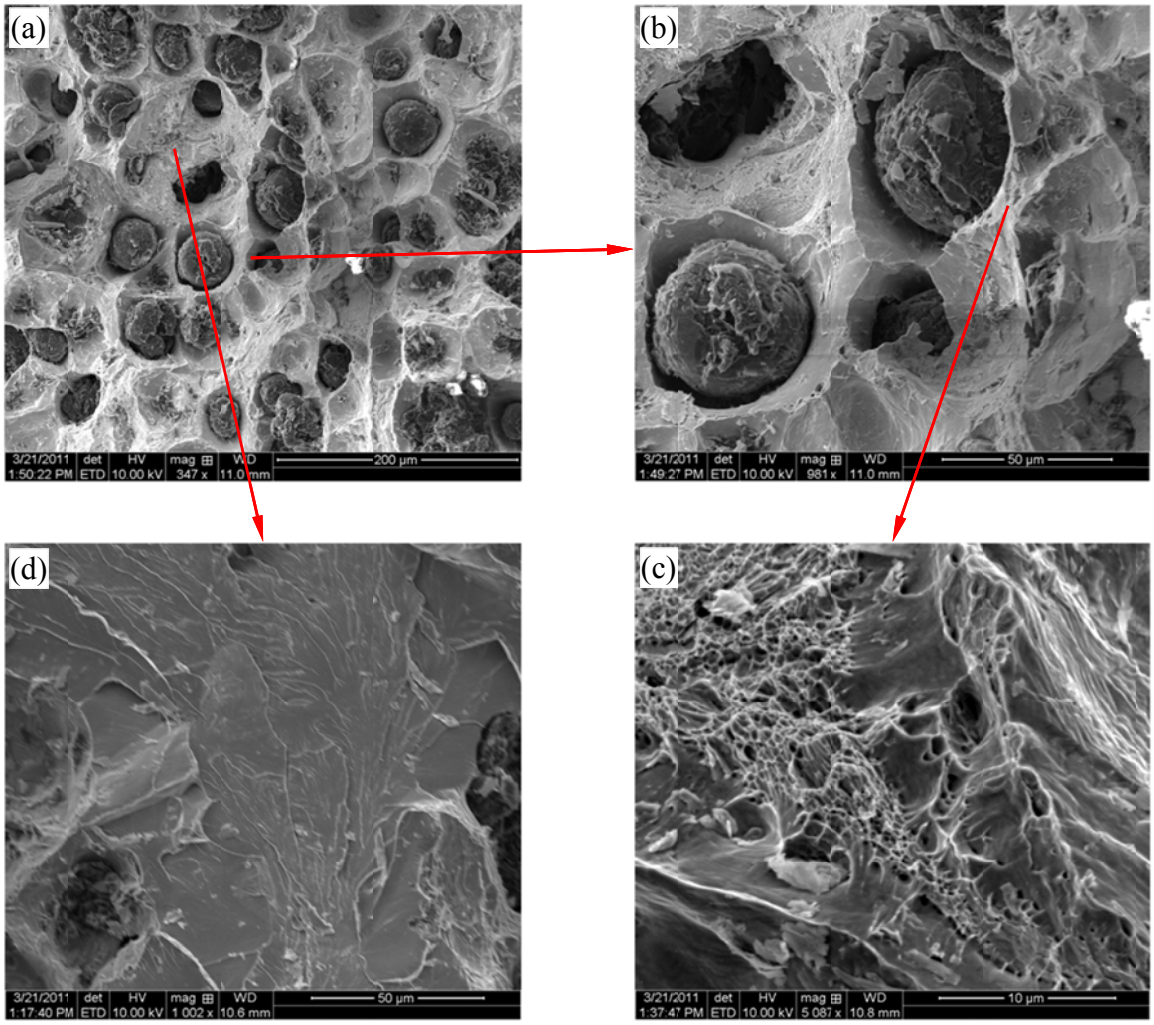

Figure 5.11. (a) Scanning electron micrographs of the fracture surface of Specimen B. (b) Equiaxed dimples surrounding each graphite nodule. (c) Secondary smaller voids at the boundary of the primary dimples. (d) Cleavage facets seen on the fracture surface.

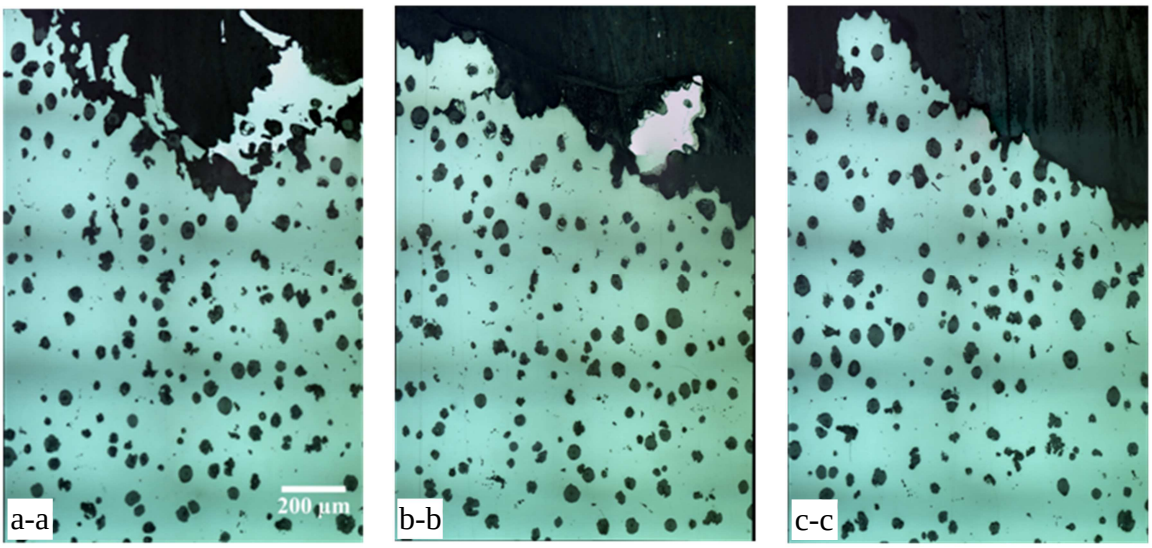

Figure 5.12. x-z micrographs of the sections a-a, b-b and c-c of the Specimen B showing the evolution of the microstructure below the fracture surface.

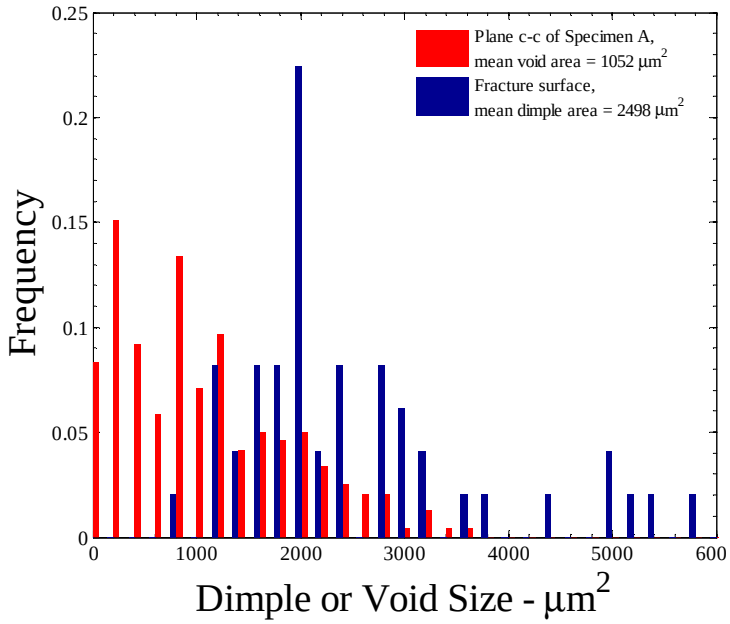

Figure 5.13. Distribution of void area acquired at section c-c of Specimen A and from the fractographs of Specimen B.

Chapter 6: Conclusions

In oxygen free, high conductivity copper, plastic deformation under uniaxial tension localizes into a neck; this is followed by shear localization across the thickness section, with the formation of shear bands oriented at an angle of 45° to the axis of tension. At the central region, where the shear bands intersect and the triaxiality is about unity, a rectangular prismatic cavity was formed. With continued straining, the rectangular cavity expanded in a self-similar manner. Scanning electron micrographs of the fracture surface indicated the absence of void growth and cleavage, suggesting alternating slip as the only mechanism for expansion of the rectangular cavity. Surface texture development was also observed in these specimens; microscopic examination of the grain level strain evolution indicated that new surfaces were generated by the alternating slip mechanism. Large strain levels were observed, with local logarithmic strain values lying in the range of 2.5 to 3.5 in regions with different triaxiality. These measurements were performed at the length scale of the grains and are significantly higher than the strain-to-failure obtained from strain measurements based on characteristic specimen dimensions.

It was concluded that in Al 6061-T6 under tensile loading, nucleation of damage does not appear for much of the deformation history until plastic strain levels of at least about 0.5-1 is reached. Once damage in the form of particle fracture or decohesion at the interface initiates, subsequent failure follows with a small increase in the overall strain. The final separation, dominated by the fluctuation in the distribution of second phase particles, occurs by the void nucleation, growth and coalescence in a highly localized layer of material on the order of the grain size. It was shown that the lower-bound strain-to-failure estimates measured at the grain level are more than double the values usually

calibrated into the Johnson-Cook model based on gage lengths related to specimen dimensions.

The deformation and failure of Al 6061-T6 under dominantly shear loading still occurs by the nucleation, growth and coalescence of voids, but the process is confined to a very small region near the fracture plane and arises only after very large plastic strains are established without generating significant damage in the material. Strain levels at the nucleation of damage were found to be greater than two, which is significantly larger than those calibrated into Johnson-Cook and modified Mohr Coulomb models. The discrepancy between these models and our experimental results is attributed to the selection of an inappropriately large gage length over which the strain is measured in conventional tests; in contrast, the present experimental results use a gage-length that is based on the characteristic microstructural length – the grain size.

In nodular cast iron, which was used as a material with pre-existing porosity, the fracture surface indicates the following features: each nodule acts as a void that grows subsequently with strain. Coalescence with neighboring voids results in ridges that outline the large equiaxed dimples. Voids that are about one order of magnitude smaller than primary dimples are typically observed at the boundaries of the larger dimples and are found at the ridges of the primary voids. Cleavage facets that are typical of ferrous alloys are also present on the fracture surface. It was concluded that initially the nodules create voids that grow by plastic flow but this is terminated by transition of deformation into a very localized region over which the coalescence occurs either by void-sheets or through cleavage.

Appendix A

A variation of digital image correlation called Q4-DIC (Besnard et al. 2006) and its extension Q4-XDIC (Réthoré et al. 2007) is presented here. Digital image correlation is based on the principle of conservation of optical flow which assumes that the deformation of the image takes place by in-plane displacement fields without any change in gray level values of the image; in other words:

$$f(\mathbf{x}-\mathbf{u}(\mathbf{x}))=g(\mathbf{x}) \tag{A.1}$$

where $f(\mathbf{x})$ and $g(\mathbf{x})$ are the gray level intensity values of the undeformed and deformed images and $\mathbf{u}(\mathbf{x})$ is the surface displacement field. Assuming the differentiability of the undeformed image $f(\mathbf{x})$ and small deformation, the Taylor expansion of f to the first order can be written as follows

$$f(\mathbf{x})-\mathbf{u}(\mathbf{x})\cdot\nabla f(\mathbf{x})=g(\mathbf{x}) \tag{A.2}$$

The calculation of displacement $\mathbf{u}(\mathbf{x})$ is an ill-posed problem; as such additional regularizations need to be made in order to calculate the displacement. If the displacement is assumed to be piecewise constant then it yields the maximizing the cross correlation coefficient of f and g used in subset matching scheme. Let us introduce the quadratic functional as follows

$$\phi=\int_{\Omega}\left[f(\mathbf{x})-\mathbf{u}(\mathbf{x})\cdot\nabla f(\mathbf{x})-g(\mathbf{x})\right]^2 d\mathbf{x} \tag{A.3}$$

Displacement field $\mathbf{u}(\mathbf{x})$ is obtained by minimizing the functional above. The displacement field is regularized in terms of a set of basis functions that takes the form

$$\mathbf{u}(\mathbf{x}) = \sum_{\alpha,n} q_{\alpha n}\psi_n(\mathbf{x})\mathbf{e}_\alpha \tag{A.4}$$

where $\mathbf{e}_\alpha$ is the unit vector in dimension α and $q_{\alpha n}$ is unknown amplitude associated with $\psi_n(\mathbf{x})$. The objective functional is now takes the form

$$\phi = \int_\Omega \left[-\sum_{\alpha,n} q_{\alpha n}\psi_n(\mathbf{x})\nabla f(\mathbf{x})\cdot\mathbf{e}_\alpha + f(\mathbf{x}) - g(\mathbf{x}) \right]^2 d\mathbf{x} \tag{A.5}$$

Now, the minimization problem leads to the following linear system

$$\mathbf{K} = \mathbf{qf} \tag{A.6}$$

where

$$K_{\alpha n\beta m} = \int_\Omega \left[\psi_m(\mathbf{x})\psi_n(\mathbf{x})\partial_\alpha f(\mathbf{x})\partial_\beta f(\mathbf{x})\right] d\mathbf{x} \tag{A.7}$$

$$f_{\alpha n} = \int_\Omega \left[f(\mathbf{x}) - g(\mathbf{x})\right]\psi_n(\mathbf{x})\partial_\alpha f(\mathbf{x}) d\mathbf{x} \tag{A.8}$$

and $\mathbf{K}$ and $\mathbf{f}$ can be seen as stiffness matrix and force vector as in finite element analysis.

A.1 Q4-DIC

Finite element simulations are widely used for calibration and verification purposes in material characterization. Therefore, using compatible kinematic descriptions in finite element discretizations and experimental measurements will reduce the interpolation errors due to mismatch in discretization. Motivated by this and the fact that images are discretized into pixels, the Q4-shape functions as in finite element are used as basis functions in minimization of the objective functional. Each element is mapped onto a master element in a local coordinate system $[0\ 1]^2$ with the following shape functions.

$$\begin{cases} N_1 = (1-x)(1-y) \\ N_2 = x(1-y) \\ N_3 = (1-x)y \\ N_4 = xy \end{cases} \tag{A.9}$$

The displacement field is expressed in terms of the shape functions as follows

$$\mathbf{u}^e(\mathbf{x}) = \sum_{n}^{n_e} \sum_{\alpha} q_{\alpha n}^e N_n(\mathbf{x}) \mathbf{e}_\alpha \tag{A.10}$$

where n_e is the number of nodes in the master element and $q_{\alpha n}^e$ are the nodal unknowns. Associated with each element a local stiffness matrix $\mathbf{K}^e$ and force vector $\mathbf{f}^e$ are constructed as follows

$$\begin{aligned} K_{\alpha n \beta m}^e &= \int_{\Omega^e} \left[N_m(\mathbf{x}) N_n(\mathbf{x}) \partial_\alpha f(\mathbf{x}) \partial_\beta f(\mathbf{x}) \right] d\mathbf{x} \\ f_{\alpha n}^e &= \int_{\Omega^e} \left[f(\mathbf{x}) - g(\mathbf{x}) \right] N_n(\mathbf{x}) \partial_\alpha f(\mathbf{x}) d\mathbf{x} \end{aligned} \tag{A.11}$$

Thus, the global stiffness $\mathbf{K}$ and force vector $\mathbf{f}$ are found by assembling the local $\mathbf{K}^e$ and $\mathbf{f}^e$.

Newton iterative method was used to solve for nodal unknowns $\mathbf{q}$ in equation (A.6). At each iteration the deformed image g is translated by the correction $\mathrm{d}\mathbf{q}^i$ that is calculated as

$$\mathrm{d}\mathbf{q}^i = \mathbf{q}^{i+1} - \mathbf{q}^i \tag{A.12}$$

Each element in image g is translated by the average displacement of the four nodes of each element. The integer part of the translation is performed by simply shifting the coordinates while a bi-cubic spline was used for sub-pixel translation. This procedure continues until the convergence is achieved.

A.2 MULTI-SCALE ALGORITHM

The linearization based on Taylor expansion limits the applicability of Q4-DIC method to the small displacements. In addition, images contain highly irregular textures that lead to multiple local minima in ϕ. So in order to deal with large deformations and avoid local minima, a multi-scale algorithm called coarse graining is adopted to increase the robustness of the Q4-DIC technique. In this algorithm, the gray level values of $2^1 \times 2^1$ pixels of the image are averaged to form super pixels at the level 1; continuing in the same manner the super pixels of size $2^n \times 2^n$ pixels are formed at level n (Figure A.1). Now, at the coarsest level n where the high frequency content of the image texture has been filtered out, the displacements are evaluated using the Newton iterative method; then the nodal displacements are interpolated into the next level $(n-1)$ as the initial values for the nodal displacements at this level; the iterative solver is used again to solve for the converged values of nodal displacements. This procedure continues until the finest level that corresponds to the actual image is reached. It is noted that in passing down each level more information is being included in the calculations; in other words, displacement amplitudes are further refined at each level.

A.3 EXTENDED DIGITAL IMAGE CORRELATION

In the presence of discontinuities in the displacement fields, calculation of the displacement field using Q4-DIC leads to increased inaccuracy near the discontinuities. In order to mitigate this issue continuous shape functions are enriched with discontinuous and/or singular functions as in XFEM. In this method, the partition of unity of shape functions over the patch covered by the set of nodes κ which reads

$$\sum_{n\in\kappa} N_n(\mathbf{x}) = 1 \tag{A.13}$$

is used to enrich the standard shape functions as follows

$$\mathbf{u}(\mathbf{x}) = \sum_{n\in\kappa}\sum_{\alpha} q_{\alpha n} N_n(\mathbf{x})\mathbf{e}_\alpha + \sum_{n\in\kappa_{enr}}\sum_{\alpha} d_{\alpha n} N_n(\mathbf{x})\varphi_n(\mathbf{x})\mathbf{e}_\alpha \tag{A.14}$$

where φ_n are the enrichment functions and κ_{enr} is a sub-set of κ in which the nodes have enriched degrees of freedom $d_{\alpha n}$. Now if the attention is focused on a crack, one discontinuous function across the crack can be introduced as follows

$$\mathbf{u}(\mathbf{x}) = \sum_{n\in\kappa}\sum_{\alpha} q_{\alpha n} N_n(\mathbf{x})\mathbf{e}_\alpha + \sum_{n\in\kappa_{cut}}\sum_{\alpha} d_{\alpha n} N_n(\mathbf{x})H(\mathbf{x})\mathbf{e}_\alpha \tag{A.15}$$

where

$$H_n(\mathbf{x}) = \mathrm{H}(\mathbf{x}) - \mathrm{H}(\mathbf{x}_n), \tag{A.16}$$

H is the Heaviside function and $\mathbf{x}_n$ is the position of the node whose support (set of elements that have the same node within their connectivity) has been cut by the discontinuity (see Figure A.2). This algorithm was implemented in a MATLAB. code.

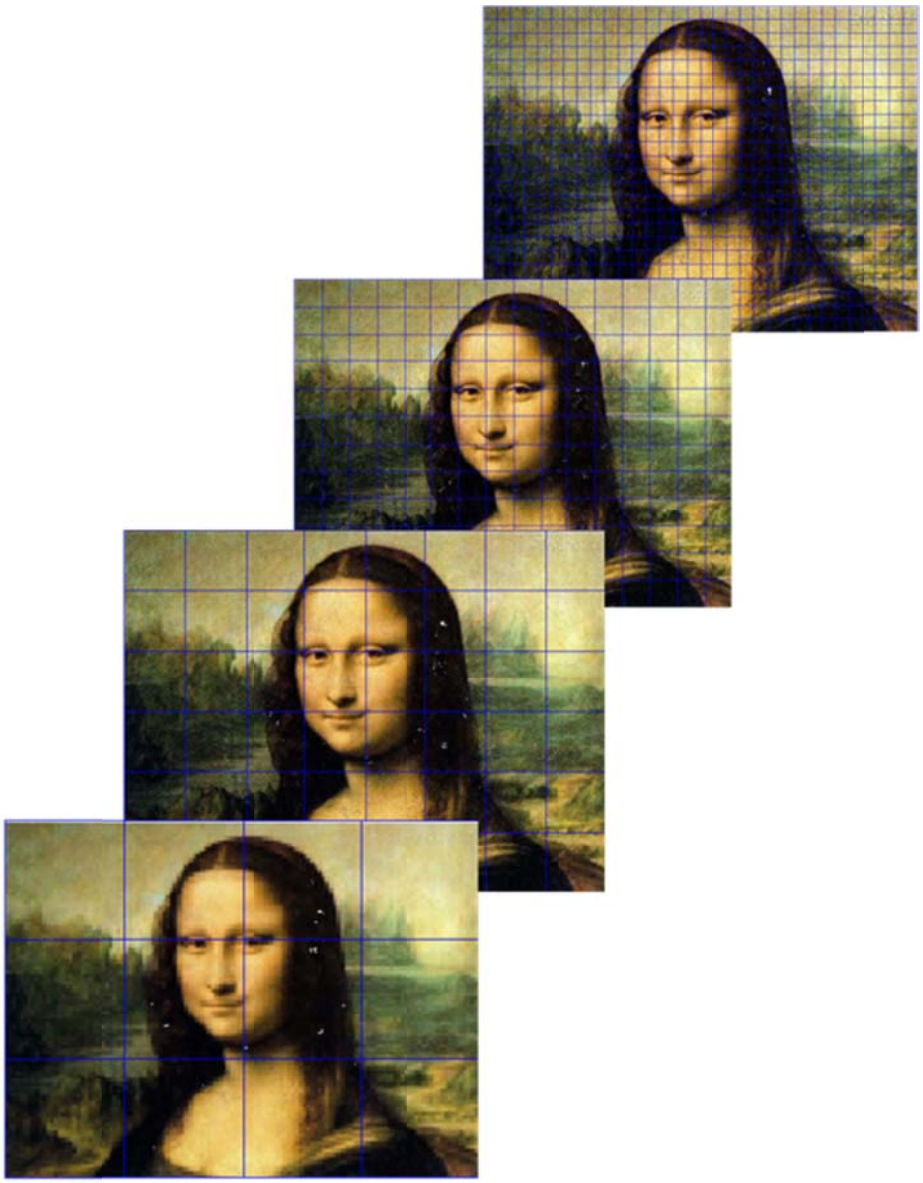

Figure A.1. Coarse graining procedure used in multi-scale algorithm.

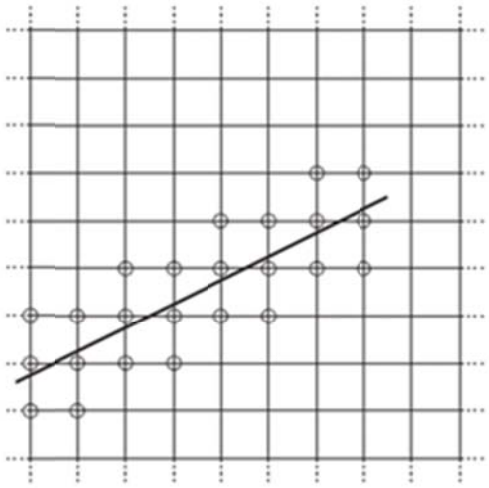

Figure A.2. Discontinuous enrichments (adapted from Réthoré et al. 2007).

References

Anand L and Kalidindi SR, 1994, The process of shear band formation in plane strain compression of fcc metals: Effects of crystallographic texture, *Mechanics of Materials*, **17**, 223-243.

Anand L and Spitzig WA, 1980, Initiation of localized shear bands in plane strain, *Journal of the Mechanics and Physics of Solids*, **28**, 113-128.

Argon AS and Im J, 1975, Separation of second phase particles in spheroidized 1045 Steel, Cu-0.6 % Cr alloy, and maraging steel in plastic straining, *Metallurgical Transactions A*, **6A**, 839-851.

Argon AS, Im J and Needleman A, 1975a, Distribution of plastic strain and triaxial tensile stress in necked steel and copper bars, *Metallurgical Transactions A*, **6A**, 815-824.

Argon AS, Im J and Safoglu R, 1975b, Cavity formation from inclusions in ductile fracture, *Metallurgical Transactions A*, **6A**, 825–837.

ASM International, 2002, Metallographer's Guide: Irons and Steels.

Babout L, Brechet Y, Maire E and Fougères R, 2004, On the competition between particle fracture and particle decohesion in metal matrix composites, *Acta Materialia*, **52**, 4517-4525.

Bao Y and Wierzbicki T, 2004, On fracture locus in the equivalent strain and stress triaxiality space, *International Journal of Mechanical Sciences*, **46**, 81-98.

Barlat F, Brem JC, Yoon JW, Chung K, Dick RE, Lege DJ, Pourboghrat F, Choi S-H and Chu E, 2003, Plane stress function for aluminum alloy sheets - Part I: theory. *International Journal of Plasticity*, **19**, 1297-1319.

Barsoum I and Faleskog J, 2007, Rupture in combined tension and shear: Experiments, *International Journal of Solids and Structures*, **44**, 1768-1786.

Beachem CD, 1963, An electron fractographic study of the influence of plastic strain conditions upon ductile rupture processes in metals, *Transactions of the ASM*, **56**, 318-326.

Becker R and Richmond O, 1994, Incorporation of microstructural geometry in material modelling, *Modelling and Simulation in Materials Science and Engineering*, **2**, 439-454.

Becker R, 1987, The effect of porosity distribution on ductile failure, *Journal of the Mechanics and Physics of Solid*, **35**, 577–599.

Beese AM, Luo M, Li Y, Bai Y and Wierzbicki T, 2010, Partially coupled anisotropic fracture model for aluminum sheets, *Engineering Fracture Mechanics*, **77**, 1128-1152.

Benseddiq N and Imad A, 2008, A ductile fracture analysis using a local damage model, *International Journal of Pressure Vessels and Piping*, **85**, 219-227.

Benzerga AA and Besson J, 2001, Plastic potentials for anisotropic porous solids, *European Journal of Mechanics A/Solids*, **20A**, 397-434.

Benzerga AA and Leblond J-B, 2010, Ductile fracture by void growth to coalescence, *Advances in Applied Mechanics*, **44**, 169-305.

Benzerga AA, 2002, Micromechanics of coalescence in ductile fracture, *Journal of the Mechanics and Physics of Solids*, **50**, 1331-1362.

Benzerga AA, Besson J and Pineau A, 2004, Anisotropic ductile fracture, Part I: experiments, *Acta Materialia*, **52**, 4623-4638.

Beremin FM, 1981, Cavity formation from inclusions in ductile fracture of A508 steel, *Metallurgical Transactions A*, **12A**, 723-731.

Bernauer G and Brocks W, 2002, Micro-mechanical modelling of ductile damage and tearing – results of a European numerical round robin, *Fatigue & Fracture of Engineering Materials & Structures*, **25**, 363-384.

Berveiller M and Zaoui A, 1979, An extension of the self-consistent scheme to plastically-flowing polycrystals, *Journal of the Mechanics and Physics of Solids*, **35**, 325-344.

Besnard G, Hild F and Roux S, 2006, 'Finite-element' displacement fields analysis from digital images: application to Portevin–le châtelier bands, *Experimental Mechanics*, **46**, 789-803.

Bilger N, Auslender F, Bornert M, Michel J-C, Moulinec H, Suquet P and Zaoui A, 2005, Effect of a nonuniform distribution of voids on the plastic response of voided materials: a computational and statistical analysis, *International Journal of Solids and structures*, **42**, 517-538.

Bishop JFW and Hill R, 1951, A theory of the plastic distortion of a polycrystalline aggregate under combined stress, *Philosophical Magazine*, **42**, 414-427.

Bridgman PW, 1964, *Studies in Large Plastic Flow and Fracture*, Cambridge, MA: Harvard University Press.

Brocks W, Sun DZ and Honig A, 1996, Verification of micromechanical models for ductile fracture by cell model calculations, *Computational Materials Science*, **7**, 235-241.

Brown LM and Embury JD, 1973, The initiation and growth of voids at second phase particles, *Proceedings of the Third International Conference on the Strength of Metals and Alloys I CSMA*, **3**, Cambridge, England, 164-169.

Butcher CJ and Chen ZT, 2009, Damage percolation modeling of void nucleation within heterogeneous particle distributions, *Modelling and Simulation in Materials Science and Engineering*, **17**, 1-16.

Carroll J, Abuzaid W, Lambros J and Sehitoglu H, 2010, An experimental methodology to relate local strain to microstructural texture, *Review of Scientific Instruments*, **81**, 083703.

Chae D and Koss DA, 2004, Damage accumulation and failure of HSLA-100 steel, *Materials Science and Engineering A*, **366A**, 299-309.

Chawla N and Deng X, 2005, Microstructure and mechanical behavior of porous sintered steels, *Materials Science and Engineering A,* **390A**, 98-112.

Chen ZT, Worswick MJ, Cinotti N, Pilkey AK and Lloyd D, 2003, A linked FEM-damage percolation model of aluminum alloy sheet forming, *International Journal of Plasticity*, **19**, 2099-2120.

Chu CC, Needleman A., 1980, Void nucleation effects in biaxially stretched sheets. *Journal of Engineering Materials and Technology*, **102**, 249-56.

Clausing DP, 1970, Effect of plastic strain state on ductility and toughness, *International Journal of Fracture Mechanics*, **6**, 71-85.

Cox TB and Low JR, 1974, An investigation of the plastic fracture of AISI 4340 and 18 nickel-200 grade maraging steels, *Metallurgical Transactions* A, **5A,** 1457-1470.

Decamp K, Bauvineau L, Besson J and Pineau A, 1997, Size and geometry effects on ductile rupture of notched bars in a C–Mn steel. Experiments and modelling, *International Journal of Fracture*, **88**, 1-18.

Dong MJ, Berdin C, Beranger AS and Prioul C, 1996, Damage effect in the fracture toughness of nodular cast iron. In: *First European mechanics of materials conference on local approach to fracture*, Fontainebleau, September.

Dong MJ, Prioul C and Francois D, 1997, Damage effect on the fracture toughness of nodular cast iron: Part I. damage characterization and plastic flow stress, modeling, *Metallurgical and Materials Transactions A*, **28A**, 2245-2254.

Eshelby JD, 1957, The determination of the elastic field of an ellipsoidal inclusion and related problems, *Proceedings of the Royal society London A*, **241A**, 376–396.

Fabrègue D and Pardoen T, 2008, A constitutive model for elastoplastic solids containing primary and secondary voids, *Journal of the Mechanics and Physics of* Solids, **56,** 719-741.

Follansbee PS and Kocks, UF, 1988, A constitutive description of the deformation of copper based on the use of the mechanical threshold stress as an internal state variable, *Acta Metallurgica*, **36**, 81-93.

French IE, and Weinrich PF, 1974, The influence of hydrostatic pressure on the tensile deformation and fracture of copper, *Metallurgical Transactions A*, **6A**, 785-790.

French IE, and Weinrich PF, 1975, The shear mode of ductile fracture in materials with few inclusions, *Metallurgical Transactions A*, **7A**, 1841-1845.

French IE, and Weinrich PF, 1976, The shear mode of ductile fracture in a spheroidized steel, *Metallurgical Transactions A*, **10A**, 297-304.

French IE, and Weinrich PF, 1977, The shear mode of ductile fracture in commercial copper, *Acta Metallurgica*, **11**, 965-968.

Ghosh S, Bai J and Paquet D, 2009, Homogenization-based continuum plasticity-damage model for ductile failure of materials containing heterogeneities, *Journal of the Mechanics and Physics of Solids*, **57**, 1017-1044.

Gologanu M, Leblond J-B and Devaux J, 1993, Approximate models for ductile metals containing nonspherical voids — case of axisymmetric prolate ellipsoidal cavities, *Journal of the Mechanics and Physics of Solids*, **41**, 1723-1754.

Gologanu M, Leblond J-B and Devaux J, 1994, Approximate models for ductile metals containing nonspherical voids — case of axisymmetric oblate ellipsoidal cavities. *Journal of Engineering Materials and Technology*, **116**, 290-297.

Gologanu M, Leblond J-B, Perrin G and Devaux J, 1995, Recent extensions of Gurson's model for porous ductile metals. In: Suquet, P. (Ed.) Continuum Micromechanics. Springer-Verlag.

Guillemer-Neel C, Feaugas X and Clavel M, 2000, Mechanical behavior and damage kinetics in nodular cast iron: Part I. Damage mechanisms, *Metallurgical and Materials Transactions* A, **31A**, 3063-3074.

Gurson A, 1977, Continuum theory of ductile rupture by void nucleation and growth: Part I – Yield criteria and flow rules for porous ductile media, *Journal of Engineering Materials and Technology*, **99**, 2-15.

Hahn GT and Rosenfeld AR, 1975, Metallurgical factors affecting fracture toughness of aluminium alloys, *Metalurgical Transactions*, **6**, 653-670.

Hancock JW and Mackenzie AC, 1976, On the mechanisms of ductile failure in high-strength steels subjected to multi-axial stress-states, *Journal of the Mechanics and Physics of Solids*, **24**, 147-169.

Hu XH, Wilkinson DS, Jain M, Wu PD and Mishra RK, 2011, The impact of particle distributions and grain-level inhomogeneities on post-necking deformation and fracture in AA5754 sheet alloys during uniaxial tension, *Materials Science and Engineering: A*, **528A**, 2002-2016.

Hung SC and Liechti KM, 1997, An evaluation of the Arcan specimen for determining the shear moduli of fiber reinforced composites, *Experimental Mechanics*, **37**, 460-468.

Hung S-C and Liechti KM, 1999, Finite element analysis of the Arcan specimen for fiber reinforced composites under pure shear and biaxial loading, *Journal of Composite Materials*, **33**, 1288-1317.

Hutchinson JW and Tvergaard V, 1980, Surface instabilities on statically strained plastic solids, *International Journal of Mechanical Sciences*, **22**, 339-354.

Jablokov V, Goto DM and Koss DA, 2001, Damage accumulation and failure of HY-100 steel, *Metallurgical and Materials Transactions A*, **32A**, 2985-2994.

Johnson GR and Cook WH, 1985, Fracture characteristics of three metals subject to various strains, strain rates, temperatures and pressures, *Engineering Fracture Mechanics*, **21**, 31-48.

Keralavarma SM and Benzerga AA, 2008, An approximate yield criterion for anisotropic porous media, *C.R. Mecanique*, **336**, 685-692.

Keralavarma SM and Benzerga AA, 2010, A constitutive model for plastically anisotropic solids with non-spherical voids, *Journal of the Mechanics and Physics of Solids*, **58**, 874-901.

Koplik J and Needleman A, 1988, Void growth and coalescence in porous plastic solids, *International Journal of Solids and Structures*, **24**, 835-853.

Korkolis, YP and Kyriakides S, 2008a, Inflation and burst of anisotropic aluminum tubes for hydroforming applications, *International Journal of Plasticity*, **24**, 509-543.

Korkolis, YP and Kyriakides S, 2008b, Inflation and burst of anisotropic aluminum tubes, part II: an advanced yield function including deformation-induced anisotropy, *International Journal of Plasticity*, **24**, 1625-1637.

Krajcinovic D, 1996, *Damage Mechanics*, North-Holland.

Lee BJ and Mear ME, 1999, Stress concentration induced by an elastic spheroidal particle in a plastically deforming solid. *Journal of the Mechanics and Physics of Solids*, **47**, 1301-1336.

Lemaitre J and Desmorat R, 2006, *Engineering Damage Mechanics: Ductile, Creep, Fatigue and Brittle Failures*. Springer-Verlag Berlin and Heidelberg GmbH & Co. KG.

Lesuer DR, Kay GJ and LeBlanc MM, 2001, Modeling large strain, high-rate deformation in metals, *Modeling the Performance of Engineering Structural Materials II, In Proceedings of a Symposium Sponsored by the SMD of TMS, Indianapolis*, IN, 75-86.

Lindholm US, Nagy A, Johnson GR and Hoegfeldt JM, 1980, Large strain, high strain rate testing of copper, *Journal of Materials Engineering and Technology*, **102**, 376-381.

Ludwik P, 1926, *Zeitschrift fur Metallkunde*, 269; quoted by Orowan (1948).

Marini B, Mudry F and Pineau A, 1985, Experimental study of cavity growth in ductile rupture, *Engineering Fracture Mechanics*, **22**, 989-996.

McClintock FA, 1968, A Criterion for ductile fracture by the growth of holes, *Journal of Applied Mechanics*, **35**, 363-371.

Mear ME and Hutchinson JW, 1985, Influence of yield surface curvature on flow localization in dilatant plasticity, *Mechanics of Materials*, **4**, 395-407.

Michel JC, Moulinec H and Suquet P, 2001, A computational scheme for linear and non-linear composites with arbitrary phase contrast, *International Journal for Numerical Methods in Engineering*, **52**, 139-160.

Monchiet V, Cazacu O, Charkaluk E and Kondo D, 2008, Macroscopic yield criteria for plastic anisotropic materials containing spheroidal voids, *International Journal of Plasticity*, **24**, 1158-1189.

Moulinec H and Suquet P, 1998, A numerical method for computing the overall response of nonlinear composites with complex microstructure, *Computer Methods in Applied Mechanics and Engineering*, **157**, 69-94.

Nahshon K and Hutchinson JW, 2008, Modification of the Gurson model for shear, *European Journal of Mechanics - A/Solids*, **27A**, 1-17.

Needleman A and Tvergaard V, 1984, An analysis of ductile rupture in notched bars, *Journal of the Mechanics and Physics of Solids*, **32**, 461-490.

Nemat-Nasser S and Li Y, 1998, Flow stress of FCC polycrystals with application to OFHC Cu, *Acta Materialia*, **46**, 565-577.

Orowan E, 1948, Fracture and strength of solids, *Report on Progress in Physics*, **12**, 185-232.

Pardoen T and Hutchinson JW, 2000, An extended model for void growth and coalescence, *Journal of the Mechanics and Physics of Solids*, **48**, 2467-2512.

Pardoen T, Delannay F, 1998, Assessment of void growth models from porosity measurements in cold-drawn copper bars, *Metallurgical and Materials Transactions A*, **29A**, 1895-1909.

Pardoen T, Doghri I and Delannay F, 1998, Experimental and numerical comparison of void growth models and void coalescence criteria for the prediction of ductile fracture in copper bars, *Acta Materialia*, **46**, 541-552.

Puttick KE, 1959, Ductile fracture in metals, *Philosophical Magazine*, **4**, 954-969.

Puttick KE, 1960, Shear component of ductile failure, *Philosophical Magazine*, **5**, 759-762.

Réthoré J, Hild F and Roux S, 2007, Extended digital image correlation with crack shape optimization, *International Journal for Numerical Methods in Engineering*, **73**, 248-272.

Rice J and Tracy D, 1969, On the ductile enlargement of voids in triaxial stress fields, *Journal of the Mechanics and Physics of Solids*, **17**, 201-217.

Rogers HC, 1960, The tensile fracture of ductile metals, *Transactions of the Metallurgical Society of AIME*, **218**, 498-506.

Rousselier G, 1987, Ductile fracture models and their potential in local approach of fracture. *Nuclear Engineering and Design*, **105**, 97-111.

Shimizu I and Abe T, 2001, Three dimensional evolution of free surface roughening topography of aluminum sheet during various plastic strain paths, *Transactions of the Japan Society of Mechanical Engineers*, **A-67**, 1761-1768.

Spencer K, Corbin SF and Llyod DJ, 2002, The influence of iron content on the plane strain fracture behavior of AA 5754 Al-Mg sheet alloys, *Materials Science and Engineering A*, **A325**, 394-404.

Spitzig WA, 1990, Effect of hydrostatic pressure on deformation, damage evolution, and fracture of iron with various initial porosities, *Acta Metallurgica et Materialia*, **38**, 1445-1453.

Spitzig WA, Smelser RE and Richmond O, 1988, The evolution of damage and fracture in iron compact with various initial porosities, *Acta Metallurgica*, **36**, 1201-1211.

Steglich D and Brocks W, 1997, Micromechanical modelling of the behavior of ductile materials including particles, *Computational Materials Science*, **9**, 7-17.

Steglich D and Brocks W, 1998, Micromechanical modelling of damage and fracture of ductile materials, *Fatigue and Fracture of Engineering Materials and Structures*, **21**, 1175-1188.

Stoudt MR and Hubbard JB, 2009, Fundamental relationships between deformation-induced surface roughness, critical strain localization and failure in AA5754-O, *Philosophical Magazine*, **89**, 2403-2425.

Sutton MA, Wolters WJ, Peters WH, Ranson WF and McNeill SR, 1983, Determination of displacements using an improved digital correlation method, *Image and Vision Computing*, **1**, 133-139.

Taylor GI, 1938, Plastic strain in metals, *Journal of the Institute of Metals*, **62**, 307-324.

Thomason PF, 1985a. A three–dimensional model for ductile fracture by the growth and coalescence of microvoids, *Acta Metallurgica*, **33**, 1087-1095.

Thomason PF, 1985b. Three–dimensional models for the plastic limit–loads at incipient failure of the intervoid matrix in ductile porous solids, *Acta Metallurgica*, **33**, 1079-1085.

Thomason PF, 1990, *Ductile Fracture of Metals*, Oxford, Pergamon Press.

Tipper C F, 1949, The fracture of metals, *Metallurgia*, **39**, 133-137.

Tong W and Clifton, RJ, 1992, Pressure-shear impact investigation of strain rate history effects in oxygen-free high-conductivity copper, *Journal of the Mechanics and Physics of Solids*, **40**, 1251-1294.

Tvergaard V, 1981, Influence of voids on shear band instabilities under plane strain conditions, *International Journal of Fracture*, **17**, 389-407.

Tvergaard V, 1990, Material failure by void growth to coalescence, *Advances in Applied Mechanics*, **27**, 83-151.

Tvergaard V, Needleman A, and Lo KK, 1981, Flow localization in the plane strain tensile test, *Journal of the Mechanics and Physics of Solids*, **29**, 15-142.

Weck E and Leistner E, 1986, *Metallographische Anleitung zum Farbätzen nach dem Tauchverfahren*, Part III, DVS, Düsseldorf.

Wen J, Huang Y, Hwang K, Liu C and Li M, 2005, The modified Gurson model accounting for the void size effect, *International Journal of Plasticity*, **21**, 381-395.

Worswick MJ, Chen ZT, Pilkey AK, Lloyd D and Court S, 2001, Damage characterization and damage percolation modeling in aluminum alloy sheet, *Acta Materialia*, **49**, 2791-2803.

Zhang ZL and Niemi E, 1995, A new failure criterion for the Gurson–Tvergaard dilational constitutive model, *International Journal of Fracture*, **70**, 321-334.

Zhang ZL, 1996, A sensitivity analysis of material parameters for the Gurson constitutive model, *Fatigue & Fracture of Engineering Materials & Structures*, **19**, 561-570.

Vita

Ali Ghahremaninezhad Mianji attended Alborz High School in Tehran, Iran. He entered Sharif University of Technology in 1997 where he received the degree of Bachelor of Science in 2001. He was admitted to the Structural Mechanics graduate program at Sharif University of Technology and received the degree of Master of Science in 2003. He worked as a consulting engineer in industry from 2003-2005. He was admitted to the Engineering Mechanics program at The University of Texas at Austin to pursue the Ph.D. degree.

Email: a_ghahremani@utexas.edu

This dissertation was typed by Ali Ghahremaninezhad Mianji.